

ELS-LEED study of low-dimensional plasmons in DySi₂ layers and nanowires

Von der Fakultät für Mathematik und Physik
der Gottfried Wilhelm Leibniz Universität Hannover
zur Erlangung des Grades

Doktor der Naturwissenschaften

Dr. rer. nat.

genehmigte Dissertation

von

Dipl.-Phys. Eddy Patrick Rugeramigabo

geboren am 17. März 1975

in Bujumbura (Burundi)

2007

Referent: Prof. Dr. H. Pfnür
Korreferent: Prof. Dr. M. Rocca

Tag der Promotion: 30.11.2007

Abstract

Low-dimensional dysprosium silicide metal systems grown on Si have been characterized by means of energy loss spectroscopy of low energy electron diffraction. The several silicide phases depending on the growth conditions have been observed. Moreover collective charge excitations were clearly detected and identified as low-dimensional plasmons which have a different dispersion compared to the well known bulk and surface plasmons.

Dy-silicide has been grown on Si(111) by means of molecular beam epitaxy. Due to its small lattice mismatch (-0.3%) to Si(111), Dy-silicide grows in epitaxial high quality crystalline layers. In the submonolayer regime, many silicide phases coexist until the silicide coverage approaches 1ML, and shows the characteristic 1×1 diffraction pattern with the stoichiometry DySi_2 . With further increasing of the coverage, the silicide turns to the multilayer phase. The collective electronic excitations in the monolayer structure have been found to have a 2D-character. Accordingly the plasmon dispersion reaches zero in the long-wavelength limit (at vanishing wave number q) and shows a \sqrt{q} behavior until it entered the domain of strong damping.

When grown on Si(001) the Dy-silicide formed an array of parallel nanowires, in the direction normal to the dimer row direction, and their length was limited by the crossing of another nanowire. A structure dependent energy loss was observed: the energy loss were only sufficiently intense when the 7×2 reconstruction has formed. An possibility of creating vast area with only parallel nanowires in one direction was performed on vicinal Si(001) with four degree miscut. At the same coverage where the 7×2 reconstruction occurs on flat Si(001), it was surprising that, besides the 7×2 periodicity, the diffraction pattern revealed a mixture of phases, with periodicities ranging from the 10×2 to that of the 7×2 , which was observed as the limit of shifting reflex positions. We were able to confirm the highest loss intensity yield at 0.4 ML, the same as on flat Si(001). Plasmon dispersion in the nanowire direction and the lack of plasmon losses in the normal direction to the nanowires confirmed the 1D-structure of the Dy-silicide nanowires. Studying the plasmon dispersion in the silicide nanowires brought us to new plasmon modes. In fact the plasmon dispersion in the nanowires could not fit any 1D-plasmon or 2D-plasmon model, but was in between. A theoretical approach was able to achieve a good approximation of the experimental dispersion curve only by considering the wire enough wide ($\approx 40 \text{ \AA}$) to sustain quasi-two-dimensional plasmons with several modes. For simplification, only the zero-mode was considered and it was able to fit the experimental curve. However it fails to explain the dispersion of the loss FWHM, which could be explained by taking into account the next plasmon mode.

The electron density and effective mass extracted from both low-dimensional systems are found to be in the same order of magnitude, suited for a 2D-electron system. were extremely high for the corresponding dimensions, what implies that other models have to be considered to understand the experimental data.

Kurzzusammenfassung

Niedrig-dimensionale metallische Dysprosium Silizid Systeme wurden auf Si aufgewachsen und mittels energieaufgelöster Beugung langsamer Elektronen charakterisiert. Die unterschiedlichen Silizidphasen in Abhängigkeit der Wachstumsbedingungen wurden untersucht. Außerdem wurden kollektive Ladungsanregungen detektiert und als niedrig-dimensionale Plasmonen identifiziert, die eine andere Dispersion aufweisen, verglichen mit den wohl bekannten Volumen- und Oberflächenplasmonen.

Dysprosiumsilizid wurde mittels Molekularstrahlepitaxie auf Si(001) aufgewachsen. Aufgrund der geringen Gitterfehlpassung (-0.3%) zum Si(111) wächst Dy-Silizid epitaktisch kristallin in hoher Qualität. Im Submonolagenbereich koexistieren viele Silizidphasen bis zu einer Bedeckung von 1ML, die die charakteristische 1×1 Beugungsstruktur aufweist mit einer DySi_2 Stöchiometrie. Mit weiter wachsender Bedeckung wandelt sich das Silizid zu Multilagen Phasen um. Die kollektive elektronische Anregung in der Monolagen Struktur wurde als 2D-Charakter identifiziert. Folglich geht die Plasmonendispersion nach Null im langwelligen Grenzbereich (für Wellenzahl $q \rightarrow 0$) und zeigt ein \sqrt{q} Verhalten bis zum Bereich starken Dämpfung.

Wenn Si(001) als Substrat benutzt wurde, bildet sich aus Dy-Silizid ein Anordnung von parallelen Nanodrähten in der Richtung senkrecht zu den Dimerketten. Die Länge eines Nanodrahtes wird limitiert durch quer dazu wachsende Nanodrähte. Ein strukturabhängiger Energieverlust wurde beobachtet. Eine ausreichende Intensität dieses Energieverlustes wurde nur bei der Bildung der 7×2 Rekonstruktion gesehen. Eine Möglichkeit zur Vergrößerung dieser Bereiche, war die Verwendung von vizinalem, 4° fehlgeneigtem Si(001). Bei der selben Bedeckung, bei der auf flachem Si(001) die 7×2 Rekonstruktion auftritt, wurde hier überraschenderweise das Beugungsmuster einer Mischung von Phasen beobachtet. Dabei wurden Periodizitäten wie bei der saubereren vizinalen Oberfläche bis hin zu denen der 7×2 Überstruktur, die als Grenze der Verschiebung von Reflexpositionen gilt, sichtbar. Es war möglich die höchste Ausbeute der Verlustintensität (selbe wie beim flachen Si(001)) bei einer Bedeckung von 0.4ML zu bestätigen. Die Untersuchung der Plasmonendispersion in den Silizidnanodrähten führte zu neuen Plasmonen Zuständen. Tatsächlich passte die Plasmonendispersion zu keinem der 1D und 2D Plasmonen-Modelle, sondern lag dazwischen. Nur mit Hilfe eines theoretischen Ansatzes war es möglich eine gute Näherung für die experimentellen Kurven zu finden. Das theoretische Modell konnte, durch die Annahme, dass die Drähte breit genug sind ($\approx 40 \text{ \AA}$), Anregungen von quasi-zwei-dimensionalen Plasmonen mit verschiedenen Moden zeigen. Zur Vereinfachung wurde nur die 0.Mode betrachtet, bei der es möglich war die experimentelle Dispersionskurve anzufitten. Dennoch scheiterte dieses Modell bei der Beschreibung der Dispersion der Halbwertsbreite (FWHM), die nur erklärt werden könnte durch Hinzunahme der nächsten Plasmonen Mode.

Die Elektronendichte und effektive Masse, beide extrahiert aus den niedrig dimensionalen Systemen, waren extrem hoch für die entsprechenden Dimensionen. Dies besagt, dass weitere Modelle in Betracht kommen könnten um die experimentellen Daten zu verstehen.

Keywords

low-dimensional Plasmon, thin films, nanowires

Schlagworte

Niedrig-dimensionale Plasmonen, dünne Schichte, Nanodrähte

Contents

1	Introduction	1
2	Surface scattering of low energy electrons	5
2.1	Elastically scattered electrons	6
2.1.1	Kinematic diffraction theory	6
2.1.2	Diffraction from stepped surfaces	8
2.2	Inelastic scattering of electrons	10
2.2.1	Dipole scattering	10
2.2.2	Impact scattering	14
2.3	Plasmons	15
2.3.1	Dielectric function and plasma oscillation frequency	15
2.3.1.1	Surface plasmon and Mie resonance	16
2.3.1.2	Influence of bound <i>d</i> -electrons	17
2.3.2	Plasmon dispersion	18
2.3.2.1	Bulk plasmon	18
2.3.2.2	Surface plasmon	18
2.3.3	Plasmon in lower dimensions	21
3	Experimental setup	23
3.1	Vacuum system	23
3.2	ELS-LEED	24
3.3	Manipulator and sample holder	26
3.4	Dysprosium evaporator	26
4	Sample preparation	29
4.1	The silicon substrate	29
4.1.1	The Si(111) surface	30
4.1.2	The Si(001) surface	31
4.1.2.1	The flat Si(001)-surface	33
4.1.2.2	The vicinal Si(001) with 4° miscut	34
4.1.3	Substrate preparation	34
4.2	Dysprosium silicide	35

5	ELS-LEED on DySi₂ / Si(111)	37
5.1	The clean Si(111)-7×7 substrate	37
5.2	Dysprosium silicide properties	37
5.2.1	Dysprosium silicide growth	37
5.2.2	Silicide surface reconstruction	40
5.2.2.1	Coverage dependence	40
5.2.2.2	Dependence on the substrate temperature	41
5.2.2.3	Annealing temperature dependence	42
5.2.3	Electronic structure of DySi ₂	43
5.2.3.1	Origin of the energy losses	45
5.2.3.2	2D-behavior of the energy losses	45
5.2.3.3	Loss intensity and damping	46
5.2.4	Surface with induced step bunches	46
5.2.5	Discussion	49
6	ELS-LEED on DySi₂ nanowires on Si(001)	53
6.1	Dysprosium silicide on flat Si(001)	53
6.1.1	Structure of clean Si(001) substrate	53
6.1.2	Structure of DySi ₂ on flat Si(001)	55
6.1.2.1	Morphology and reconstructions	55
6.1.2.2	Electronic structure	58
6.1.3	Discussion	62
6.2	Dysprosium silicide on vicinal Si(001)	65
6.2.1	Structure of vicinal Si(001) substrate	65
6.2.2	Investigation of DySi ₂ on vicinal Si(001)	65
6.2.2.1	Study of the morphology of Dy silicide nanowires	66
6.2.2.2	Electronic structure	71
6.3	Discussion	71
7	Summary and outlook	81

Acronyms

AES:	Auger electron microscopy
BZ:	Brillouin Zone
Dy:	Dysprosium
DySi ₂ :	Dysprosium Disilicide
ELS-LEED:	Energy Loss Spectroscopy of Low Energy Electron Diffraction
HREELS:	High Resolution Electron Energy Loss Spectroscopy
FWHM:	Full Width at Half Maximum
I-V:	Current-Voltage
LEED:	Low Energy Electron Diffraction
MBE:	Molecular Beam Epitaxy
ML:	Monolayer
RT:	Room Temperature
Si:	Silicon
STM:	Scanning Tunneling Microscopy
SPA-LEED:	Spot Profile Analysis of LEED
UHV:	Ultra High Vacuum
1D, 2D, 3D:	one-, two-, three-dimensional

Chapter 1

Introduction

Since the construction of the first transistor by Bardeen, Brattain and Shockley, the scientific world has been constantly occupied by the idea of speeding up the charge carriers carrying the signal and diminishing the size of the electronic device. As the feature size of the electron device decreases to the nanometer scale, new electrical, optical and magnetic properties arise, which are significantly different from their bulk counterparts, especially due to quantum confinements and quantum size effects [1]. These new properties may enable new classes of devices like single-electron transistors [2] and molecular switches [3].

In solid state physics, the synthesis of low-dimensional structures has been a topic of scientific and technical interest for decades. For the semiconductor technology the atomic arrangement and the electronic structure of the metal overlayer are of immense interest, both because of their importance for contact in microelectronic devices, and for a fundamental physical understanding. Technologically the principle target is to find materials forming a stable interface with low lattice mismatch. Practically the choice of the metal depends then on its Schottky-barrier height. Metals like Al, Ag, Cu and Au are commonly used as contact materials and their Schottky-barrier on *n*-type Si lies in the range 0.7 - 0.8 eV, whereas silicides from Hf and Ti have 0.5 - 0.6 eV [4].

The pioneering work of Baglin and co-workers [5] has introduced rare-earth (RE) silicides as a major candidates in the Si technology, with low temperature formation, good electrical and thermal conductivity. RE-silicides present a small lattice mismatch with respect to Si(111) from -2.55 to 0.83% (the minus sign means that the RE has a smaller lattice constant), depending on the size of the RE metal [6, 7]. The small lattice mismatch enables the epitaxial growth of chemically sharp interfaces with high degree of crystallinity and structural perfection, well suited for a microscopic understanding of the structural and electronic properties. Moreover silicides of heavy trivalent RE on *n*-type Si have shown a Schottky-barrier height of 0.3 - 0.4 eV, representing the lowest known value for metal/*n*-Si contacts [8]; thus making them a potential candidate for ohmic contacts on *n*-type Si. On *p*-type Si, RE-silicides have a Schottky-barrier height of 0.7 - 0.8 eV, well suited for infrared detectors or photovoltaic applications [9]. In the monolayer RE₂Si₂ phase on *n*-type Si, the Fermi-level position was found

at only 0.08 eV below the conduction band minimum, corresponding to exceptionally low band bending [10, 11]. All those properties make the RE-silicides adequate for potential device applications such as in metallic base transistors [12], or tunable infrared detectors [13], or in conventional microelectronics technology as ohmic or rectifying contacts or low-resistance interconnects to *n*-type Si [14].

For further miniaturization of sub-micron scale electronic devices, the limiting width of the interconnecting wires is set down to the range of the atomic scale. But nanowires narrower than 10 nm are difficult to reach with lithographic methods [15, 16, 17], and nanolithography is too slow if macroscopic areas have to be fabricated. Formation of nanowire structures of width below 10 nm can be achieved using self-assembly methods, which depend on some type of symmetry-breaking phenomenon on a surface to support growth along a preferred direction. These methods, however, produce nanowires which have irregular shapes and sizes, and/or are not robust [18].

In contrast to the epitaxial layer growth of RE-silicide on Si(111), some RE-silicides self-assemble into nanowire structures when grown on Si(001) [19]. The nanowire formation occurs through an anisotropical lattice mismatch : they are closely matched to the Si(001) square surface lattice along one crystallographic axis (lattice mismatch below 1.5% [20]) but possess a significant lattice mismatch along the perpendicular axis. Furthermore, perfectly unidirectional and robust RE-silicides nanowires are formed on vicinal Si(001) with an average length around 2 μm and an average width of 2 nm [21]. In the present work, Dy-silicide has been studied both on Si(111) and on Si(001). By taking advantage of its small lattice mismatch (-0.36%) to Si(111), one can grow epitaxially a perfect crystalline and flat silicide phase with the stoichiometry DySi_2 , which is an atomically thick layer. Besides DySi_2 has been found to form closely packed thin metallic nanowires [22, 23]. The electron confinement reached in 1D and 2D electron systems are attractive and very promising for new peculiar properties that influence transport phenomena and optical properties. Free 1D and 2D electron gas systems are expected to sustain unique collective charge-density excitation [24, 25], which are called 1D and 2D-plasmons.

Electron Loss Spectroscopy of Low Energy Electron Diffraction (ELS-LEED) have been used for the first time to study the atomic and electronic structure of DySi_2 . A normal LEED device can not separate the elastically scattered electrons from the background of electrons that have experienced inelastical scattering. And the acceptance angle of a conventional high resolution electron energy spectrometer is set to acquire a maximum intensity with less angle resolution. With the ELS-LEED device, however, diffraction and spectroscopy informations can be simultaneously gathered from the same point on the substrate, with both high energy and momentum resolution. The plasmon energy can be studied as a function of the momentum number q_{\parallel} parallel to the surface and the dispersion curve can be combined with theoretical approaches, thus leading to information of static and dynamical properties of the electron gas system.

The present work is outlined as follow: In the second chapter we introduce the theoretical concepts of surface diffraction and electronic excitations. In the third and fourth chapters experimental setup and all involved materials in this work will be described.

Especially the UHV-chamber and the ELS-LEED device will be presented. The experimental results will be presented and discussed in the fifth and sixth chapters. In chapter five, the plasmon dispersion of the monolayer DySi₂ is reported together with the geometrical structures encountered. The plasmon dispersion was related to the 2D plasmon model [25] with some plasmon damping effects. The structure of Dy-silicide nanowires on flat and 4°-vicinal Si(001) is presented in chapter six. A plasmon dispersion is reported, which is localized between the 1D and 2D-plasmon dispersion; it is discussed in terms of quasi-2D-plasmon dispersion in a strip region [26]. At the end a summary and an outlook are given.

Chapter 2

Surface scattering of low energy electrons

Electron scattering at surface has been used successfully over decades to study surface morphologies. To take into account the surface sensitivity electrons have to penetrate only into the top most surface layers (3 - 10 Å). This is achieved by normal incident electrons of energy of 10 to 300 eV (LEED) or high energy electrons (in keV units) but at grazing incidence (RHEED).

In the vicinity of the surface impinging electrons interact with the surface components (atoms and electrons). While most of the electrons are elastically backscattered, a non-negligible amount of electrons experience an energy loss or gain in contact with the surface (phonons and impact scattering) or near the surface (dipole scattering).

The analysis of the elastic scattered electrons provides information about the symmetry and the morphology of the surface. A well ordered surface produces sharp reflexes in the diffraction (LEED) pattern. While studying the intensity and shape variation of a single spot with energy one performs SPA-LEED (**S**pot **P**rofile **A**nalysis of **L**ow **E**nergy **E**lectron **D**iffraction). It gives insight over the defects and superstructures available on the surface. Here due to the cross section of low energy electrons a full dynamical LEED-theory needs to be performed. The latter takes into account the multiple scattering effects for a full computation of a diffraction pattern. By such analysis of energy dependent reflex intensities (I(V)-LEED), information about the arrangement of atoms in complex unit cells can be gathered. For simplicity reasons however a kinematic approximation can be used to describe the surface scattering process in the framework of single scattering events. In this way one can still obtain information over the inter atomic distance, step distribution, island size, etc.

Inelastically backscattered electrons are a precious source of spectroscopic information about the elementary excitations at the surface such as lattice vibrations (phonons), oscillations in the electron gas (plasmons) and other electronic excitations (excitons, intraband and interband transitions). Inelastic backscattering can take place at the surface (impact scattering) and via the long-range dipole field of the charge fluctuation (dipole scattering).

In the course of the experiment it is needed, but not always easy to separate elastic from inelastic scattered electrons. While a well ordered surface should give sharp reflexes in the LEED pattern from elastic backscattered electrons, inelastic electrons are also detected as diffuse intensity at finite temperature due to interaction with thermally activated atom vibrations (Debye-Waller factor).

The use of such scatterings for surface studies has been described in many works. A brief review of the fundamentals will be presented in this chapter .

2.1 Elastically scattered electrons

2.1.1 Kinematic diffraction theory

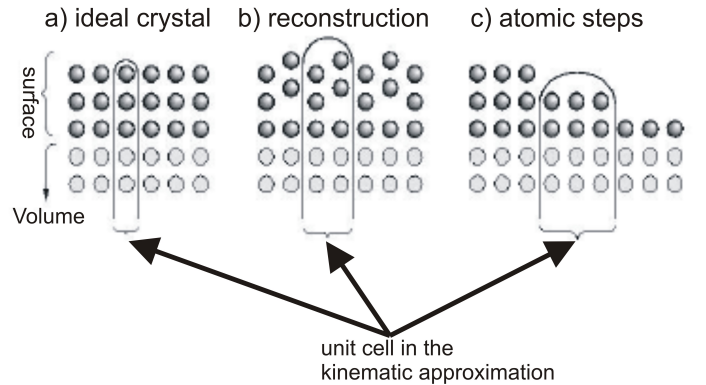


Figure 2.1: Unit cells in the kinematic approximation

In the kinematic approximation single scattering events are considered. In this approximation the surface is divided into identical unit cells, each of which is organised in rows of atoms together with all underlying atoms of the bulk (Fig. 2.1). Incoming electrons as well as backscattered electrons can be considered as plane waves (Fraunhofer diffraction) due to a large distance between the electron gun - sample and detector - sample compared to the electron wavelength. The wave function of an electron incident at atomic position \mathbf{r} can then be expressed as $\Psi_i = e^{i\mathbf{k}_i \cdot \mathbf{r}}$, where \mathbf{k}_i is the wave vector of the incoming electron. If \mathbf{k}_s is the wave vector of the backscattered electron, then the wave function of the scattered electron from the surface is given by

$$\Psi(\mathbf{k}_i, \mathbf{K}) = \frac{1}{N} \sum_{\mathbf{n}} f(\mathbf{n}, \mathbf{K}, \mathbf{k}_i) e^{i\mathbf{K} \cdot \mathbf{R}_{\mathbf{n}}} . \quad (2.1)$$

$\mathbf{K} = \mathbf{k}_s - \mathbf{k}_i$ is the scattering vector. $\mathbf{r}_{\mathbf{n}}$ represents the position vector of the \mathbf{n} -th unit cell. $f(\mathbf{n}, \mathbf{K}, \mathbf{k}_i)$ is a scattering factor, resulting from the sum of the atomic scattering

factors of the row of atoms at the \mathbf{n} -th unit cell :

$$f(\mathbf{n}, \mathbf{K}, \mathbf{k}_i) = \sum_{\mathbf{v}} f_{\mathbf{v}}(\mathbf{K}, \mathbf{k}_i) e^{i\mathbf{K}\mathbf{r}_{\mathbf{v}}} , \quad (2.2)$$

where $\mathbf{r}_{\mathbf{v}} = \mathbf{R}_{\mathbf{v}} - \mathbf{R}_{\mathbf{n}}$ gives the relative position of the atom to the position vector of the unit cell.

During a diffraction experiment the intensity of the diffracted electron beam is detected. It can be obtained mathematically from the scattered wave function as follows:

$$I(\mathbf{K}, \mathbf{k}_i) = |\Psi(\mathbf{K}, \mathbf{k}_i)|^2 = \left| \sum_{\mathbf{n}} f(\mathbf{n}, \mathbf{K}, \mathbf{k}_i) e^{i\mathbf{K}\mathbf{r}(\mathbf{n})} \right|^2 . \quad (2.3)$$

All unit cells contribute to the diffraction intensity. An additional dependence can come from steps, facets and surface inhomogeneities. A simplification can be brought in equation 2.3 if one considers that the scattering factors from all unit cells are the same, allowing to express the intensity as a summation over all unit cells:

$$I(\mathbf{K}, \mathbf{k}_i) = \left| \sum_{\mathbf{n}} f(\mathbf{n}, \mathbf{K}, \mathbf{k}_i) \right|^2 \left| \sum_{\mathbf{n}} \mathbf{n} e^{i\mathbf{K}\mathbf{r}(\mathbf{n})} \right|^2 . \quad (2.4)$$

The intensity expression can be separated into two factors:

$$F(\mathbf{K}, \mathbf{k}_i) = \left| \sum_{\mathbf{n}} f(\mathbf{n}, \mathbf{K}, \mathbf{k}_i) \right|^2 , \text{ and } G(\mathbf{K}) = \left| \sum_{\mathbf{n}} e^{i\mathbf{K}\mathbf{r}(\mathbf{n})} \right|^2 .$$

$F(\mathbf{K}, \mathbf{k}_i)$ is the dynamical form factor. It presents a strong dependence to the electron energy (\mathbf{K}_{\perp}) but the dependence on the parallel component of the scattering vector \mathbf{K}_{\parallel} is very weak. $F(\mathbf{K}, \mathbf{k}_i)$ can be therefore expressed as $F(E)$. The lattice factor $G(\mathbf{K})$ depends on the the surface morphology and the scattering vector \mathbf{K} . Thus the spot profile can be studied using the lattice factor whereas dynamic scattering effects are considered by the form factor.

If for simplicity reasons, and without loss of generality, one considers a well ordered quadratic lattice with lattice constant a , height coordinate normal to the surface plane $h(\mathbf{n})$ and \mathbf{d} the corresponding height unit vector, the atom positions can be described as

$$\mathbf{r}(\mathbf{n}) = a \cdot \mathbf{n} + \mathbf{d} \cdot h(\mathbf{n}) . \quad (2.5)$$

Hence, the scattering vector \mathbf{K} may also be split into its components parallel \mathbf{K}_{\parallel} and perpendicular \mathbf{K}_{\perp} to the surface, so that the lattice factor can be expressed by:

$$G(\mathbf{K}) = \sum_{\mathbf{n}} \left\langle e^{i\mathbf{d}\mathbf{K}_{\perp}[h(\mathbf{n}+\mathbf{m})-h(\mathbf{n})]} \right\rangle_{\mathbf{m}} e^{ia\mathbf{K}_{\parallel}\mathbf{n}} . \quad (2.6)$$

The bracket $\langle \dots \rangle$ means averaging over the index m . If one introduces the pair correlation function $C(\mathbf{n}, h)$ by

$$\left\langle e^{id\mathbf{K}_\perp[h(\mathbf{n}+\mathbf{m})-h(\mathbf{n})]} \right\rangle_{\mathbf{m}} = \sum_h C(\mathbf{n}, h) e^{id\mathbf{K}_\perp h},$$

then one obtains

$$G(\mathbf{K}) = \phi(n, \mathbf{K}_\perp) e^{ia\mathbf{K}_\parallel \mathbf{n}}, \quad (2.7)$$

where

$$\phi(n, \mathbf{K}_\perp) = \sum_h C(\mathbf{n}, h) e^{id\mathbf{K}_\perp h}$$

is the phase correlation function.

For a perfect flat surface $h = 0$. The lattice factor results in a sum of δ -functions

$$G_{ideal}(\mathbf{K}) = \sum_{\mathbf{n}} \delta(\mathbf{K}_\parallel - \frac{2\pi}{a} \cdot \mathbf{n}). \quad (2.8)$$

For an ideally periodic surface, the lack of periodicity in the direction perpendicular to the surface results in well ordered lattice rods in the so-called Ewald-construction. In a LEED pattern the width of the spot are thus only set by the limits of the instrument.

2.1.2 Diffraction from stepped surfaces

Introduction of steps on a surface results in a spot profile dependence on \mathbf{K}_\perp . From equation 2.8 the condition of obtaining maxima is set by $\mathbf{K}_\perp d = 2\pi n$, where n is an integer. A dimensionless scattering phase S can be introduced to replace \mathbf{K}_\perp by

$$S = \frac{\mathbf{K}_\perp d}{2\pi}. \quad (2.9)$$

S is independent from a particular material system and describes the phase difference of electrons scattered from adjacent terraces of step height difference d . For a fixed energy, electrons are described by their de Broglie wavelength $\lambda = (h^2/2m_e eE)^{-1/2}$, with h , m , e , and E the Planck constant, the electron mass, elementary charge and energy, respectively. Equation 2.9 becomes

$$S = 2d \cos \theta (E/150.4)^{1/2}, \quad (2.10)$$

where θ is the angle between the incident electron beam and the normal to the surface. For integer value of S , the so-called in-phase or Bragg condition of scattering, electrons from adjacent terraces interfere constructively and are insensitive to surface roughness. Sharp LEED spots are obtained as in the case of an ideal flat surface. At half integer value of S , the out-of-phase or anti-Bragg condition, electrons interfere destructively and the intensity in the sharp spots is at minimum. The intensity is not vanishing but redistributed into a diffuse shoulder around the spot. The profile of the diffuse intensity

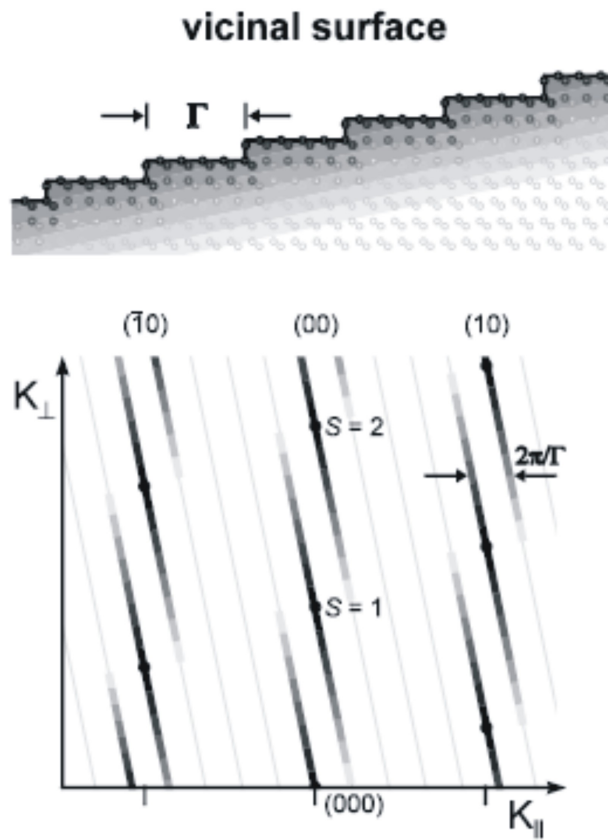


Figure 2.2: Energy dependence of the diffraction rods on a vicinal surface with a regular step train. From ref. [27]

in not depending on S but is given by the terrace width distribution.

For a periodic arrangement of steps as in vicinal surfaces, an additional contribution comes from the separation between individual steps (Fig. 2.2) [27]. This results in lattice rods perpendicular to the vicinal surface. Additionally, splitting of spots occurs. A terrace width Γ of N atoms ($\Gamma = Na$) results in a spot splitting of $2\pi/Na$ in a LEED pattern. The inclination angle of the vicinal surface α can be connected to the size of the spot splitting in unit of the unreconstructed surface Brillouin zone (SBZ) by

$$\Delta K_{SBZ} = \frac{a}{\Gamma} = \frac{a \tan \alpha}{d} . \quad (2.11)$$

The inclination of the vicinal surface can also be determined by the direction of the lattice rods as function of S . They intersect the fundamental rods of a flat surface in in-phase condition in the case of monoatomic steps. Double stepped vicinal surfaces results in lattice rods crossing at out-of-phase condition additionally.

2.2 Inelastic scattering of electrons

When an incident beam of low energy electrons is backscattered from a surface, most of the electrons are elastically reflected. But a small fraction experiences interactions with the surface elementary excitations and an energy loss or gain $\hbar\omega$ occurs, with $\hbar = h/(2\pi)$ where h is the Planck constant, and ω is the vibration frequency of the surface excitation, so that $E_s = E_i - \hbar\omega$. Here E_i and E_s the energy of the incident and inelastically reflected electrons, respectively. The analysis of the energy spectrum of all backscattered electrons leads then to the nature of the involved surface elementary excitations. This is the domain of the electron energy loss spectroscopy (EELS).

The inelastic scattering events are basically treated differently according to the scattering mechanism. An electron can be scattered when still far from the crystal (dipole scattering) or in contact with the surface (impact scattering). In the dipole scattering regime an electron interacts, via its electromagnetic field, with long-range electric field fluctuations present in the vacuum above the crystal surface. In the impact scattering regime, however, the incident electron is scattered near or inside the crystal by surface atomic potential in the top most surface layers. The description of the impact scattering requires to consider the microscopic structure of the substrate potential, but a macroscopical theory may sufficiently describe the dipole scattering. A detailed description of the EELS can be found in the literature [28]. In the following a brief review of the scattering mechanisms will be given.

2.2.1 Dipole scattering

An impinging electron interacts via its electromagnetic field with the dipole field of the elementary excitations of the solid. The nature of the vibrating particles (ions, conduction or valence electrons, adsorbed molecules,...) defines the kind of excitation

that are observed (phonons, plasmons, excitons, vibrations of adsorbates, ...). Fig. 2.3 illustrates the dipole scattering. The electric field of an incident electron with wave vector \mathbf{k}_i interacts with the dipole moment of an adsorbed molecule and the inelastically backscattered electron has a final wave vector \mathbf{k}_s . If projected onto a plane parallel to the surface, the wave vector transfer experienced by the electron can be defined as $\mathbf{Q}_{\parallel} = \mathbf{k}_i - \mathbf{k}_s$. The surface of the crystal can be considered as lying in

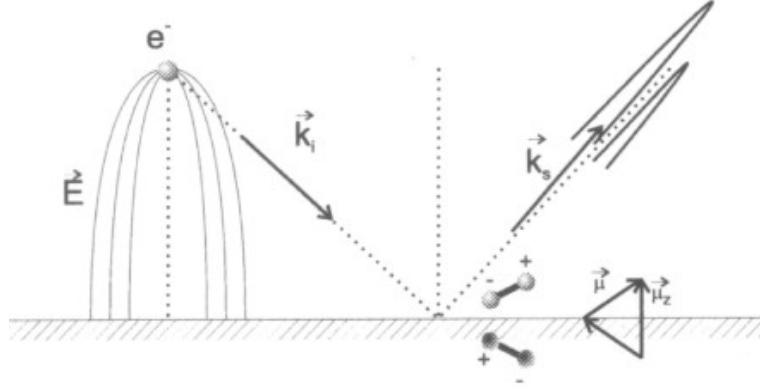


Figure 2.3: Dipole scattering through interaction of the electric field of an electron with the dipole moment of an adsorbed molecule. The electron experiences a small angle scattering in the specular direction.

the plane (xy), with the crystal in the half space $z < 0$ and the vacuum above. If the wave vector transfer \mathbf{Q}_{\parallel} is caused by an excitation with frequency ω_0 , then retardation effects can be ignored if $\omega_0/\mathbf{Q}_{\parallel} \ll c$, with c the velocity of the light. For a given value of \mathbf{Q}_{\parallel} and for an energy change of $\hbar\omega = E_i - E_s$, the direction of the reflected electron is uniquely determined. If $\rho(\mathbf{x}, t)$ is defined as the change in the charge density due to elementary excitations of any nature in the system, with $\int d\mathbf{x}\rho(\mathbf{x}, t) = 0$ for charge neutrality reason, the electrostatic potential that is seen by an approaching electron above the surface is given by:

$$\varphi(\mathbf{x}, t) = \int d\mathbf{x}' \frac{\rho(\mathbf{x}', t)}{|\mathbf{x} - \mathbf{x}'|} = 2\pi \int \frac{d^2Q_{\parallel}}{Q_{\parallel}} e^{-Q_{\parallel}x_{\perp}} e^{i\mathbf{Q}_{\parallel} \cdot \mathbf{x}_{\parallel}} \int_{x'_{\perp} \leq 0} d\mathbf{x}' \rho(Q_{\parallel}, x'_{\perp}, t) e^{Q_{\parallel}x'_{\perp}}, \quad (2.12)$$

where

$$\rho(Q_{\parallel}, x'_{\perp}, t) = \int d^2x'_{\parallel} e^{-i\mathbf{Q}_{\parallel} \cdot \mathbf{x}'_{\parallel}} \rho(\mathbf{x}', t).$$

Because the potential must obey the Laplace's equation in the vacuum above the crystal, the electron feels the excitation at a distance $\approx \mathbf{Q}_{\parallel}^{-1}$ far from the crystal and senses the instantaneous position of the charges in the medium in very short time scale compared to the period of excitation. This indicates that only long-wavelength vibrations will strongly interact with the probing electron because their potential extends quite far

in the vacuum and will provide a long time coupling. Through energy and momentum conservation $E_s - E_i = \pm \hbar\omega$ and $\mathbf{k}_s - \mathbf{k}_i = \mathbf{Q} + \mathbf{G}$, the dipole scattering will emphasize those inelastic events associated with the excitation of small wave vectors, which cannot scatter the electron very far from the specular (or Bragg) reflection direction [29]. An important consequence is that the maximal efficiency takes place at an angle of $\hbar\omega_0/2E_i$ which, in the normal experiment condition $\hbar\omega \ll E_i$, peaks the maximum near the specular direction, the so-called dipolar lobe in the angular distribution.

It can also be seen that the potential is produced by charge fluctuations that extend down to a distance $\approx \mathbf{Q}_{\parallel}^{-1}$ below the crystal surface. Thus an electron that experiences an inelastic scattering with a change of its wave vector parallel to the surface of a value $\mathbf{Q}_{\parallel}^{-1}$ senses deep into the medium roughly the distance $\mathbf{Q}_{\parallel}^{-1}/\epsilon_0$.

The amplitude of the inelastically backscattered electrons can be calculated by inserting the potential $\varphi(\mathbf{x}, t)$ into the Schrödinger equation and solving it in the first order in $\varphi(\mathbf{x}, t)$ using the perturbation theory. For an accurate description of the scattering amplitude only two small-angle inelastic scattering events make the dominant contribution to the scattering cross section. They are related to dipole scattering accompanied with specular reflection as illustrated in Fig. 2.4. The scattering efficiency per solid

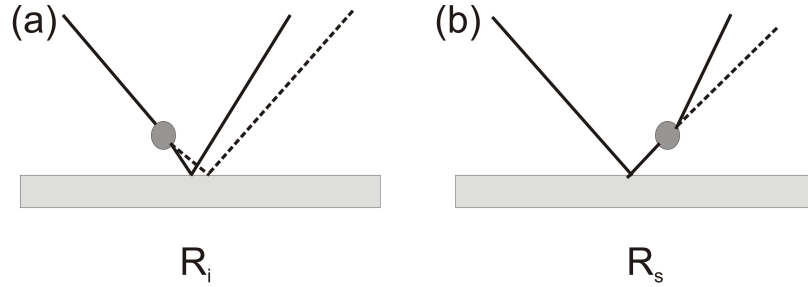


Figure 2.4: Dipole scattering event with small-angle scattering. The full circle represent the scattering center of an electron from the fluctuating electric field in the vacuum above the crystal. Specular reflections on the surface are considered.

angle and unit energy $d^2S/d\Omega(\hat{k}_s)d\hbar\omega$ is more convenient to calculate. The combination $(d^2S/d\Omega(\hat{k}_s)d\hbar\omega)d\Omega(\hat{k}_s)d\hbar\omega$ is dimensionless and gives the probability that an electron will scatter from its initial state into a final state in the solid angle $d\Omega(\hat{k}_s)$, and in the energy range $d\hbar\omega$. The scattering efficiency per solid angle and unit energy is given by

$$\frac{d^2S}{d\Omega d\hbar\omega} = \frac{m^2 e^2 v_{\perp}^2}{2\pi^2 \hbar^5 \cos \theta_i} \left(\frac{k_s}{k_i} \right) \frac{|v_{\perp} Q_{\parallel} (R_s + R_i) + i(R_i - R_s)(\omega - \mathbf{v}_{\parallel} \cdot \mathbf{Q}_{\parallel})|^2}{Q_{\parallel}^2 [v_{\perp}^2 Q_{\parallel}^2 + (\omega - \mathbf{v}_{\parallel} \cdot \mathbf{Q}_{\parallel})^2]^2} \cdot P(\mathbf{Q}_{\parallel}, \omega). \quad (2.13)$$

In this expression, θ_i is the angle of incidence with respect to the surface normal, v_{\perp}^2 and v_{\parallel}^2 are the magnitude of the incident electron velocity normal and parallel to the

surface, respectively, k_i and k_s are the magnitudes of the wave vectors of the incident and scattered electron, respectively. R_i and R_s are the probability amplitudes that describe the specularly reflected electron before or after the inelastic scattering due to dipole scattering. $P(\mathbf{Q}_{\parallel}, \omega)$ contains information on the physics of the surface region of the crystal. If in the small angle inelastic electron scattering from surfaces the energy transfer $\hbar\omega$ is small with respect to the electron incident energy E_i , then one may correctly assume $R_i \approx R_s$, so that the expression in equation 2.13 can be transformed to

$$\frac{d^2S}{d\Omega d\hbar\omega} = \frac{2m^2 e^2 v_{\perp}^4}{\pi^2 \hbar^5 \cos \theta_i} \left(\frac{k_s}{k_i} \right) \frac{|R_i|^2}{\left[v_{\perp}^2 Q_{\parallel}^2 + (\omega - \mathbf{v}_{\parallel} \cdot \mathbf{Q}_{\parallel})^2 \right]^2} \cdot P(\mathbf{Q}_{\parallel}, \omega), \quad (2.14)$$

where $|R_i|^2$ is the intensity of the elastically reflected beam normalized to the incident intensity. However the validity of the assumption $R_i \approx R_s$ must be carefully checked out due to the fact that in the low incident energy, even if the energy transfer $\hbar\omega$ is small with respect to the E_i , strong resonances can appear in R_i or R_s , so that the assumption $R_i \approx R_s$ is not anymore valid. It becomes then important to know if the dipole scattering event occurred before or after the specular reflection at the surface.

In equation 2.14, the right-hand side expression can be separated into the expression of $P(\mathbf{Q}_{\parallel}, \omega)$ and the rest of the expression which is defined as the kinematic factor. It describes the angular distribution of the inelastically scattered electrons, resulting in the typical form of the dipolar lobe. In this expression all parameters can be fully determined either by the scattering geometry or are directly measurable. This is not the case for $P(\mathbf{Q}_{\parallel}, \omega)$ which describes the shape of the energy loss spectrum and contains the response of the target, given by its dielectric properties. $P(\mathbf{Q}_{\parallel}, \omega)$ is related to the dielectric properties of the substrate by the expression [28, 30]

$$P(\mathbf{Q}_{\parallel}, \omega) = \frac{2\hbar Q_{\parallel}}{\pi} [1 + n(\omega)] \text{Im} \left((\tilde{\epsilon}(Q_{\parallel}, \omega) + 1)^{-1} \right), \quad (2.15)$$

where

$$n(\omega) = \left[e^{\frac{\hbar\omega}{k_B T}} - 1 \right]^{-1}.$$

$\tilde{\epsilon}(Q_{\parallel}, \omega)$ describes the effective dielectric function of the surface. The expression $\text{Im} \left((\tilde{\epsilon}(Q_{\parallel}, \omega) + 1)^{-1} \right)$ in equation 2.15 is in general described as the loss function.

The expression of $\tilde{\epsilon}(Q_{\parallel}, \omega)$ is obtained within a simple model description of the substrate. One considers a semi-infinite substrate with a complex, but isotropic dielectric constant $\epsilon_b(\omega)$ upon which a layer of thickness d and dielectric function $\epsilon_s(\omega)$ is added. For a certain value of d and $\epsilon_s(\omega)$ one may describe a layer of adsorbed molecules, or model a semiconductor with a depletion or an accumulation layer near the surface. If $d \rightarrow 0$ an appropriate choice of $\epsilon_b(\omega)$ may enable to discuss scattering from a metal, or a semiconductor with free carriers present, or an insulator where interband electronic transitions contribute mostly to $\epsilon_b(\omega)$. The expression of $\tilde{\epsilon}(Q_{\parallel}, \omega)$

is then given by [28, 30]

$$\tilde{\epsilon}(Q_{||}, \omega) = \epsilon_s(\omega) \left[\frac{1 + \Delta(\omega)e^{-2Q_{||}d}}{1 - \Delta(\omega)e^{-2Q_{||}d}} \right], \quad (2.16)$$

where

$$\Delta(\omega) = \frac{\epsilon_b(\omega) - \epsilon_s(\omega)}{\epsilon_b(\omega) + \epsilon_s(\omega)}.$$

It may be added that increasing the energy of the impinging electrons decreases the excitation cross section. This cross section is proportional to the intensity of the specular beam, and thus enables normalization and comparison of experimental data.

All vibrating modes are not detected in an EELS experiment. A molecule adsorbed on a metal surface has in general vibrational frequency which is nearly two order of magnitude smaller than that of the free electron gas in the metal. Any change in the dipole moment of the molecule can be followed instantaneously by the metal electrons, forming in that way an image dipole in the metal. The image dipole reinforce perpendicular vibrations while parallel vibrations are screened. This is the metal surface selection rule which states that only molecules with vibrational, totally symmetric modes, that produce an non-zero electric dipole change perpendicular to the metal surface will be detected close to the specular reflected beam. Note that this implies that the dipole and its image in the metal are very close with respect to the electron-surface distance in the long-range interaction, so that the incident electron can not distinguish between them. If the dipole is removed away from the surface oscillations in EELS, cross sections for both perpendicular and parallel vibrations can be induced [31].

2.2.2 Impact scattering

The impact scattering event occurs when the incident electron is scattered in the near vicinity of the surface by atomic potentials of the substrate or adsorbate atoms. Elastic scattering at the surface results in electron diffraction and is described in the LEED theory. Inelastic scattering occurs when the atoms are displaced by excited vibrations (phonons). The characteristics of atomic potentials implies that the impact scattering is essentially a short range interaction, accompanied by large momentum transfers.

Contrary to the dipole scattering, the impact scattering results in a broad angular distribution, and the closeness of the interaction to the surface requires a microscopic approach of the surface in order to describe the impact scattering. A most complete theoretical treatment of the impact scattering can be found in [32, 33]. It describes the adsorbate and substrate target by an array of muffin-tin potentials. The potentials associated with sites of interest are displaced rigidly by the vibration. This model description does neither take into account the dipole moment nor the electron response due to the fact that the incident electron near the surface does not sense anymore the image dipole. Within that model the probability that an electron scatters into the solid

angle $d\omega$ is given by the expression

$$\frac{dP}{d\Omega} = \frac{mE_0}{s\pi^2\hbar^2} \frac{\cos^2\theta_i}{\cos\theta_s} S |M(\mathbf{k}_i, \mathbf{k}_s, q_{||}, \mathbf{u})|^2, \quad (2.17)$$

where θ_i and θ_s are the angle of incidence and of analysis, S is the sample area, m is the electron mass. M is a matrix element that describes the scattering of an electron of initial \mathbf{k}_i and final \mathbf{k}_s wave vector from a surface phonon of wave vector $q_{||}$ and polarization \mathbf{u} .

From model calculations it comes out that the inelastic cross section is no longer proportional to the intensity of the incident beam, so that normalization and intensity comparison fails. Moreover the intensity of the inelastic scattering increases on an average with increasing incident energy. Also the impact scattering selection rule differs from the dipole one. It states that, if the plane contains \mathbf{k}_i and \mathbf{k}_s and the normal to the surface, surface phonons having polarization \mathbf{u} parallel to the surface but perpendicular to the plane of incidence will not be observed.

2.3 Plasmons

A plasmon is defined as the quantum of a plasma oscillation, which is a collective longitudinal excitation of the free electron gas in a metal or in a semiconductor with a high dopant concentration. Collective oscillations of free charges determine the dielectric behavior in those materials.

2.3.1 Dielectric function and plasma oscillation frequency

The expression of the dielectric function $\varepsilon(\omega) = D(\omega)/E(\omega)$, with $D(\omega)$ the electric displacement and $E(\omega)$ electric field, can be derived from the motion of an electron in an electric field using Newton second law as

$$\varepsilon(\omega) = 1 - \frac{\omega_p^2}{\omega^2}, \quad (2.18)$$

where

$$\omega_p = \sqrt{\frac{4\pi ne^2}{m}} \quad (2.19)$$

is the bulk plasma frequency obtained by fulfilling the condition $\varepsilon(\omega) = 0$ for propagation of longitudinal waves. n is the electron density, m the electron mass and e the electron charge.

The expression of the dielectric function in equation 2.18 does not take into account the influence of the ion core background like in a simple metal. A model description for the electronic properties of a simple metal can be sufficiently achieved by using the so-called jellium-model. In this model the valence electrons are considered to be free

and the positive ions core form an homogeneous positive background. A perturbation in the electron gas with respect to the positive ion background can be expressed by an equation of motion inside the Drude model in which the damping constant γ is given by the electric conductivity. The expression of the dielectric function is then given by

$$\varepsilon(\omega) = \varepsilon_\infty - \frac{\omega_p^2}{\omega^2 + i\gamma\omega} . \quad (2.20)$$

One can see that in the limit of weak damping ($\gamma \rightarrow 0$) equation 2.20 reduces to equation 2.18. In the expression of ω_p , m represents in this case the effective mass of the electrons in the conduction band of the solid.

2.3.1.1 Surface plasmon and Mie resonance

If a semi-infinite metal is considered with the surface lying in the plane (x,y) and the metal bulk in the half-space $z < 0$, an external electromagnetic field can interact with the metallic surface and thus create a wave-like perturbation of the charge density localized at the surface, which is called surface plasmon [34, 35]. Surface plasmons are self-sustaining oscillations of the electron gas characterized by an exponential decay of the potential ϕ associated to it, both towards the vacuum and the bulk. Similar to the bulk plasmon, surface plasmons are longitudinal modes. From classical electromagnetics the electric potential ϕ is given by

$$\phi(\mathbf{r}) = \phi_0 e^{i\mathbf{Q}_\parallel \cdot \mathbf{r}_\parallel} e^{-Q_\parallel |z|} , \quad (2.21)$$

where \mathbf{r}_\parallel is the position vector in the surface plane, \mathbf{Q}_\parallel is the momentum of the surface plasmon and z is the distance normal to the surface, with $z = 0$ in the surface plane and the vacuum above in the half-space $z > 0$. The normal component of the electric field E_z associated with equation 2.21 can be obtained by differentiating equation 2.21 with respect to the z direction:

$$\begin{aligned} E_z(z = 0^+) &= \phi_0 Q_\parallel e^{i\mathbf{Q}_\parallel \cdot \mathbf{r}_\parallel} \\ E_z(z = 0^-) &= -\phi_0 Q_\parallel e^{i\mathbf{Q}_\parallel \cdot \mathbf{r}_\parallel} . \end{aligned} \quad (2.22)$$

E_z is discontinuous across the surface. However the z component of the electric displacement vector $D_z = \varepsilon E_z$ must be continuous accros the metal-vacuum interface, so that $\nabla \cdot D = 0$ is fulfilled. This results in the condition of existence of surface plasmon

$$\varepsilon(\omega) = -1 . \quad (2.23)$$

Inserting equation 2.23 in equation 2.18 results in the expression of the surface plasmon which is determined by the bulk electronic properties.

$$\omega_s = \omega_p / \sqrt{2} . \quad (2.24)$$

In the ideal case of spherical metal clusters the resonance condition becomes $\varepsilon(\omega) = -2$, so that the surface excitation occurs at the Mie frequency ω_M given by [36]

$$\omega_M = \omega_p / \sqrt{3} . \quad (2.25)$$

2.3.1.2 Influence of bound d -electrons

The expression of ω_p in equation 2.19 is no longer valid in the case of metals with strongly bound d -electrons where, as in silver for example, the assumption of a free electron gas fails due to the mutual polarization between the $5s$ and $4d$ states. Such $s-d$ polarization is responsible for a large renormalization of the Ag bulk plasma frequency that can be understood by considering the dielectric function. The real part of $\epsilon(\omega) = \epsilon_1(\omega) + i\epsilon_2(\omega)$ must be rearranged to contain the contribution from the free electrons in the $s-p$ band and an additional contribution from the bound d -electrons [37]:

$$\epsilon_1(\omega) = \epsilon_1^s(\omega) + \epsilon_1^d(\omega) - 1, \quad (2.26)$$

where $\epsilon_1^s(\omega)$ is the Drude term, appropriate for the $5s$ electrons and $\epsilon_1^d(\omega)$ is the bound electron contribution whose frequency dependence is governed by interband transitions from the occupied $4d$ band to the $5s$ conduction band, close to the Fermi level (Fig. 2.5). The contribution of the bound term is to decrease the bulk plasma fre-

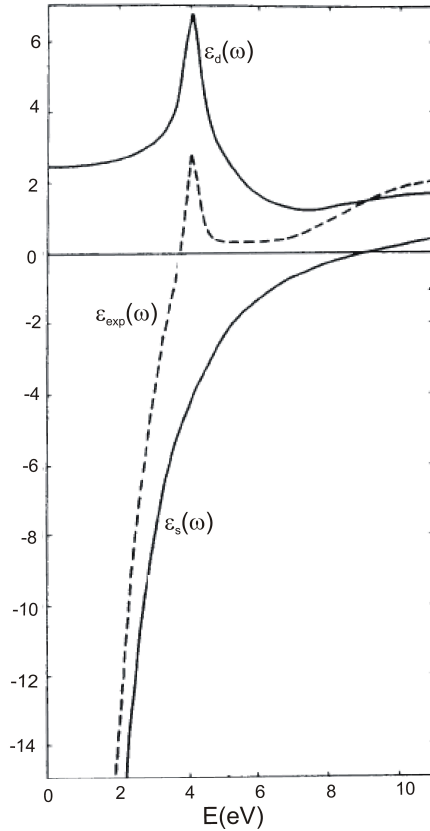


Figure 2.5: Ag-dielectric function $\epsilon(\omega)$ versus energy, as measured optically, from ref. [40]

quency from the unscreened, calculated value (from equation 2.19 for $n=5$) of $\omega_p=9.2$

eV to the observed value [38] of 3.8 eV. Accordingly, the surface plasmon and the Mie resonance are down shifted from the calculated values of 6.5 eV and 5.3 eV to the measured values 3.7 eV and 3.5 eV, respectively.

In the following the plasmon treatment will be restrained to the case of simple metals if not explicitly indicated.

2.3.2 Plasmon dispersion

2.3.2.1 Bulk plasmon

The dispersion relation of the dielectric function describing the variation of the bulk dielectric constant with the wave vector q can be determined using the theory of the linear response based on the *Random Phase Approximation* (RPA). It is the so-called Lindhardt dielectric function [39]

$$\varepsilon(q, \omega) = 1 - \frac{4\pi e^2}{q^2 V} \sum_k \frac{f_F(k+q) - f_F(k)}{E(k+q) - E(k) - \hbar + i\hbar/\tau}, \quad (2.27)$$

where V is the volume of the free electron gas, f_F the Fermi function, $E(k)$ the energy values of the electrons and τ a damping constant. The bulk plasmon dispersion can be derived from equation 2.27, its expression is given by

$$E_p(q) = \hbar\omega_p(q) = \hbar\omega_p + \frac{3\hbar E_F}{5m\omega_p} q^2, \quad (2.28)$$

with E_F the Fermi energy. Note that in the limit $q \rightarrow 0$, equation 2.28 reduces to the bulk plasma frequency derived in equation 2.19. The excitation of plasmons is accompanied by single particle excitation (SPE) where an excited electron has enough energy to make a transition to an unoccupied state, leaving behind a hole. There is a critical value q_c in the momentum transfer where the dispersing plasmon energy begins to decay by creating electron-hole pairs (Fig. 2.6).

2.3.2.2 Surface plasmon

The dispersion of the surface plasmon can be found considering the dynamical response of the electrons at a metal surface to a time varying external field. Here for simplification the jellium model for simple metals is again considered, with the ions core forming a uniform positive background truncated at the surface and the valence electrons are considered free. The electron distribution near the surface region needs to be closely considered due to the fact that the surface plasmon dispersion is very sensitive to the charge distribution at the surface [38].

If a weak uniform external field oscillating at frequency ω is applied to a jellium surface, an induced charge $\delta(z, q, \omega)$ localized in the surface region is created as a response of the system to the perturbation. The probability of exciting plasmons or

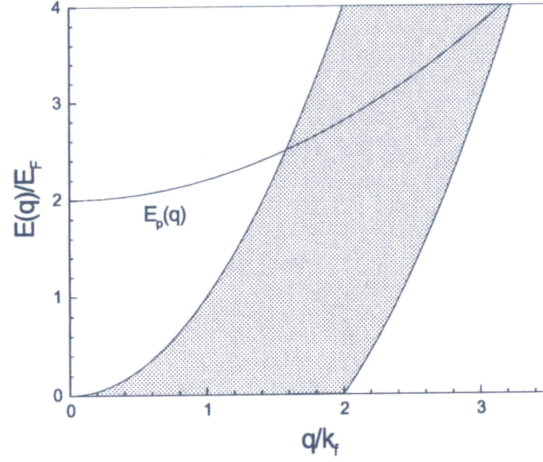


Figure 2.6: Bulk plasmon dispersion. The grey-area is the domain with high probability of electron-hole pairs excitation

electron-hole pairs can be determined from the imaginary part of the surface response function $g(q_{||}, \omega)$ [41]

$$g(q_{||}, \omega) = \int dz e^{qz} \delta(z, q, \omega) . \quad (2.29)$$

The response function $Im(g(q, \omega))$ has been calculated within the *time dependent local density approximation* (TDLDA) as well as its frequency dependence [37]. It has been found that, besides the expected surface plasmon, an additional surface mode at $\omega_m = 0.8\omega_p$ appears, which corresponds to the so-called multipole surface mode. Compared to the monopole charge distribution associated to the ordinary surface plasmon, the multipole surface mode has charge fluctuation normal to the surface with an extra node.

The surface response function may now be associated to the dielectric function. Across the surface the local dielectric function of the solid was found discontinuous. To insure the continuity of the electric displacement vector \mathbf{D} across the vacuum-solid interface, the expression of the response function becomes:

$$g(q_{||}, \omega) = \frac{\epsilon(\omega) - 1}{\epsilon(\omega) + 1} , \quad (2.30)$$

with $\epsilon(\omega) = 1 - \omega_p^2/\omega^2$ the Drude dielectric function. With the condition $\epsilon(\omega) = -1$ for the excitation of surface plasmon, the surface plasmon frequency is defined by the pole of the response function. A more complete expression of the response function has been developed for small $q_{||}$, taking into account the position of the surface screening charge relative to the edge of the jellium [42, 43].

$$g(q_{||}, \omega) \approx \frac{\epsilon(\omega) - 1 + q_{||}d(\omega) [\epsilon(\omega) - 1]}{\epsilon(\omega) + 1 - q_{||}d(\omega) [\epsilon(\omega) - 1]} . \quad (2.31)$$

The quantity $d(\omega)$ is the centroid of the surface screening charge induced by an elec-

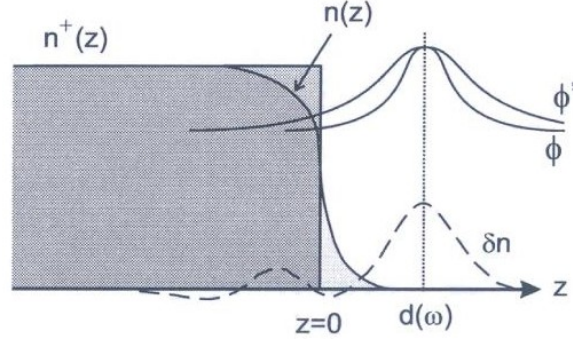


Figure 2.7: Schematic illustration of the influence caused by the position of induced charge density distribution δn on the plasmon dispersion. $n(z)^+$ and $n(z)$ represent the positive charge background and the negative charge distribution in the jellium, respectively. The potential associated with δn is illustrated by ϕ and ϕ' for large and small values of q , respectively.

trical field normal to the surface, measured from the edge of the positive charge background (Fig. 2.32):

$$d(\omega) = \frac{\int dz z \delta(z, 0, \omega)}{\int dz \delta(z, 0, \omega)}. \quad (2.32)$$

For $\omega \neq 0$, $d(\omega)$ is a complex number, where its real part $Re(d(\omega))$ gives the dispersion of the surface plasmon and the imaginary part $Im(d(\omega))$ the width. Considering the pole of the surface response function $g(q_{||}, \omega)$, the dispersion of the surface plasmon at small $q_{||}$ is given by

$$\omega_s(q_{||}) = \omega_s \left[1 - \frac{1}{2} q_{||} Re(d(\omega)) + O(q_{||}^2) \right]. \quad (2.33)$$

Due to the fact that $Re(d(\omega))$ is positive for all simple metals [42, 44] the surface scattering process induces a negative dispersion at small $q_{||}$. A simple physical picture can help to understand that behavior. As illustrated in Fig. 2.32, the centroid of the induced charge distribution is located outside the jellium edge. The potential associated to this charge decays exponentially towards the surface, and up to a distance which is inversely proportional to $q_{||}$. This means that the perturbation is more localized with increasing $q_{||}$ and therefore extends to region with lower electron density. The lowering of the electron density results (equation 2.19) in the decrease of the plasma frequency, thus leading to the negative plasmon dispersion.

2.3.3 Plasmon in lower dimensions

The concept of surface plasmon can be extended, if the oscillating charge density distribution is confined to a two-dimensional(2D) space. Theoretically a model system can be achieved, if one assumes free conduction electrons embedded in a jellium layer of ion cores forming a uniform positive background. The 2D jellium is lying on a semi-infinite dielectric medium. Experimentally, the 2D jellium can be made of metals which surfaces (for instance (111)-Ag, (111)-Au surfaces) are known to support a partially occupied band of Shockley surface states within a wide projected energy gap around the Fermi level [45, 46]. These states are strongly localized near the surface and disperse with momentum parallel to the surface. Hence they can be considered to form a quasi 2D surface-state band with a 2D Fermi energy. In the absence of the 3D substrate those surface states would support a new art of surface plasmon, the so-called 2D-plasmon. The absence of the 3D metallic substrate can be achieved by a (semi)-insulating material supporting the 2D electron system. In the presence of the 3D substrate, dynamical screening at the surface can provide a mechanism for the existence of the so-called acoustic surface plasmon, as recently observed on the (0001) Be surface with a linear energy dispersion [47].

It has been seen that the surface plasmon frequency is determined by the bulk proper-

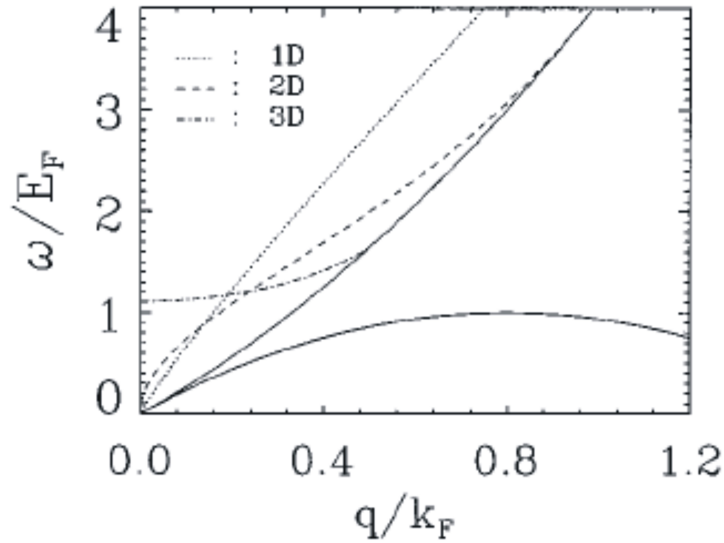


Figure 2.8: Comparison of plasma dispersion in three dimensions. The solids lines indicate the single-particle electron-hole continuum excitation regime in 1D. From ref. [48]

ties (equations 2.24 and 2.33). In contrary the properties of the 2D-plasmon are determined by the properties of the 2D electron system itself, especially due to the restriction in the motion normal to the surface. Within the framework of the self-consistent-

field approximation the response of a 2D electron gas to a longitudinal electric field of arbitrary wave vector and frequency has been calculated, leading to the expression of the 2D-plasmon dispersion of a 2D nearly free-electron system at small q_{\parallel} [25]:

$$\omega_{2D}^2(q_{\parallel}) = \frac{2\pi n e^2}{m^* \epsilon_b} q, \quad (2.34)$$

where n is the 2D electron density of occupied surface states, m^* the effective electron mass, and ϵ_b is the dispersionless dielectric constant of the substrate supporting the 2D electron gas. It can be seen from equation 2.34 that $\omega_{2D}^2 \rightarrow 0$ for $q \rightarrow 0$. In contrary surface and bulk plasmons have finite energy in the limit $q \rightarrow 0$.

If the 2D-electron system is restricted in one direction whereas the other direction is chosen to extend infinitely, the resulting 1D-electron system would sustain collective motion exhibiting sound-wave behavior [24] or 1D-plasmons. The 1D-plasmon dispersion has been found to be proportional to $q\sqrt{|ln(q)|}$, which results also in vanishing plasmon energy in the long-wavelength limit [48] (Fig. 2.8).

The lifetime of the plasmon is limited by its decay into single particles excitations. A general distinction is made between the direct Landau damping and the indirect Drude damping. The Landau damping mechanism involves a single sp -band or direct $d \rightarrow sp$ transitions whereas in the Drude mechanism, inter- and intraband transitions are mediated by the exchange of reciprocal lattice vectors or of phonons [49].

Chapter 3

Experimental setup

3.1 Vacuum system

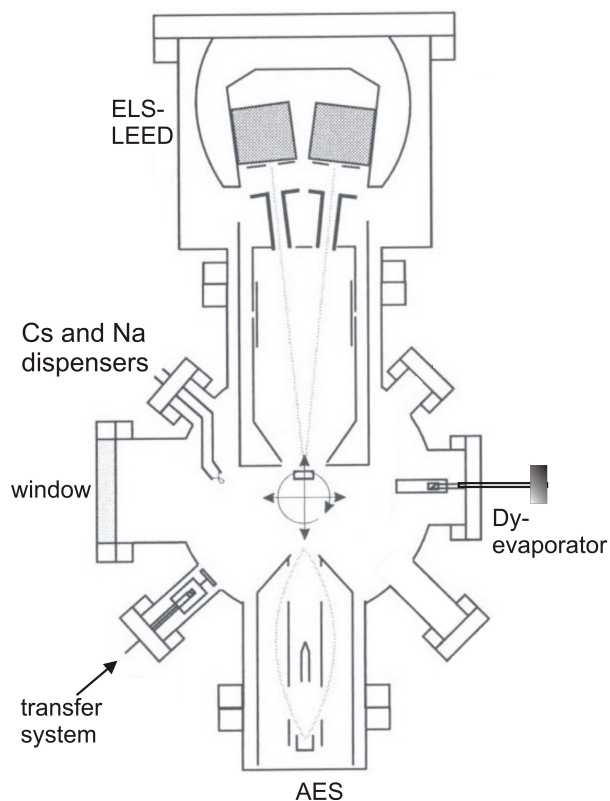


Figure 3.1: A schematic view of the UHV-chamber

The present work was performed in an Ultra High Vacuum (UHV) chamber. Surface science is dependent on such apparatus when dealing with atomically clean surfaces or controlled layer absorption on prepared surfaces. It is therefore necessary to reduce

to the minimum the rate of contamination of samples surfaces over the time required to conduct measurements.

The vacuum system used in our experiments was made of a main chamber on which a transfer system was coupled. For the main chamber a standard pumping system made of a 125 l/s ion-getter pump (triode system), a titan-sublimation pump, a turbo-molecular pump (type varian V70LP) was able to reach a basic pressure $\leq 2 \times 10^{-10}$ mbar after backing out the whole chamber for 24 hours at 200°C. In the range of pressure $\leq 1 \times 10^{-10}$ mbar the main chamber was then only pumped by the ion-getter pump and the titan-sublimation pump, separated from the rest of the pumping system by a valve. The basic pressure in the main chamber was $\leq 5 \times 10^{-11}$ mbar.

The transfer system was pumped independently. A turbo-molecular pump (type Balzers TPU 062) was able to reach in few hours 1×10^{-8} mbar. This was made possible by a pre-pressure system made of a vacuum-can that was continuously pumped by a rotary pump. A quicker pumping could also be achieved by shortly backing out. The transfer system enabled a rapid change of samples without breaking the vacuum over several months.

Fig. 3.1 represents a middle cut view of the used vacuum chamber. The pressure and the nature of the rest gas in the chamber was measured using an ionisation gauge (type ionivac IM510) and a quadrupole mass spectrometer, respectively. Surface analysis and characterisation was obtained through ELS-LEED and AES measurements. The housing of ELS-LEED was additionally covered from inside by μ -metal-plates, to achieve a sufficient protection against external magnetic fields. A non commercial Dy-evaporator was used as source of adsorbant.

3.2 ELS-LEED

The energy loss spectroscopy of low energy electron diffraction (ELS-LEED) was the main experimental method in this work. The ELS-LEED, shown in Fig. 3.2, is a unique method that enables a combined study of elastically and inelastically scattered electrons from crystal surfaces. It is made from a combination of a conventional high resolution electron energy loss spectrometer (HREELS) [50] with a deflection unit for a high momentum resolution in the profile analysis of LEED-spots (SPA-LEED) [51]. This combination yields a powerful technique to study surface morphologies through diffraction of elastically scattered electrons and surface electronic structures using inelastically scattered electrons, simultaneously with high energy and momentum resolution [52, 53].

A schematic view of the ELS-LEED device is given in Fig. 3.2. The electron beam, emitted from an electron gun with a tungsten cathode, is focalised by means of lenses into the entry slit of the monochromator made of a 127°-cylindrical condenser. The monochromator pass-energy is obtained by setting adequate voltages on the condensers. Only electrons with the selected pass-energy reach the end-slit, where they are then accelerated to the LEED-energy. Before reaching the sample, the monochroma-

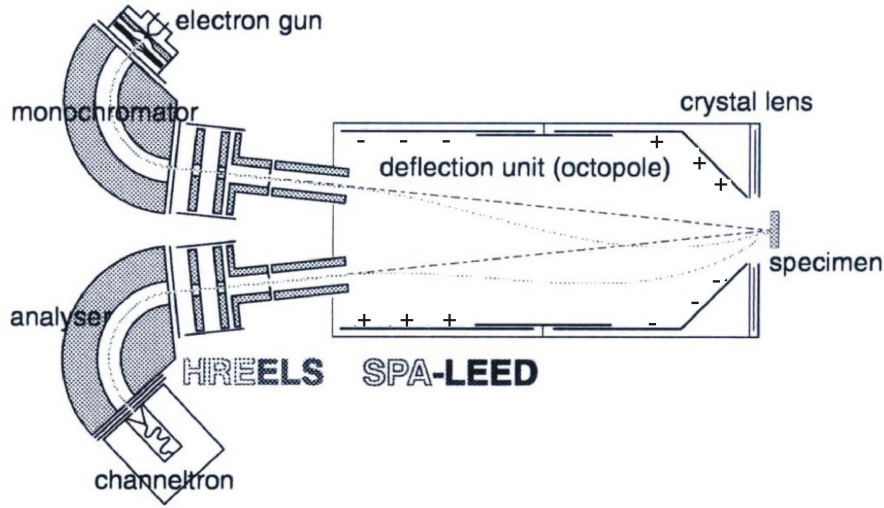


Figure 3.2: A schematic view of the ELS-LEED spectrometer

tized electrons pass through the deflection unit where a precise momentum transfer can be selected. The electrons are then scattered off the sample surface and are decelerated to reach the pass-energy of the analyser (similar to the monochromator). The electron reaching the end-slit of the analyser are counted by a channeltron. Without use of the deflection unit, the incident and scattered beams have a 6° -angle with respect to the normal of the surface.

In a HREELS system the momentum resolution is determined by the angular acceptance of the spectrometer and by the geometry of the experiment. Hence, for high impact energies and big deflection angles, the window in momentum space over which data are integrated can become very large, thus introducing some artifacts in the measurement results, especially if the inelastic cross section of the losses varies very rapidly in such a range [54]. In the case of an ELS-LEED device, the position change in momentum space is achieved by an electronic deflection of the electron beam, allowing a better momentum resolution.

The transfer width of the ELS-LEED instrument was determined to be 150nm [53], corresponding to a momentum resolution of 0.004 \AA^{-1} , but is limited in general by the quality of the surface. The best energy resolution reached with the ELS-LEED is 4.3meV. In the present work the best reached was 8meV on Si(111)-surface and 13meV on vicinal Si(001)-surface. The energy and momentum conservation are given by

$$E_{loss} = E_i - E_s$$

$$\hbar q_{\parallel} = k_s \sin \theta_s - k_i \sin \theta_i , \quad (3.1)$$

where k_i (k_s) and E_i (E_s) are the wave vectors and energies of the incident (scattered) electrons, respectively, and q_{\parallel} the momentum transfer parallel to the surface.

The ELS-LEED offers multiple possibilities for experiment in energy and momentum space. In the SPA-LEED modus, LEED line scans and two-dimensional patterns can be achieved. If the system is switched to HREELS, energy loss spectra can then be performed in nearly any point in reciprocal space. Moreover the device allows to perform angular distribution of inelastically scattered electrons, when a LEED line scans is made from diffracted electrons that have experienced energy changes. One can very precisely follow the dispersion of elementary excitations in a short range near $q_{||}$.

3.3 Manipulator and sample holder

In order to deal optimally with the system studied in this work a new manipulator was build. It is a commercial cryogenic system (from Janis Research ST 400 UHV supertrans system) allowing cooling at both liquid nitrogen (LN_2) and liquid helium (LHe) temperature. The cryogenic temperature was controlled via a silicon diode mounted on the bottom of the cooling rod.

The manipulator (type MECA 2000) was incorporated to a differential pumped rotating feedthroughs. It enables a 360° rotation around the manipulator axis and translation in the horizontal plane. This is of importance because the sample has to change its position during the experiment. A thin gold foil was put between the lower end of the manipulator and an adaptation block with four fingers, for electrical and thermal contacts. The sample temperature was measured via two Ni-NiCr thermocouples mounted on one of the finger in front of the adaptation block.

The sample holder is built to enable sample transfer from the transfer sytem to the main chamber. It is made of four molybdenum (Mo) blocks electrically isolated from each other. On the sample side of the sample holder two titanium (Ti) pieces, on which the sample is lying, were mounted. The sample is then fixed to the Ti-pieces by Mo-plates. To increase the electrical contact, high doped silicon pieces (spacer) are inserted between the sample and Mo-plates, and the sample and Ti-pieces.

In the present work, LN_2 was used for cooling the sample and the lowest temperature at the sample was $\approx 120\text{K}$.

3.4 Dysprosium evaporator

In order to grow Dy silicide on Si, a non-commercial molecular beam epitaxy (MBE) evaporator was used. Fig. 3.3 shows different views of the evaporator. 99.9% pure Dy was contained in tantal crucible (f), which was heated by electron bombardement. The crucible and the filament (g) are housed in a water cooled (b) cooper (Cu) cylinder (a), so that the heat radiation does not lead to warming up of the surrounding. In the evaporating process the crucible was set at a voltage of 1 kV and the filament was heated to reach the adequate emission current of 8 to 14 mA. The evaporation rate was

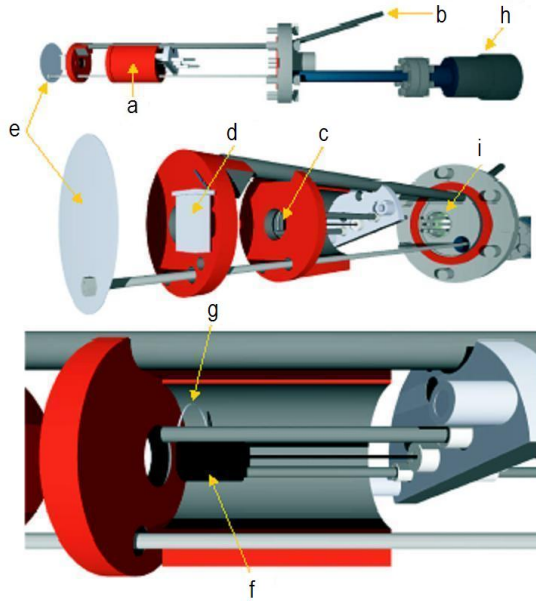


Figure 3.3: MBE-evaporator. See text for detailed description of the different notations

controlled by a 10 MHz quartz microbalance (d) and the evaporation time was controlled by the opening and closing of a shutter (e) in front of the evaporator. For the rest of the notation, (c) represents the opening in the Cu-cylinder through which Dy is evaporated, and (h) and (i) are the feedthroughs for electric contacts and for rotating the shutter.

Dy-evaporator calibration

Dy-silicide has been grown by MBE deposition of Dy on a Si substrate. Due to the lack of an external gun, it was not possible to calibrate the evaporator using the intensity oscillation during the epitaxial layer growth. The high oxidation potential of Dy did not allow to move continuously the sample from the evaporator to the ELS-LEED device. The calibration was then made using an approximation of the frequency change in the quartz microbalance, if one atomic layer of Dy would cover it.

The frequency change Δf in the quartz is proportional to the deposited Dy amount

$$\Delta f = C \cdot \rho$$

where C is the quartz constant given by $C=3.764 \text{ Hz } \text{\AA}/u$, and ρ is the mass density in atomic mass unit u . The frequency change of 54.7 Hz per Dy monolayer was obtained. The geometry factor was calculated to be around 4 by measuring the crucible-to-quartz and crucible-to-sample distances. Using this calibration the deposition of one Dy monolayer corresponded to $\Delta f = 218 \text{ Hz} \pm 20\text{Hz}$ (an error of 9 %).

In order to perform a better calibration, we used the LEED structure of the 1×1 LEED pattern of the monolayer Dy-disilicide DySi_2 as a fingerprint, when grown on Si(111). The transition from the 1×1 reconstruction to the multilayer $(\sqrt{3} \times \sqrt{3})\text{R}30^\circ$ was clearly observed at $\Delta f_{\text{Si}(111)} = 160$ Hz.

The frequency change for 1ML Dy deposited on Si(001) was obtained by dividing $\Delta f_{\text{Si}(111)}$ by a factor of 1.15, equivalent to the ratio of the atom density on Si(111) surface ($1\text{ML} = 7.8 \times 10^{14}$ atoms/cm²) to that on Si(001) surface ($1\text{ML} = 6.78 \times 10^{14}$ atoms/cm²). This correspond to $\Delta f_{\text{Si}(001)} = 140$ Hz.

Chapter 4

Sample preparation

4.1 The silicon substrate

In the periodic table of elements silicon (Si) is the second element of the group IV. It is a semiconducting material of the electronic configuration $[\text{Ne}]3s^2p^2$. The bulk crystal has a diamond structure, which results from the sp^3 hybridization of the valence electrons. Each atom is covalently bonded to four nearest neighbors in tetrahedral coordination of 109.5° bonding angle and 2.35\AA bonding length. The Si space lattice is face centered cubic of lattice constant 5.43\AA [55] The used silicon surfaces, the

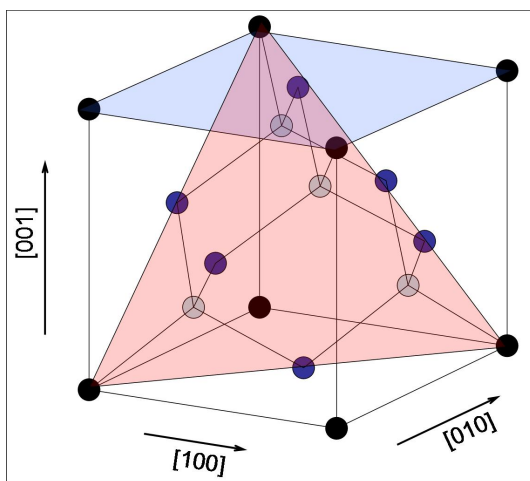


Figure 4.1: Space crystal lattice of silicon. The rectangular and the triangular surfaces represent the (001) and the (111) silicon surfaces, respectively

Si(111) and Si(001) are sketched in fig. 4.1, together with the silicon crystal lattice. In the following the two surfaces and dysprosium will be described in more detail.

4.1.1 The Si(111) surface

Cleavage of Si along the (111) direction leaves at each atom a free electron, the so-called dangling bond. These are energetically unfavorable, therefore the surface reorganises into a 2×1 -superstructure, and thus reduces the surface energy. By heating the sample from RT to high temperature, the surface undergoes an intermediate 5×5 reconstruction and converts irreversibly into a 7×7 -phase upon heating at temperatures from 210 to 600°C [56]. The 7×7 reconstruction is the lowest-energy structure for the Si(111) surface. By heating the sample above 850°C, a reversible $7 \times 7 - 1 \times 1$ transition occurs, in which the formal structure can be restored upon slow cooling of the 1×1 surface through the region of the transition temperature [57].

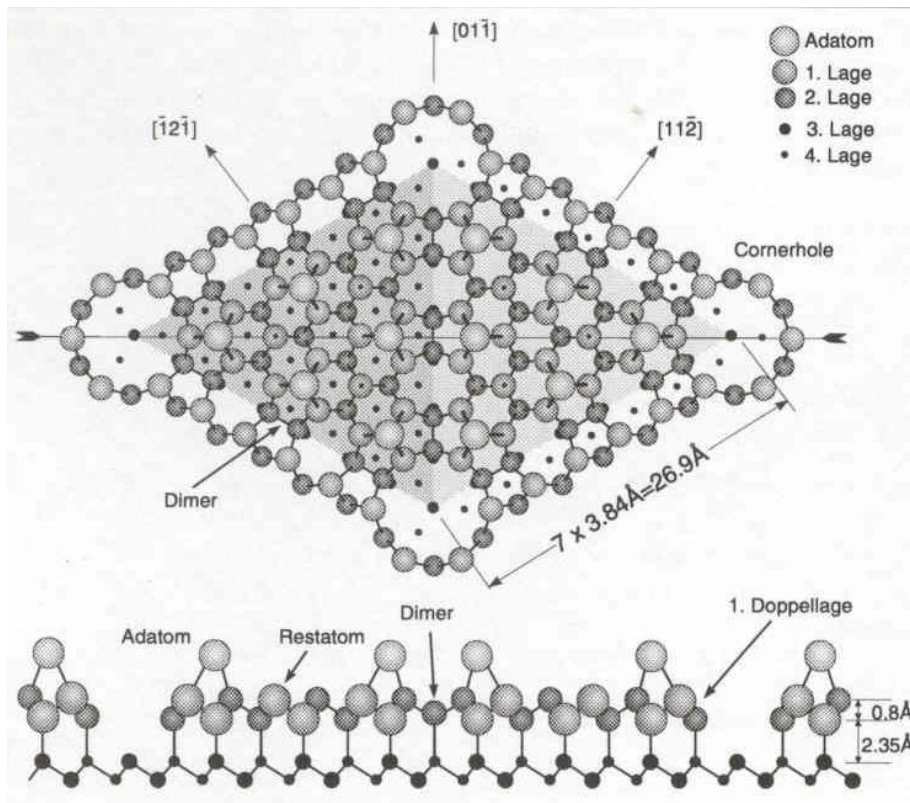


Figure 4.2: DAS-Model of the Si(111) 7×7 -surface structure. From ref. [58]

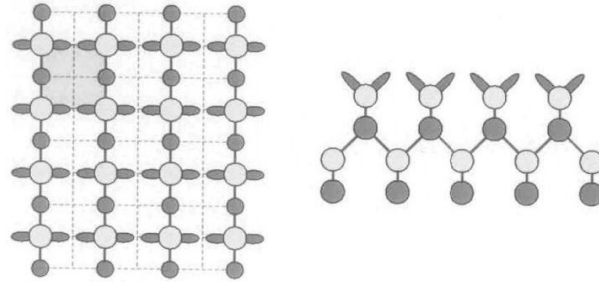
The Si(111)- 7×7 reconstructed surface has been the widely used among Si surface orientations. Discovered in 1959, it remained unclear until Takayanagi *et al.* proposed the dimer adatom stacking-fault (DAS) model [58]. The model, still valid up to now, is illustrated in Fig. 4.2. In the top view atoms on (111) layers of decreasing heights are indicated by circles of decreasing sizes. Each unit cell of the 7×7 reconstruction possesses 12 adatoms, 9 dimers and 19 dangling bonds are remaining, compared to 49 dangling bonds available after cleavage. The half on each unit cell has a stacking fault.

The electronic structure of bulk Si differs from that of the Si(111)- 7×7 surface. On the one hand, bulk Si is semiconducting, with a band gap of 1.12eV at 300K between the valence and the conduction band. On the other hand, each Si(111)- 7×7 unit cell has 19 danglings bonds. If one assumes that an independent-particle picture is valid, this odd number of dangling bonds implies the existence of at least one partly filled band of surface states, thus making this surface metallic [59]. This metallic nature is challenged by the fact that one can not completely exclude the presence of a small band gap between filled and empty states due to the large size of the 7×7 unit cell. Evidence of surface states on Si(111)- 7×7 surface was obtained using several methods. In particular, using HREELS, Backes *et al.*[60] found broad loss spectra in the elastically scattered electrons with high background intensities up to several hundreds meV of electron energy-loss. This was assumed to be resulting from excitations described by a Drude-type dielectric response of a metallic surface-state band. The assumption was supported by the fact that the sample exposure to H₂ narrowed the elastic peak and caused the background to disappear, thus creating a band gap. Ibach *et al.* [28] proposed excitation of a conduction-band plasmon of very small frequency to explain the broadening of the elastic peak. It was furthermore assumed that the background was due to interband transitions between the many subbands possibly existent on the 7×7 -Si(111) surface. The argumentation was disputed by Froitzheim *et al.* that performed EELS measurements on both cleaved and polished Si(111)- 7×7 surface. They claimed that the high background loss intensity could be accounted for by carbon contamination that induced a band bending [61].

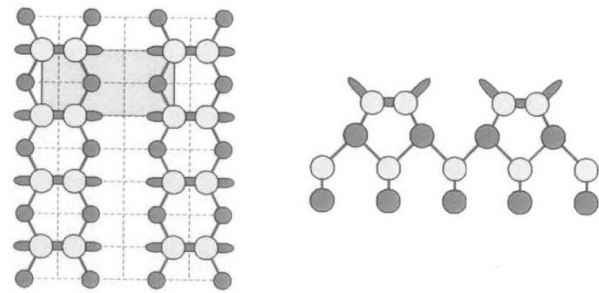
4.1.2 The Si(001) surface

When the silicon is cleaved to create the Si(001)-surface, the surface atoms form a periodic square lattice of lattice constant 3.84Å. On the bulk side the surface atoms are bonded to two atoms. But on the vacuum side the remaining two bonds are left free. These are the so-called dangling bonds. As for the case of the cleaved Si(111)-surface, the dangling bonds (Fig. 4.3 in (a)) represent energetically unstable surface states. Thus the surface atoms undergo a reconstruction, in which the atoms in the surface top layer shift from their original positions in the bulk to bond to their nearest neighbors (Fig. 4.3 in (b)), therefore minimizing the surface energy. The reduction of the surface energy through additional bondings between silicon surface atoms depends more on the bonding angle and less on the bonding length. This results from the fact that the additional bonding is accompanied by an elastic strain, which depends strongly on the bonding length and weakly on the change in the bonding angle [62]. A detailed description of the reconstruction mechanism can be found in the literature [63]. This surface reconstruction occurs just after cleavage, so that the expected cleaved Si(001)- (1×1) can not be observed. The unreconstructed surface can, however, be observed, if for example, the dangling bonds are saturated by an adequate adsorbant, like hydrogen [64]. The surface reconstruction is achieved by dimerisation. Each dimer is generated by two neighboring atoms which form σ and π bonds to each other [65].

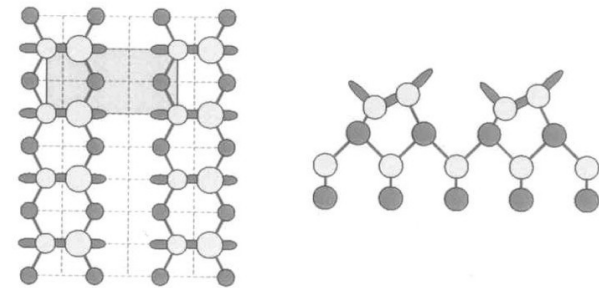
(a) (1x1): truncated bulk



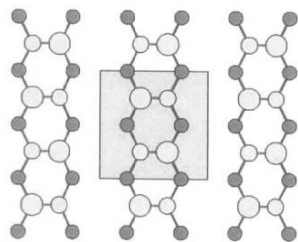
(b) (2x1) symmetric dimers



(c) (2x1) asymmetric (buckled) dimers



(d) p(2x2) buckled dimers



(e) c(4x2) buckled dimers

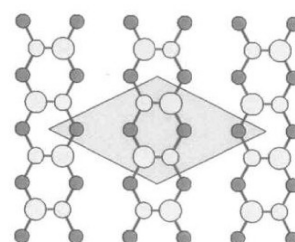


Figure 4.3: Structure models of Si(001) from cleavage to dimer buckling induced reconstruction. The grey region represent the unit cell. From ref. [69]

This results in the well known Si(001)- 2×1 reconstruction. Due to the geometry of the diamond structure the dimers arrange in parallel chains (dimer rows), inducing the anisotropy of the Si(001)- 2×1 reconstructed surface. One consequence of the anisotropy is the diffuse of Si-atoms which is along the dimer rows hundred times larger than across them [66, 67].

The orientation of the dimer can also have an angle with respect to the surface plane. In that case the dimer is called asymmetric or buckled and one atom in the dimer is higher than the other with respect to the surface plane. It was proposed that, in the buckled dimer, a charge transfer occurs from one dimer atom to the other, resulting in partially ionic dimer atoms, in compatibility with the semiconducting band structure of the surface revealed by angle-resolved photoemission spectroscopy [68]. If the buckling angle is the same in all dimers and rows (Fig. 4.3 in (c)), then the long-range ordering results in a 2×1 -periodicity as in the case of symmetric dimers. Theoretical approaches have confirmed that the 2×1 -buckled supersymmetry leads to a minimization of energy in the system. However the exact value of the energy difference diverges in the literature, running from 0.12 eV [69] to 0.02 eV [70]. If the last value is considered, it would mean that both reconstructions coexist at RT. Further variation in the dimer atom buckling can result in $p(2\times 2)$ and $c(4\times 2)$ symmetries (Fig. 4.3 in (d) and (e)). The energy changes for the different symmetries can be found in [69]. The energy difference is very small between $p(2\times 2)$ and $c(4\times 2)$, implying that they can be distinguished from each other only at low temperature. In fact, at RT, due to the rapid phase transition between them, their average results in 2×1 reconstruction. It must be noted that the presence of defects on the surface can suppress the oscillation motion of the buckled dimers, so that the dimer asymmetry related reconstruction might be observed even at RT.

At this level a differentiation in the consideration of the Si(001) surface will be introduced. The latter is normally considered as flat in opposite to the vicinal Si(001) miscut with a few degree. We will describe the vicinal Si(001) with 4° miscut towards Si[$1\bar{1}0$].

4.1.2.1 The flat Si(001)-surface

On the flat Si(001), besides the 2×1 reconstruction, LEED experiments show also a 1×2 reconstructions. This illustrates the coexistence of two domains with perpendicular dimer rows, as a result of the bonding geometry that rotates by 90° on the successive layer in the diamond crystal structure. The domains are equally populated and are separated by single atomic steps. The dimer rows are thus oriented in the $[110]$ -direction on one terrace and in the orthogonal $[1\bar{1}0]$ -direction on adjacent terrace. Two kinds of steps emerge and are named S_A and S_B [71] (Fig. 4.4). In the case of S_A -steps, the dimer rows on the upper terrace are parallel to the step, whereas for S_B steps, the dimer rows are orthogonal to the steps. The S_A steps have been calculated to have the lowest energy [71].

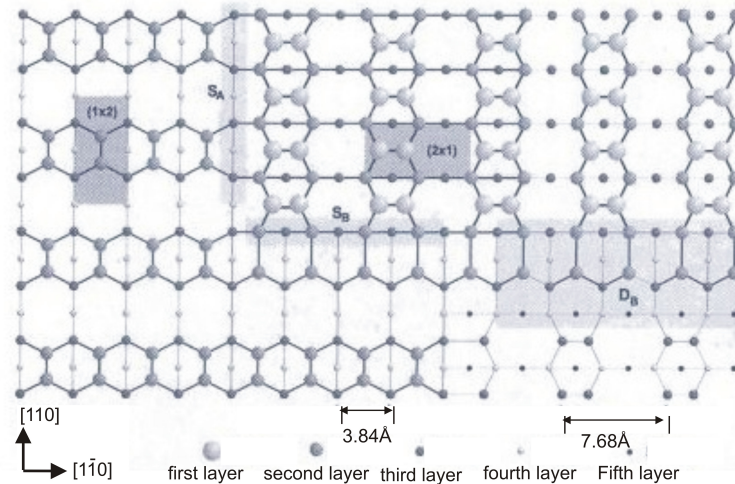


Figure 4.4: Structure model of Si(001) surface with description of the step notation. From ref. [71]

4.1.2.2 The vicinal Si(001) with 4° miscut

Vicinal Si(001) are created when the crystal is cut with a small angle to the direction of the plane of symmetry. The surface morphology is made of flat terraces separated by steps. Diffraction experiments have shown that there is a continuous transition from two domains (observed on the flat Si(001)) to single domain for misorientation angles from 1.5° to 5°. The single domains are separated by double atomic steps with can be named D_A and D_B in analogy to the single atomic step notation. The D_B steps have the lowest formation energy [71]. The angle of 2° has been determined as the critical for the equilibrium transition between single and double steps [72]. With increasing miscut angle the stability of the double steps increases.

4.1.3 Substrate preparation

All used samples in the present work were obtained from commercial Si wafers. The latter were already polished on one side, 300 μm thick and for both (111) and (001) surface orientation very low doped ($\geq 1000 \Omega\text{cm}$). Rectangular shaped samples were cut manually using a diamond cutter. The length was fixed to 17 mm and the width varying from 7 to 10 mm. The samples were rinsed with propanol prior to mounting on the sample holder .

Before removing the native oxide, the sample holder was first degassed at 630°C in UHV for 6 hours. At that temperature the native oxide is still stable and protects the

surface from adsorption of other rest gas molecules. The native oxide was then removed by a series of flash-heating the sample by direct current up to 1200°C while keeping the pressure lower than 1×10^{-9} mbar. The temperature was followed using an infrared pyrometer.

The formation of the Si(111)- 7×7 reconstructed surface was obtained by quickly decreasing the temperature from 1200°C to 830°C, holding there for 10min and then slowly decreasing at a rate of 1°C / sec till 650°C and from there at 10°C/sec.

A high attention has to be given to the preparation of Si(001) surface due to its high reactivity and the defect dependent surface reconstruction. A well ordered Si(001)- 2×1 surface was obtained by quickly decreasing the temperature from 1200°C to 900°C and then slowly decreasing the temperature to a rate of 1°C/sec. In the case of vicinal surfaces, the step direction was kept parallel to the current direction to minimize the step destruction by electromigration.

The cleanness of the sample was mainly checked through the sharpness of 2D-LEED patterns. In the beginning, AES has been used to insure that the used method was reliable.

4.2 Dysprosium silicide

Dy is the 66 element in the periodic table of elements. As other rare-earth(RE) elements, Dy forms silicide when it reacts with Si. Comparing the kinetics of silicide formation, the RE elements belong to a separate, distinct class amongst the transition metal silicide [73]. Several stoichiometries are observed in RE silicide: RE_5Si_3 and RE_5Si_4 in metal rich form, monosilicide $RESi$, and disilicide of varying composition $RESi_{2-x}$ with $x \approx 0.33 - 0$ (from RE_3Si_5 to $RESi_2$).

The metal rich silicides crystallize most frequently in the Mn_5Si_3 and Sm_5Ge_4 structures, and the monosilicides crystallize either in FeB or in CrB structures [74]. These metal rich silicide structures, formed at RT, are not stable when the RE overlayers are annealed at high temperatures. They all undergo transitions to silicon rich silicides structures of type $RESi_{2-x}$. The latter crystallizes in three different closely related structure types, which are dependent on the nature of the RE, the value of x and on the temperature: tetragonal ($ThSi_2$) for $x \approx 0$, hexagonal (AlB_2) for the RE_3Si_5 stoichiometry, and orthorombic ($GdSi_2$) for intermediate compositions [75].

Bulk Dy-silicide has the hexagonal AlB_2 structure type. Si and Dy atoms are arranged in hexagonal alternating layers. Dy atoms form centered hexagonal structures and the Si layers (between the Dy hexagons) form graphite-like hexagons with one additional vacancy in each hexagon [10, 76, 77, 78, 79]. The top surface layer of Dy silicide is formed of buckeled Si atoms, similar to the 1×1 -Si(111)-surface. Each Dy atom is surrounded by 12 Si atoms at 3.019Å and each Si atom by 6 Dy atoms at 3.830Å.

Dy silicide hexagonal unit cell is shown in Fig. 4.5 [80]. It has a lattice mismatch of -0.3 % compared to the Si(111)-unit cell, allowing the epitaxial growth of Dy silicide films. As already investigated, Dy silicide undergoes several Dy coverage dependent

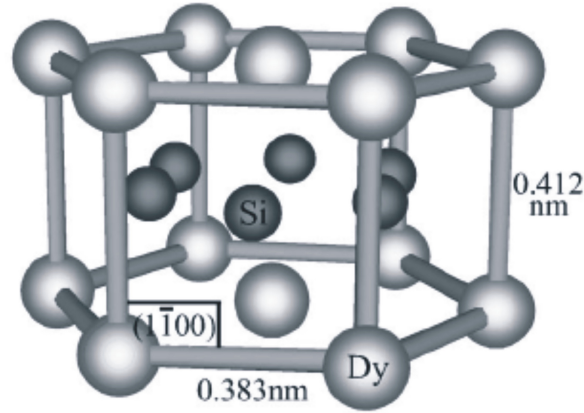


Figure 4.5: Unit cell of DySi_2 in the hexagonal AlB_2 type symmetry. From ref. [80]

reconstructions. Indeed at lower Dy coverage around 0.5ML a $(2\sqrt{3} \times 2\sqrt{3})\text{R}30^\circ$ -reconstruction has been resolved and characterised using STM [23]. At submonolayer coverage the $(2\sqrt{3} \times 2\sqrt{3})\text{R}30^\circ$ is mixed to a 5×2 -chain-like structure, with 60° -rotating domains. At the monolayer coverage a hexagonal DySi_2 can be formed. It has a 1×1 -periodicity and has been characterized by Engelhardt *et al.* using STM[23]. It is a defect free layer in contrast to the multilayer $\text{DySi}_{1.7}$. The defect consists of a Si-atom vacancy in every Si graphite-like hexagon. This defect occurs also in the multilayer regime where the Si-vacancies are rotating about 60° . The ordering of the vacancies is responsible for the $(\sqrt{3} \times \sqrt{3})\text{R}30^\circ$ -reconstruction.

Hexagonal Dy silicide grows on the square lattice of the Si(001) surface with the $(1\bar{1}00)$ plane parallel to Si(001), and $[0001]$ parallel to one of the Si $\langle 1\bar{1}0 \rangle$ direction on Si surface. This results in anisotropic lattice mismatch along the two perpendicular $\langle 1\bar{1}0 \rangle$ directions of -0.3 % and 7.3 %, respectively. Due to strain induced by the large lattice mismatch, highly elongated islands grow in the direction of the small lattice mismatch. The growth conditions can be tuned to transform the elongated islands in structures with high aspect ratios or nanowires [19].

Chapter 5

ELS-LEED on DySi₂ / Si(111)

Before studying the characteristics and properties of Dy-silicide on Si(001) surfaces, it is simple to begin with Si(111) as substrate. One of the main reason is that, due to the small lattice mismatch between Si(111) and Dy-silicide, the growth of epitaxial flat overlayer is expected, which would permit higher ELS-LEED intensities. Moreover, by means of photoemission spectroscopy it has been possible to distinguish between the monolayer DySi₂ and the multilayer Dy₃Si₅ structurally, electronically and chemically [10, 11]. This can be used as a fingerprint for evaporator calibration. All these make the Si(111) substrate a better starting point than the Si(001) surface.

In the following, ELS-LEED study of Dy-silicide grown on Si(111) will be presented. For the first time, we present HREELS results on the monolayer DySi₂ with a 2D-plasmon dispersion.

5.1 The clean Si(111)-7×7 substrate

The Si-substrate was prepared as described in section 4.1.3. A 2D-diffraction pattern of the clean sample is given in Fig. 5.1. The sharpness of the spots are an indication of the long-range ordering of the surface atoms. Fig. 5.2 shows HREELS spectra from the clean Si(111)-7×7 surface taken at 120 K and at RT. They both present a broad shoulder at the energy loss side of the spectra. This shoulder is the metallic Drude tail, in good agreement with the metallic nature of the Si(111)-7×7 surface. A slight broadening of 1 meV occurs when the temperature increases.

5.2 Dysprosium silicide properties

5.2.1 Dysprosium silicide growth

DySi₂ films have been prepared by depositing Dy by means of MBE techniques. This evaporation technique was already described in section 3.4. Reaction between silicon and dysprosium already occurs at room temperature [81] but the quality and structure

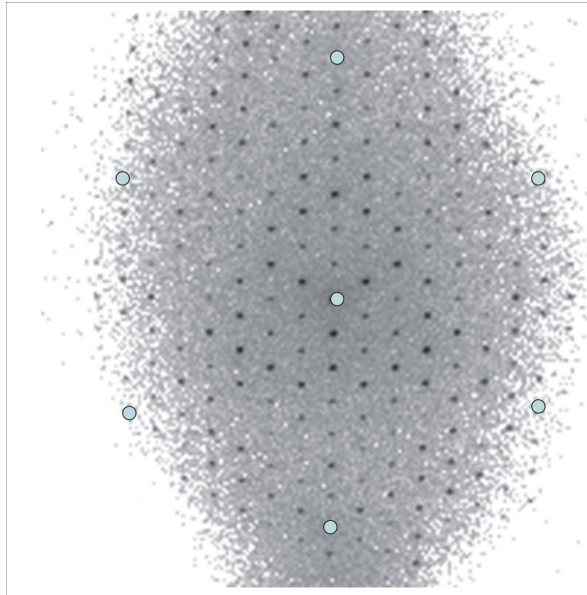


Figure 5.1: Diffraction pattern of the Si(111)- 7×7 surface reconstruction. The dark-green point are illustrating the 1×1 -unit cell

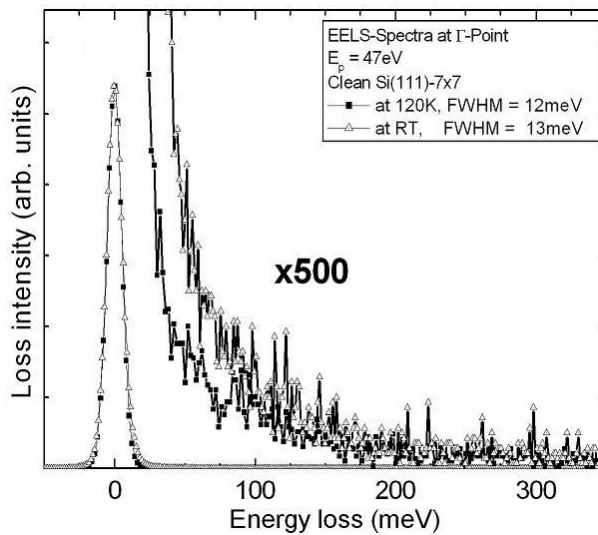


Figure 5.2: Electron energy loss spectra on the clean Si(111)- 7×7 taken at 120K and RT, respectively. $E_p=47$ eV

of the Dy-silicide depends on the growth condition. In the present work, the silicide preparation was performed by depositing Dy at RT followed by annealing at temperature ranging from 400 to 600°C or by depositing Dy at elevated substrate temperature (400 - 600°C), mostly followed by postannealing.

Although relatively stable in air at RT Dy has a very high oxidation level in the vapor phase. An adequate environment was achieved by working under UHV-condition with a base pressure of 2×10^{-11} mbar. During film preparation the pressure was better than 3×10^{-10} mbar. Thus we were able to protect the silicide film from oxidation during growth.

ELS-LEED measurements were mostly done either at 120 K or at RT. As illustrated in

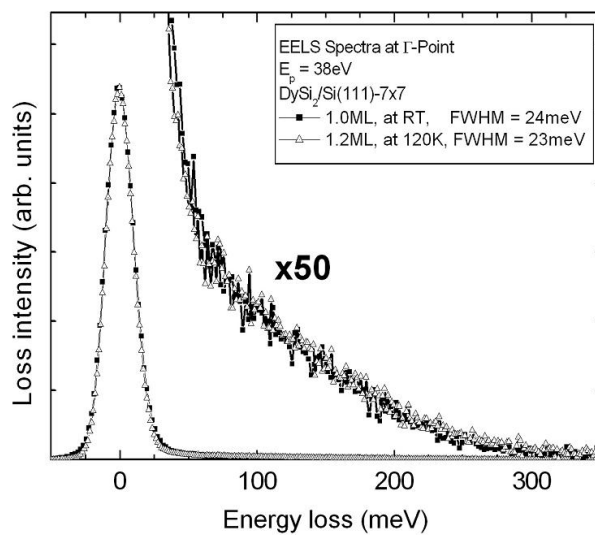


Figure 5.3: Electron energy loss spectra on 1ML Dy-silicide at RT and on 1.2ML Dy-silicide at 120K. $E_p=38$ eV

Fig. 5.3 no substantial differences occur due to temperature variation between 120 K and RT. We will therefore skip specifying the sample temperature during the measurements.

As expected, Dy-silicide grew crystalline as revealed by LEED pictures. At the monolayer DySi₂ coverage, LEED pattern showed the typical 1×1 -periodicity. Besides, a HREELS spectrum at Γ -point on that surface has been taken. It is compared to the spectrum taken also at Γ -point on clean Si(111) surface as illustrated in Fig. 5.4. The strong enhancement of the Drude tail on DySi₂ compared to clean Si(111) substrate reveals the metallicity of the silicide overlayer.

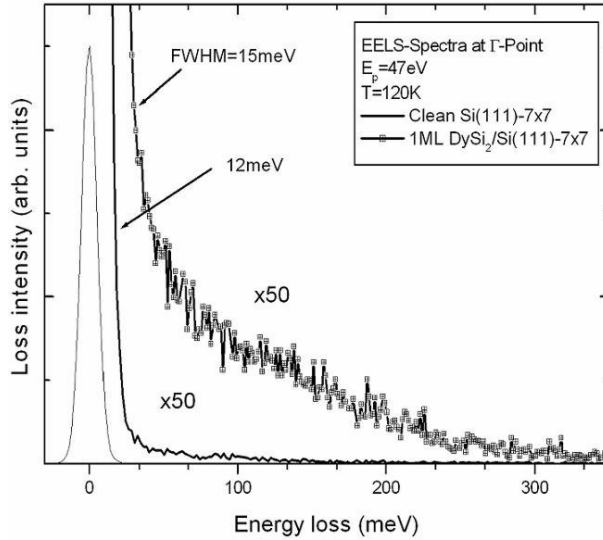


Figure 5.4: Electron energy loss spectra on clean Si(111)- 7×7 surface and with 1ML Dy-silicide. $E_p=47$ eV

5.2.2 Silicide surface reconstruction

By growing Dy-silicide on Si(111) as described above, we were able to observe, by means of electron diffraction, all Dy-silicide surface reconstructions available in the literature. Moreover other reconstructions that are not yet reported for Dy-silicide were seen. In the following we are going to present some parameters on which the silicide film structures are depending on.

5.2.2.1 Coverage dependence

Fig. 5.5 show SPA-LEED line scans of various Dy-silicide coverages. Scans in (a)-(b) are made along the ΓK - ΓM -directions of Si(111)-SBZ, respectively. On the bottom of each set of graphs line scans of the clean Si(111)- 7×7 reconstruction are given for the two crystallographic directions. As can be seen at Dy coverage of 0.28ML, low Dy coverage does not destroy completely the 7×7 structure. Instead small islands with $(2\sqrt{3}\times 2\sqrt{3})R30^\circ$ reconstruction are formed, leaving some regions of clean Si(111). SPA-LEED line scans show weaker 7×7 -peaks than for the clean substrate. In the ΓM -direction, between the 2nd and the 3rd order spots, an additional spot associated to the $(2\sqrt{3}\times 2\sqrt{3})R30^\circ$ periodicity can be seen. Increasing Dy coverage induces a 5×2 reconstruction. At this stage we assume that 2D DySi₂ islands have already formed, as already reported from STM measurements, supposed to be dominant around 1ML [11]. This is however very dependent on the initial growth condition, especially on the substrate temperature. A 2D-LEED pattern taken from a silicide film around 1ML Dy coverage shows no spots from the $(2\sqrt{3}\times 2\sqrt{3})R30^\circ$. Their disappearance coincides

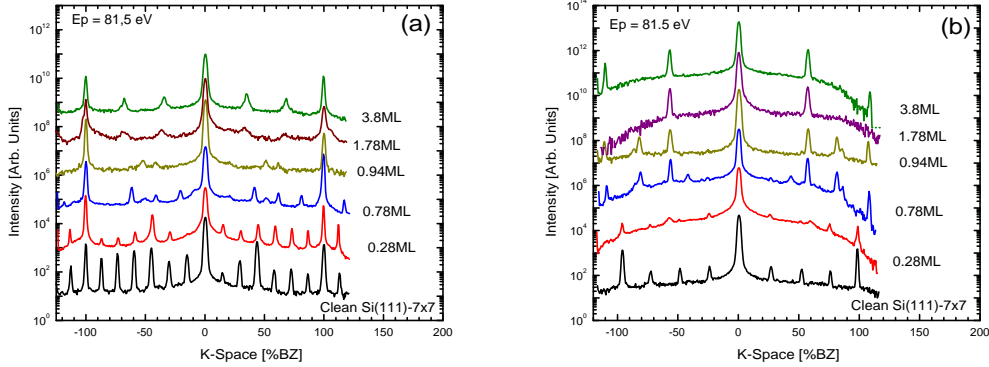


Figure 5.5: SPALEED line scans of in the (a) Γ K-direction and (b) Γ M-direction of the Si(111)-SBZ. Each line scan is shown with the corresponding Dy-silicide coverage.

with the appearance of the $(\sqrt{3} \times \sqrt{3})R30^\circ$ structure, associated to 3D silicide islands. Depending on the growth condition the 5×2 and $(\sqrt{3} \times \sqrt{3})R30^\circ$ reconstructions can coexist in 2D-LEED patterns of 0.8 to 1.3ML. Extreme growth conditions like high substrate temperature or creation of step bunches resulted in 3×3 and 5×1 structure periodicities. Such structures are not reported for Dy-silicide but they were found on other rare-earth silicide in conditions that will be discussed later.

5.2.2.2 Dependence on the substrate temperature

RT deposition of a thin Dy layer on Si(111) results in a crystalline film. A 2D-diffraction pattern of a thin Dy layer deposited on Si(111) at RT shows a diffuse 1×1 superstructure. There is no trace of the Si(111)- 7×7 reconstruction. This reveals that the epitaxial film is not yet well organised. A metal-rich silicide formation at the interface layer can be expected [81]. More diffuse and much less intense 1×1 spots are obtained when Dy is deposited at low temperature (120 K). In both cases high quality silicide can then be achieved by annealing the film at temperature of 400-600°C. Dy-silicide films were also achieved by depositing Dy on a hot Si(111) surface. The substrate temperature was mainly at 500-600°C. After deposition the sample was annealed at the deposition temperature in order to achieve a full silicide formation.

Fig. 5.6 (left) shows a 2D-LEED pattern of a 0.9ML thin DySi₂ grown on a 500°C hot Si(111) substrate followed by a 10 min postannealing process. The arrows **a**, **b** and **c** show several features representing structural reconstructions. Line scans along the Γ K and Γ M directions of the SBZ (fig. 5.6(right)) help us to get more insight in that structure. The 1×1 -DySi₂ unit cell is shown by solid lines on the right side for the two direction. The upper LEED spectrum is taken along the Γ M-direction. The dotted lines represent a periodicity that can be recognized as the $(2\sqrt{3} \times 2\sqrt{3})R30^\circ$

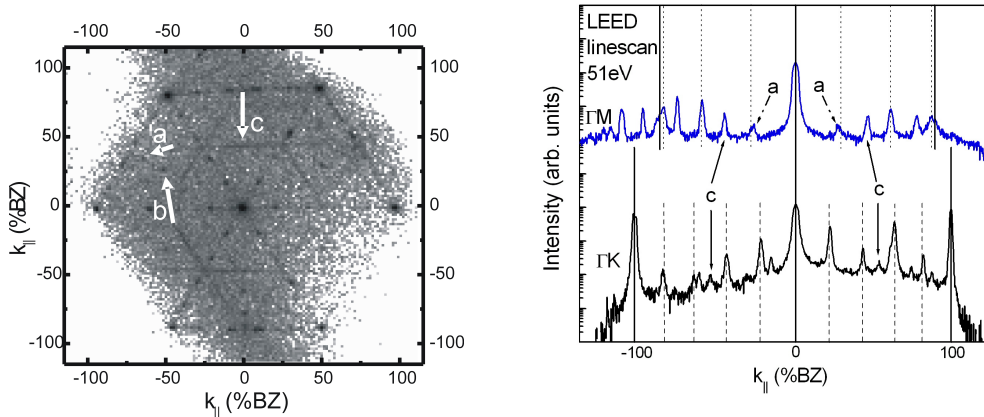


Figure 5.6: 2D-LEED pattern (left) and LEED line scans (right) of 0.9ML DySi₂ grown on Si(111)-7×7 held at 500°C.

reconstruction (**b**-arrow). Areas of the clean 7×7-clean Si(111) are still present on the surface as showed by the **a**-arrow. The **c**-arrow can be clearly understood if one considers the lower line scan in the Γ K-direction. Dashed lines are helping to identify domains with 5×-periodicity. If we take the streaks into account this gives out rotational 5×2 domains.

We have performed also deposition of 0.9ML Dy at RT on Si(111)-7×7. The sample was thereafter annealed at 500°C for 30min. Contrary to what was obtained before, the 2D-LEED showed intense 1×1-spots and LEED line scans confirmed that no other spots were available. High Dy coverages result in a $(\sqrt{3}\times\sqrt{3})R30^\circ$ and the intensity of their spots is increasing with increasing coverage compared to the intensity of the 1×1-spots.

When grown at 600°C a Dy-silicide film has a structure comparable to the one grown at 500°C. But here the annealing time is of importance. Compared to the 2D-LEED pattern in Fig. 5.6, a film grown at 600°C does not show any rest of clean Si(111) areas if the film is kept at that temperature for less than 1 min after evaporation. But the situation changes after annealing the film 10 min more minutes. In this case LEED-spots from the 7×7-symmetry can be seen. This annealing dependence will be discussed in detail in the following section

5.2.2.3 Annealing temperature dependence

Annealing is an important process in the formation of self-assembled structures. It provides the needed energy for atoms to self-organise in the surface overlayer, resulting in enhanced film quality. In the case of Dy-silicide, we have seen above that RT-deposition and even deposition at high temperature does not necessarily lead to formation of a good quality silicide layer. Nevertheless, while at 500°C the annealing

time is not subject to many fluctuations, one needs to find the optimal annealing time if the annealing temperature is set to 600°C.

Dy, in an amount of nearly 1ML, deposited on Si(111) at RT, followed by annealing the sample at 500°C for a time between 10 and 30min, results in a defect free DySi₂ monolayer, as revealed by bright 1×1-LEED spots. The film is, however, not stable at 600°C. In fact annealing at 600°C for 10min destroys some areas of this structure as shown by LEED line scans with weak spots that can be associated to 5×2- and also to the 7×7-reconstruction of the clean Si(111).

On the other hand, if one considers the same silicide thickness grown on a 600°C-hot substrate and annealed for a short time, the structure is not changed by annealing at 500°C. But additional annealing at 600°C acts as described above.

5.2.3 Electronic structure of DySi₂

HREELS has been used so far to study plasmon dispersion and hydrogen-induced semimetal-semiconductor transition for 2D ErSi₂ on Si(111). In this section for the first time HREELS was used to study the plasmon dispersion for DySi₂ on Si(111).

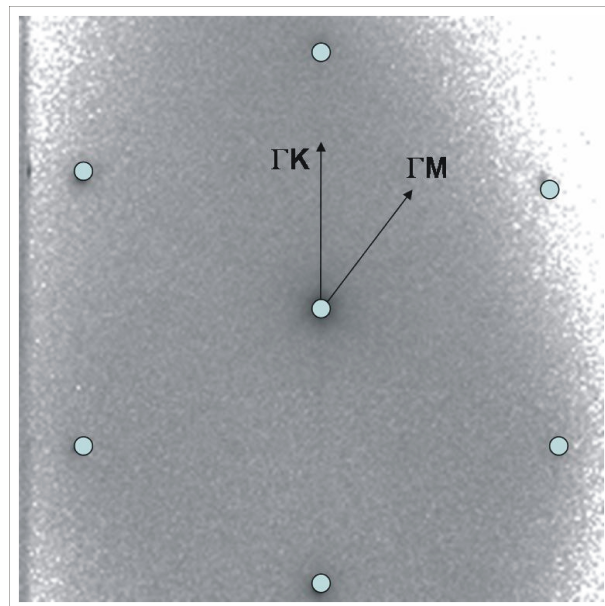


Figure 5.7: (1×1)-LEED pattern of 1 ML DySi₂. The arrows show the direction of HREELS scans

Fig. 5.8 shows energy loss spectra on 1 ML DySi₂ along the Γ -K-direction (see Fig. 5.7 for details on direction). The loss spectra has been shifted upwards with increasing momentum transfer for a better comparison. For momentum transfer $q_{\parallel} \leq 0.014 \text{ \AA}^{-1}$, it was not possible to separate the loss peak from the Drude tail background. For higher q_{\parallel} a single loss peak is seen to form an intense background and to disperse to higher

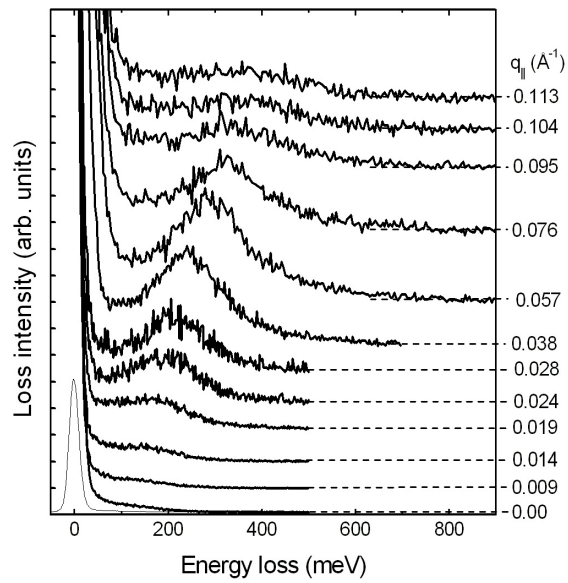


Figure 5.8: HREELS spectra on a 1ML DySi₂ grown at RT and annealed at 500°C. The spectra are taken at $E_p=38$ eV along the Γ -K-direction

energies with increase in the momentum transfer. At $q_{\parallel} \geq 0.095 \text{ \AA}^{-1}$ the loss intensity decreases drastically and after $q_{\parallel} = 0.113 \text{ \AA}^{-1}$ it vanishes out.

5.2.3.1 Origin of the energy losses

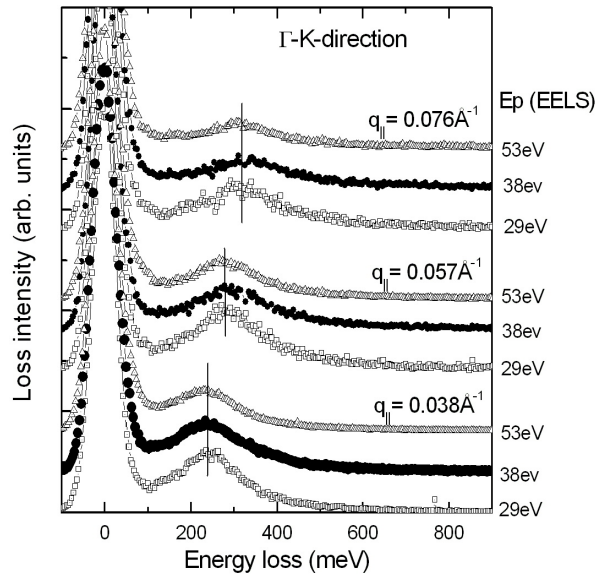


Figure 5.9: EELS spectra of 1ML DySi₂ grown at RT and annealed at 500°C for 3 different energies and for different momentum transfer

To check whether the energy losses are mediated by elementary excitations in the surface area or in the surface space-charge or even in the bulk, we have performed the experiment at several energies, the so-called change in the probing depth. Fig. 5.9 shows set of energy loss spectra performed at three different energies and at several momentum transfers. For a given momentum transfer the loss peak position has no dependence on the energy. This lets us assume that the excitation is strictly localized in the surface topmost layer.

5.2.3.2 2D-behavior of the energy losses

The energy spectra were also performed in the non-equivalent ΓM -direction as shown in Fig. 5.7. The resulting spectra are shown in Fig. 5.10 together with the ones in the ΓK -direction and for different primary electron energies. One can see that the excitation is isotropic on the surface.

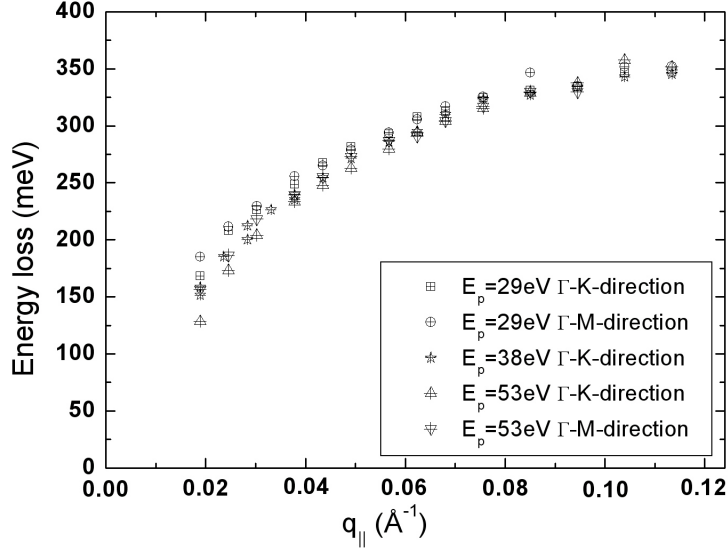


Figure 5.10: Dispersion relation of energy losses of a 1ML DySi₂ grown at RT and annealed at 500°C.

5.2.3.3 Loss intensity and damping

The loss intensity dispersion is shown in Fig. 5.11. The curves present all the same behavior, characterized by a first increase in the loss intensity until the momentum transfer reaches a value $q_{||} \approx 0.04 \text{ \AA}^{-1}$. After reaching the maximum the loss intensity decreases with an identical slope until $q_{||} \approx 0.1 \text{ \AA}^{-1}$ where the slope changes slightly to a smaller decrease. The intensity maxima are increasing with decreasing electron energy, which is in agreement with the dipole character [28]. Moreover the intensity maxima in the Γ K-direction seems to be higher than the maxima in the Γ M-direction. Fig. 5.12 shows the dispersion of the loss width. The extraction of the loss width for momentum transfer $q_{||} \leq 0.024 \text{ \AA}^{-1}$ is accompanied with a large uncertainty. But from that point, the width increases monotonically with increasing momentum transfer until $q_{||} \approx 0.1 \text{ \AA}^{-1}$ is reached. Thereafter the width slope shifts to high width value, revealing enhanced broadening.

5.2.4 Surface with induced step bunches

In the substrate preparing process with direct current heating, it may happen that the cleaning process induces some roughness on the surface. In the following step bunches were created while cleaning the sample due to inhomogeneous heating of the sample. That surface offers then quite similar properties as a vicinal Si(111) surface. The

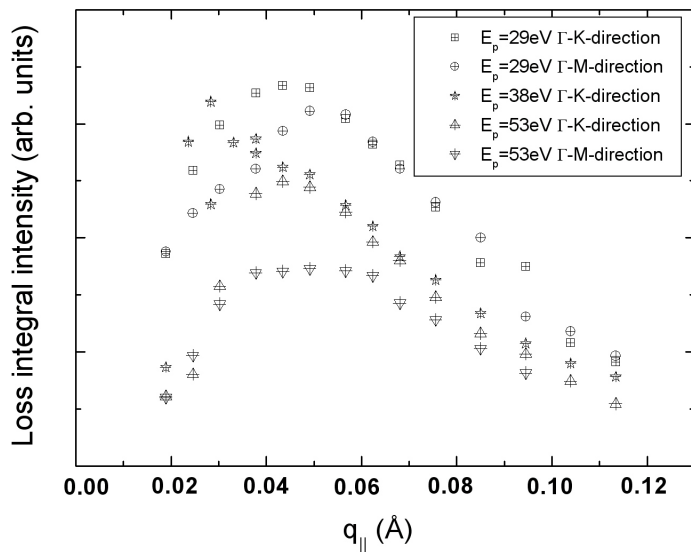


Figure 5.11: Dispersion relation of energy losses of a 1ML DySi₂ grown at RT and annealed at 500°C.

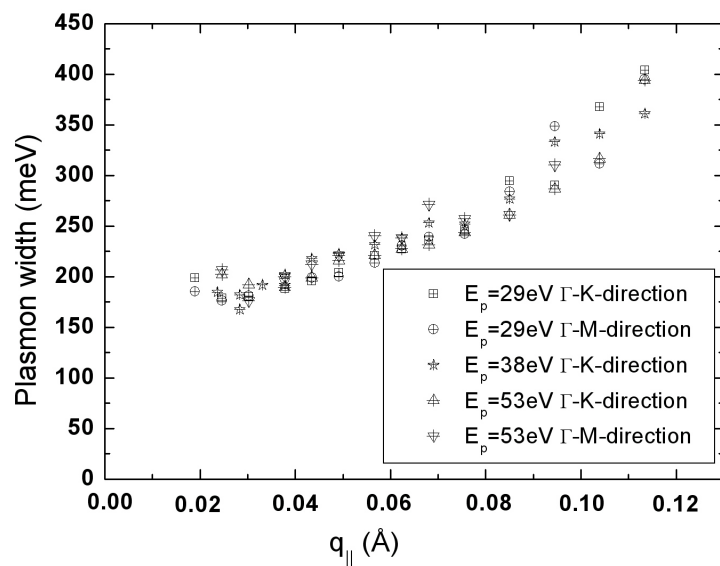


Figure 5.12: Dispersion relation of energy losses of a 1ML DySi₂ grown at RT and annealed at 500°C.

created facet width was calculated to be $\approx 14 \text{ \AA}$ from Fig. 5.13.

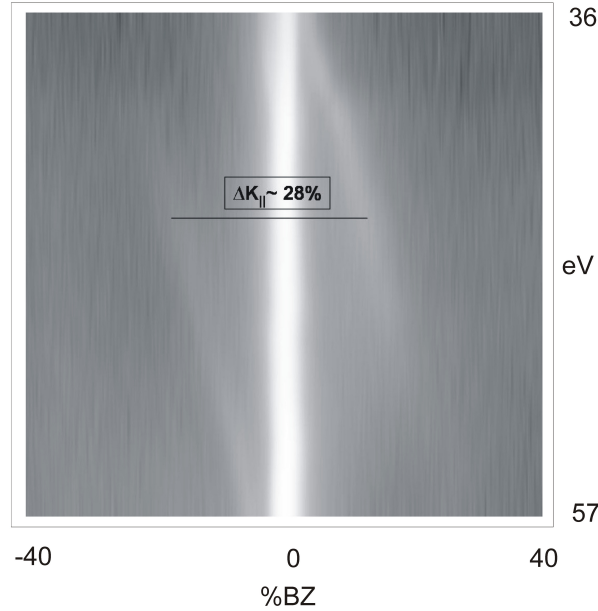


Figure 5.13: Gray scale of a diffraction picture from several line scans taken from 36 eV to 57 eV. The bright parts represent peak intensities.

Fig. 5.14 shows a 2D-LEED pattern of 0.7ML Dy deposited on this substrate held at 600°C . The grown film was annealed for 3min at the same temperature. As one could anticipate, it seemingly vanishing $(2\sqrt{3}\times 2\sqrt{3})R30^\circ$ -spots can be seen from the diffraction picture and they are mixed with 5×2 -spots. The striking difference to flat substrates on which 3-rotational 5×2 -domains are present, the majority of the 5×2 -domains on this faceted surface seems to be 1-directional, with the $5\times$ -periodicity normal to the steps. Under the same growth condition if the Dy coverage is increased to 1.4ML Dy, the $(2\sqrt{3}\times 2\sqrt{3})R30^\circ$ -structure is replaced by a $(\sqrt{3}\times \sqrt{3})R30^\circ$ -periodicity associated to Dy-silicide films with 3D-islands. But even at that coverage the 5×2 -periodicity is still visible, but with decreasing streak intensity.

Coming back to the 5×1 and 3×3 reconstructions encountered before (section 5.2.2.1), one can assume that the 5×1 is just a 5×2 with decreasing streak intensities. The 3×3 has been reported in the case of Eu-silicide, but for higher coverages and for annealing around 900°C [82]. Such reconstruction was not found in the case of Dy. It may be caused by some defect induced reconstruction due to the roughness of the surface. The monolayer DySi_2 has also been grown on the surface shown in Fig. 5.13. Accordingly, a dispersing loss peak can be seen in the ΓK - und ΓM -directions ((a) and (b) in Fig. 5.15). If this directions are considered with respect to the morphology of the surface, the ΓM -direction that we have choosen runs parallel to the long axis of the facets, that is parallel to the steps. The ΓK -direction makes an angle of 30° to the step direction.

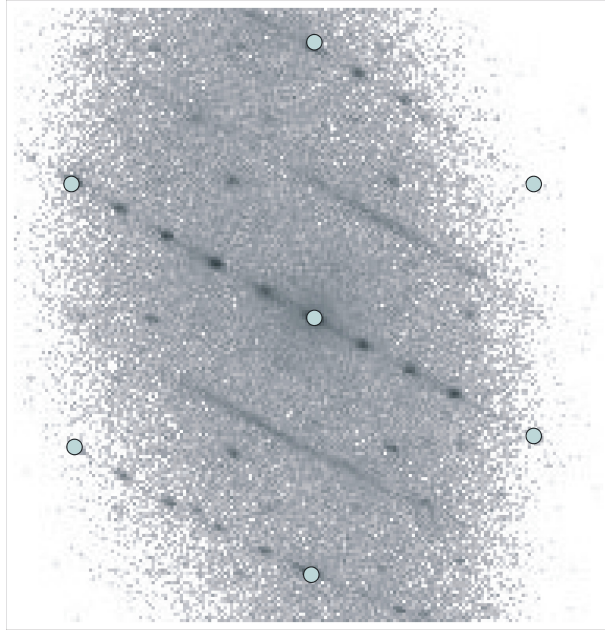


Figure 5.14: 0.7ML DySi₂ grown on Si(111)-7×7 held at 600°C, and annealed for 3min at the same temperature.

No loss peak is clearly seen in the direction normal to the step (c) in Fig. 5.15). This quasi-1D behavior agrees with the Dy-silicide nanowires that have already been reported to grow on vicinal Si(111) [83]

5.2.5 Discussion

We were able to grow the 2D-monolayer stoichiometric DySi₂ with high precision by using the submonolayer and multilayer reconstructions as a fingerprint. LEED patterns showed the usual 1×1 surface. Energy loss experiments were then performed on such a surface. As a result, a 2D-plasmon dispersion were obtained, with the information that the excitation is localized in the topmost surface layer. Now we turn to the fitting of the dispersion relation in order to extract the electronic properties of the involved electron system.

The dispersion curve was fitted by using equation 2.34 [25]. The Si dielectric constant ϵ_{Si} is nearly dispersionless ($\epsilon_{Si}=10.5 - 11.5$) within the frequency range of interest [84]. Due to similarity to the case of 2D-plasmon on Si(111)- $\sqrt{3} \times \sqrt{3}$ -Ag [85], the value of $\epsilon_{Si}=11.5$ was considered. Fig. 5.16 shows the fitting curve of the 2D-plasmon dispersion points. As expected the 2D-plasmon energy vanishes in the long-wavelength ($q_{\parallel} \rightarrow 0$). At small q_{\parallel} the dispersion curve follows the $\sqrt{q_{\parallel}}$ slope of the fitting curve. Between $q_{\parallel} = 0.03 \text{ \AA}$ and $q_{\parallel} = 0.09 \text{ \AA}$ the fitting curve lies slightly lower than the plasma energy, but in a reasonable error range. At $q_{\parallel} \geq 0.09 \text{ \AA}$ both curve deviate

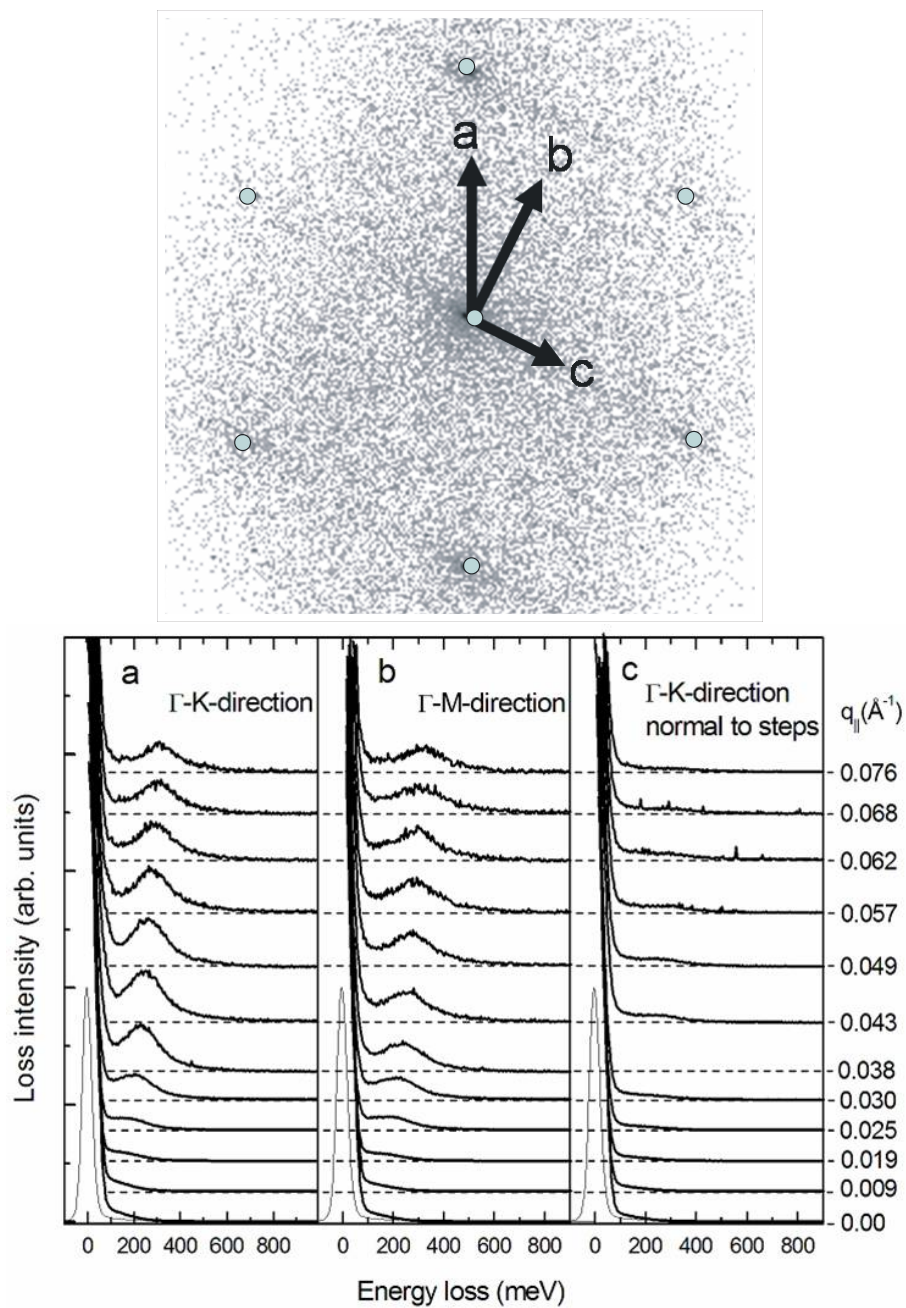


Figure 5.15: EELS spectra of a 1ML DySi₂ grown at RT and annealed at 500°C. The spectra are taken at $E_p=53\text{eV}$ along the SBZ Γ -K, Γ -M and in the direction normal to the steps

Table 5.1: Fitting results: the value from ErSi₂ are given for comparison, from ref. [86, 87]. The value of m^* was fixed during each fitting step and the N was the varying parameter. In Possibility 1, m^* is taken from Photoemission experiments on DySi₂ nanowires [22]. In Possibility 2, a free electron mass is considered. In Possibility 3 the effective mass is fixed at the value given above for ErSi₂.

		N	m / m_0
1.8ML ErSi		$8.7 \times 10^{20} \text{ cm}^{-3}$	4.6
Possibility 1	fixed m^*	$1.36 \times 10^{14} \text{ cm}^{-2}$	0.5
Possibility 2	fixed m^*	$2.70 \times 10^{14} \text{ cm}^{-2}$	1.0
Possibility 3	fixed m^*	$1.25 \times 10^{15} \text{ cm}^{-2}$	4.6

completely from each other, with a significant stagnation of the plasma energy. For

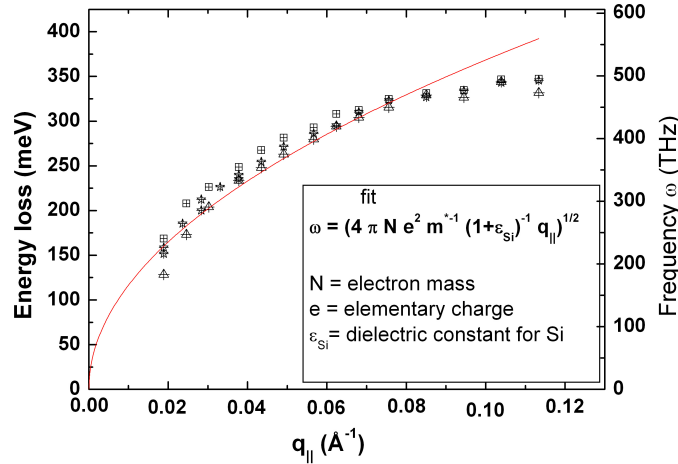


Figure 5.16: Fitting of the 2D-plasmon dispersion curve by using equation 2.34

starting to extract the plasma properties from the fitting process, we took reference to available photoemission data on ErSi₂ for layer thickness of 4.7 Å [86, 87]. The results are summarized in table 5.1.

The obtained values seem to be consistent with a high 2D-electron density. The comparison between ErSi₂ and DySi₂ should not be straightforward because the two silicide layers do not have the same lattice structure: 5 Å ErSi₂ should already have the defected AIB₂, what is not the case for 1ML DySi₂. Nevertheless the ErSi₂ constitutes a good starting point to understand the 2D-plasmon dispersion in DySi₂.

Let's focus our attention to the integral intensity dispersion (Fig. 5.11). The integral intensity increases significantly from zero and reach its maximum around $q_{||}=0.04 \text{ Å}^{-1}$

and begin to vanish. The $q_{||}$ value from which the intensity drops to zero corresponds to the crossing point of the energy dispersion curve and the boundary of the single particle excitation (SPE) continuum [88]. Here exchange effects can make the intensity decline more rapidly and fall to zero at still smaller $q_{||}$. For this case we set the critical $q_{||}^c=0.09 \text{ \AA}$

Unfortunately lack of a basic theory and spectroscopic data describing this system such as the surface band structure does not allow a further reasonable discussion.

Chapter 6

ELS-LEED on DySi₂ nanowires on Si(001)

6.1 Dysprosium silicide on flat Si(001)

6.1.1 Structure of clean Si(001) substrate

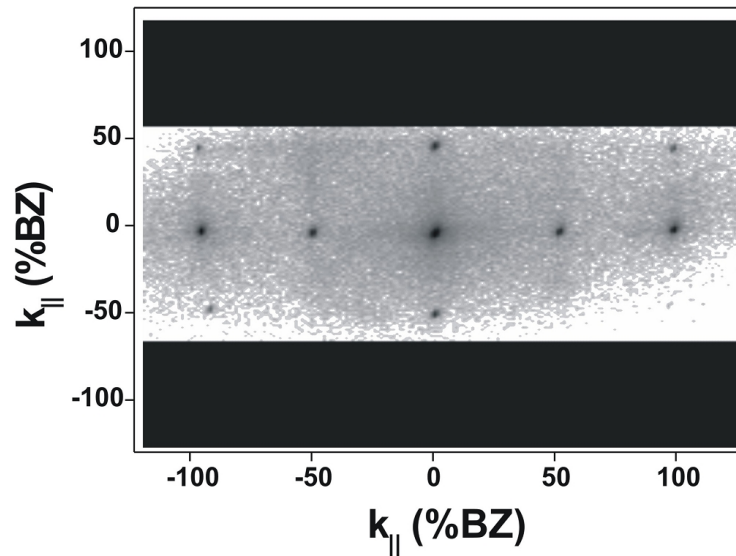


Figure 6.1: Two dimensional diffraction pattern of a clean flat Si(001) 2×1 reconstructed surface.

The Si(001)-substrate cleaning was performed as described in section 4.1.3. The surface reconstruction was revealed by a two dimensional LEED pattern as shown in Fig. 6.1. From the picture the two perpendicular domains on adjacent terraces with 2×1 and 1×2 , respectively can be seen. Diffuse streaks in the place of a $c(4 \times 2)$ -reconstruction

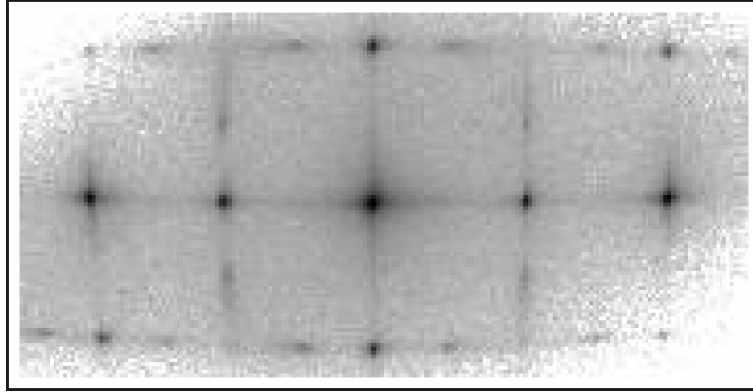


Figure 6.2: Two dimensional diffraction pattern of a clean flat Si(001) surface with $c(4 \times 2)$ reconstruction.

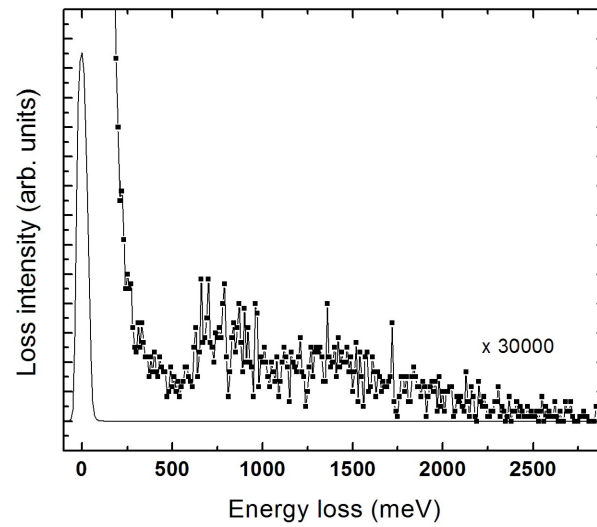


Figure 6.3: HREELS spectrum of a clean Si(001) surface with $c(4 \times 2)$ reconstruction. The primary energy is 51.6 eV and the FWHM is 60 meV.

can also be seen. A detailed description of the possible Si(001)-surface reconstructions has already been made in section 4.1.2. The occurrence of the $c(4\times 2)$ reconstruction was also obtained in the course of this work (Fig. 6.2) as expected at low temperature. It should be mention that all LEED pictures in this chapter have been taken with an asymmetry of 50 to 60% in one direction due to the device restrictions.

Contrary to the Si(111)- 7×7 reconstructed surface, the Si(001)-surface with 2×1 reconstruction is semiconducting [68]. Fig. 6.3 shows an electron energy loss spectrum taken on clean Si(001)- $c(4\times 2)$ surface. The resolution was decreased up to 60meV to increase the sensitivity. Two features emerge, around 800 meV and 1470 meV, in good agreement with available values in the literature [89, 90], especially in [91] where values of 900 and 1500meV were obtained. Both losses are of surface specific transitions, and are commonly denoted S_0 and S_1 respectively. S_1 is attributed to the electronic transition from the π bonding to π^* antibonding states associated with the asymmetric dimers [91, 92] whereas the feature S_0 can be assigned to indirect transition from the top of the valence band to the empty π^* antibonding states [93]. There is a diffuse shoulder with decreasing intensity from 300 up to 500meV. This feature might be associated with defects (e.g., dimer vacancy defects). In the near vicinity the CO stretching vibration would exist at 260meV. Thus a carbon contamination vibrational loss may be excluded [91].

6.1.2 Structure of DySi₂ on flat Si(001)

6.1.2.1 Morphology and reconstructions

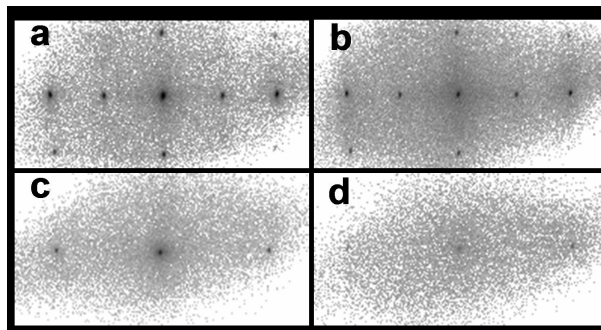


Figure 6.4: Two dimensional LEED pattern of a) clean Si(001)- 2×1 -surface on which in b), c) and d) 0.27ML, 0.82ML and 1.8ML Dy has been evaporated at RT, respectively.

Similarly to the case of Si(111), the silicide structure formed by deposition of Dy on Si(001) at RT is crystalline. This can be seen in Fig. 6.4. In (a) the 2×1 reconstruction of the clean Si(001)- 2×1 is shown. Successive deposition of Dy still produce a diffraction pattern. As illustrated in (b) for 0.27ML Dy-silicide, areas of clean Si(001)- 2×1

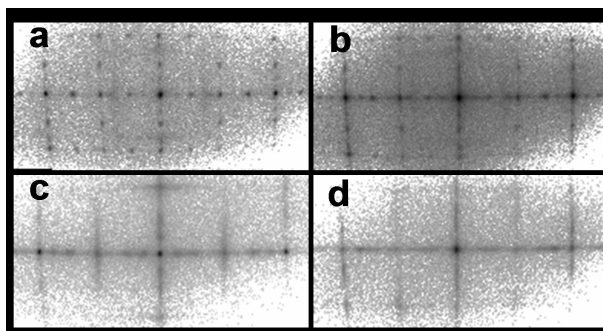


Figure 6.5: Two dimensional LEED pattern of a)0.27ML, b)0.35ML, c)0.82ML and d)1.8ML Dy evaporated at RT on Si(001)- 2×1 -surface, and annealed at 500°C for a,b and c, and at 550° for d.

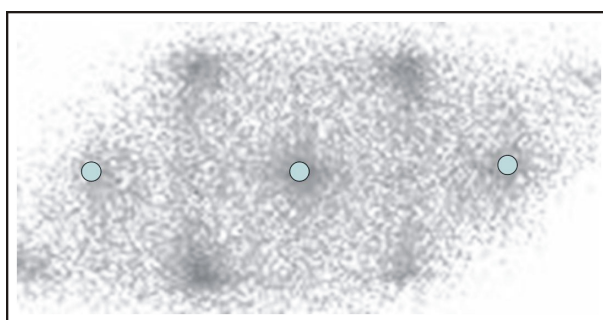


Figure 6.6: Two dimensional LEED pattern of 25ML Dy evaporated at RT on Si(001)- 2×1 -surface, and annealed at 600°C for 20min. The dark green circles represent the 1×1 -unit cell of Si(001)

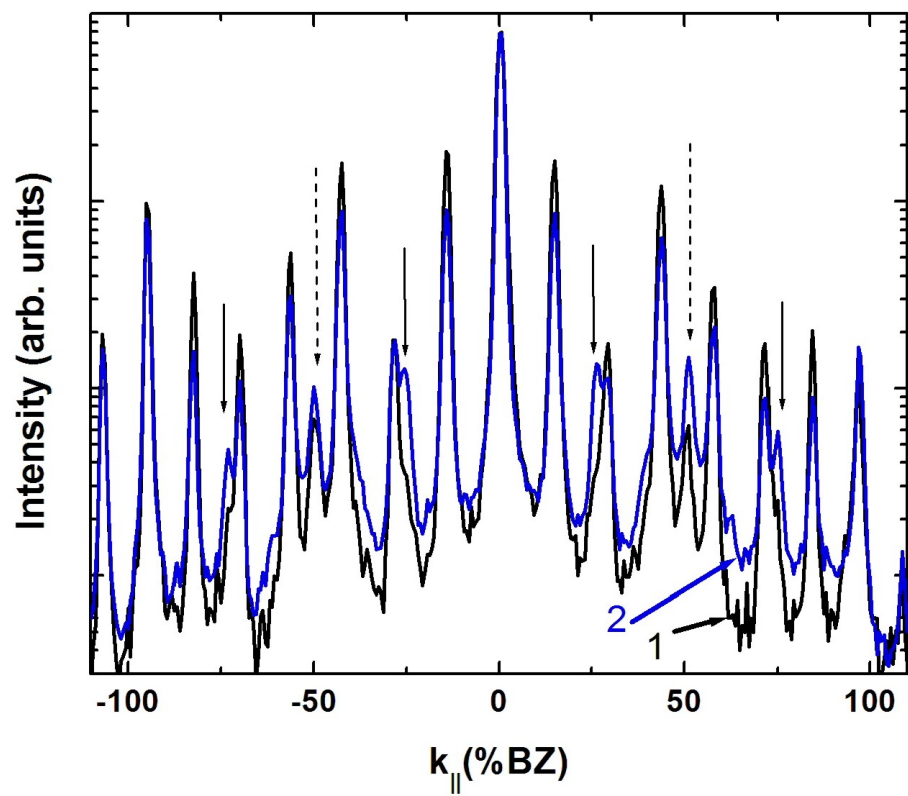


Figure 6.7: LEED line scans of 0.42ML Dy deposited on Si(001)- 2×1 -surface at 600°C (1), and further annealed at 600°C for 5min (2).

remain up to a Dy coverage of 0.5ML where the intensity of the $2\times$ -periodicity begins to vanish. This implies that the structure is getting more disordered with increasing Dy coverage.

The situation changes when the grown structure is annealed at high temperature around 500°C . Depending on the amount of Dy coverage specific reconstructions are formed. Fig. 6.5 shows LEED patterns of several Dy coverages, grown by depositing Dy at RT on Si(001) and annealing the sample at 500 and 550°C . Starting by picture (a) with 0.27ML Dy deposited, there is a combination of 4×2 and 2×4 reconstructions. If the structure on the flat Si(001) is kept in mind, where the direction of dimer rows is rotated by 90° on adjacent terraces (section 4.1.2), the 4×2 reconstruction can be understood as related on the direction of the dimer rows, rotated by 90° on the next terrace. In addition, a diffuse feature can be seen, with square form of $\approx 70\%$ BZ side length, centered around the specular spot. Its appearance seems to be restricted to coverages lower than 0.4ML. Especially that structure was found on samples when Dy was deposited at RT and annealed at temperature around 500°C .

At a slightly higher Dy coverage of 0.35ML (b in Fig. 6.5) the diffuse square is strongly reduced and new features are formed. Besides the formation of streaks and the 4×2 reconstruction, a 7×2 reconstruction has formed. Again, this reconstruction is available with a 90° -rotation.

For increasing coverages (c and d in Fig. DySi₂-at-RT-flat-Si001+Annealing), the 4×2 and 7×2 get diffuse, and sharp and broad streaks are appearing. Later on with further increase in Dy amount the streaks begin to reorganize into a $c(2\times 2)$ -reconstruction. Fig. 6.6 shows a LEED pattern of 25ML Dy deposited at RT and annealed for 20min at 600°C . The $c(2\times 2)$ -reconstruction can be recognized and the diffuse intensity can be referred to the high roughness on the surface.

The growth of Dy silicide on flat Si(001) seems to be the same in the range from 450 to 600°C . An interesting annealing effect was observed during the annealing process when the substrate was held at high temperature during deposition. Fig. 6.7 shows LEED line scans of 0.42ML Dy grown on Si(001) held at 600°C . The sample heating was first stopped just after finishing the deposition (1) and later again annealed at the same temperature for 5min (2). After the 5min annealing time, the intensity of the $7\times$ -spots has decreased. Furthermore a $4\times$ -periodicity which was before appearing as a broad shoulder has become a clear peak. The same process conducted at 500°C results in further increase of intensity of the spots.

6.1.2.2 Electronic structure

Fig. 6.8 shows a comparison between HREELS spectra taken at Γ -point for a clean Si(001)- 2×1 surface and after growth of Dy silicide.

For the Dy silicide covered sample the HREELS spectrum presents a broad Drude tail. This is an indicator of a metallic nature of the surface. The growth of Dy silicide is accompanied by a broadening of the elastic peak. The lack of such a tail in case of Si(001) is in good agreement with the semiconducting nature of the 2×1 -surface.

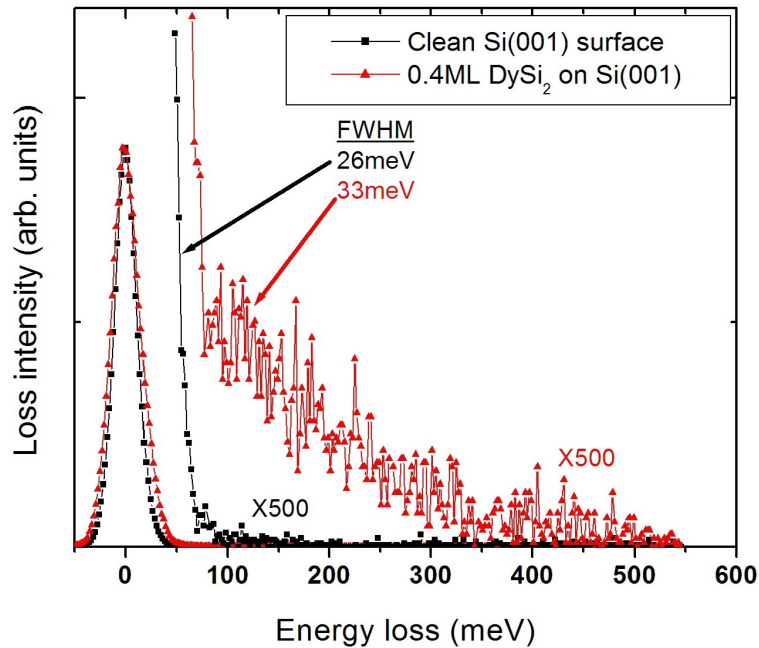


Figure 6.8: HREELS spectra taken at 120K, $E_p=51.6\text{eV}$. The curves have been magnified by 500 for clarity

There is then a high expectation to find plasmon-like excitation on Dy silicide grown on Si(001).

Fig. 6.9 shows HREELS spectra of Dy silicide grown by depositing 0.37ML Dy on Si(001) held at 500°C . A loss peak is clearly seen at $q_{\parallel} > 0.016 \text{ \AA}$. The loss peak disperses to higher energy and begins to broaden, until it vanishes for $q_{\parallel} > 0.1 \text{ \AA}$. Astonishingly the occurrence of the losses seems to be restricted to a narrow range of Dy coverages, around 0.35ML. That coverage is associated with the formation of the 7×2 reconstructions.

It has already been reported that it is possible to induce an anisotropy in the terrace distribution on the Si(001) surface by heating the substrate. Depending to the current direction, if the substrate is held at temperatures higher than 900°C for a sufficiently long time, one of the dimer row directions, parallel or perpendicular to the steps, will be favored [94]. Growth of 0.35ML Dy silicide on such surface results in anisotropical 7×2 reconstruction where the intensity in one of the two directions is vanishing, as illustrated in the upper part of Fig. 6.10. The lower part shows energy loss spectra taken with momentum transfers 0.057 \AA (graph a) and 0.08 \AA (graph b). In each graph, energy loss spectra along and perpendicular to the $7 \times$ periodicity are represented by full and empty squares, respectively.

The energy loss spectra present a directional anisotropy, which, if associated to the anisotropy of the grown Dy silicide, can reveal surface structures with high aspect

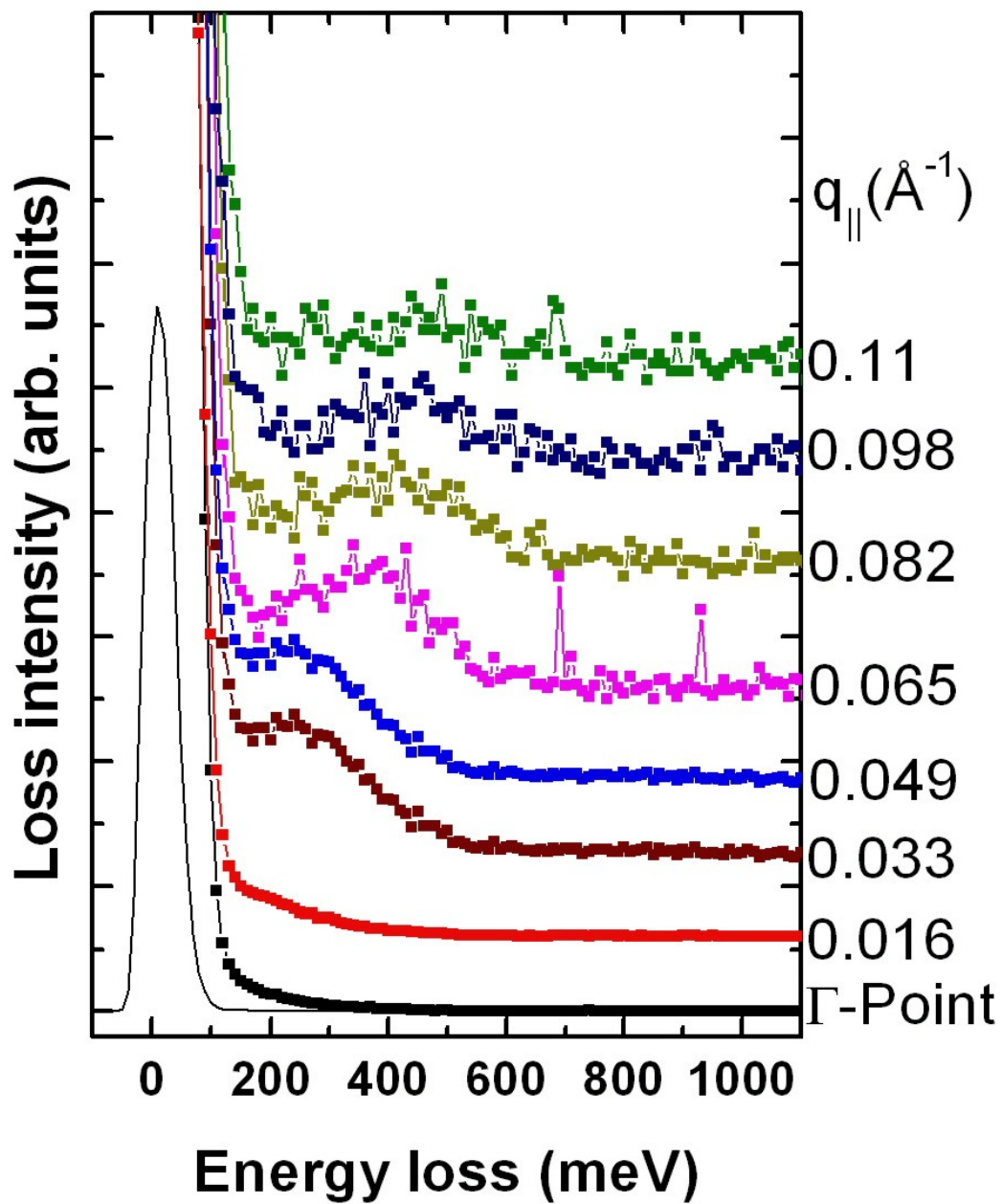


Figure 6.9: HREELS spectra taken at 120K on 0.37ML Dy silicide grown on Si(001), $E_p=51.6\text{eV}$

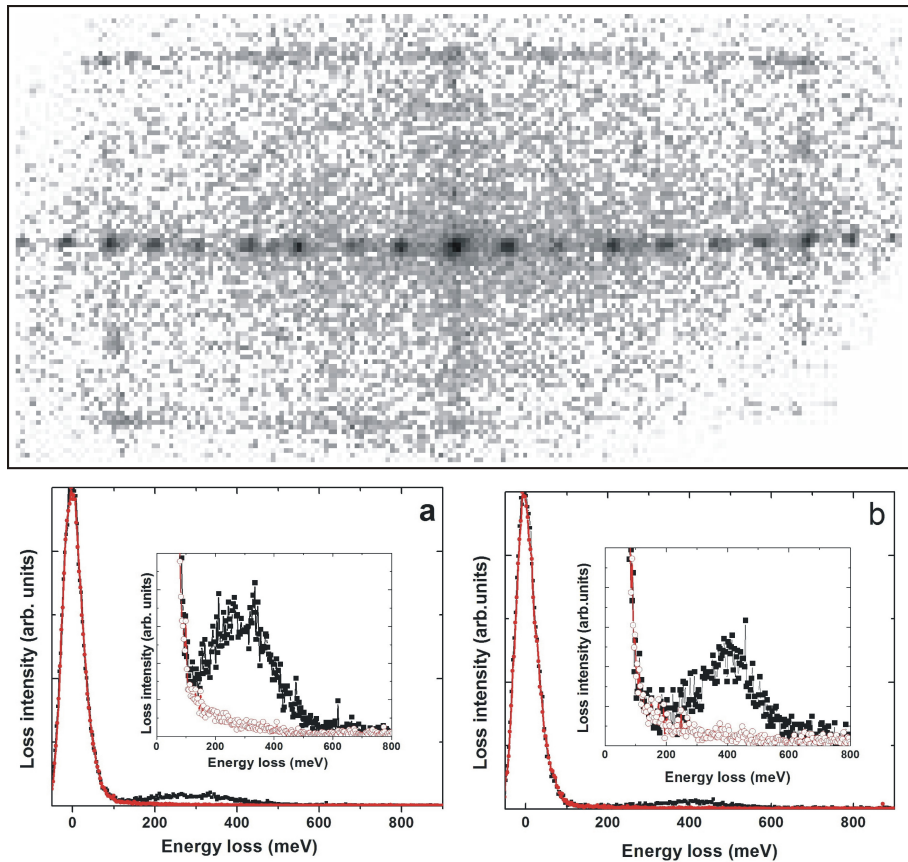


Figure 6.10: upper: two dimensional LEED pattern of Dy silicide grown by depositing 0.37ML Dy on anisotropic Si(001). lower: (a) and (b) are HREELS spectra of the silicide structure at 0.057 and 0.08 Å respectively. In each graph, the full squares (empty circles) represent spectra perpendicular (parallel) to the sharp $7\times$ -spots line. $E_p=51.6\text{eV}$

ratios, resembling to elongated islands, or wire structures.

6.1.3 Discussion

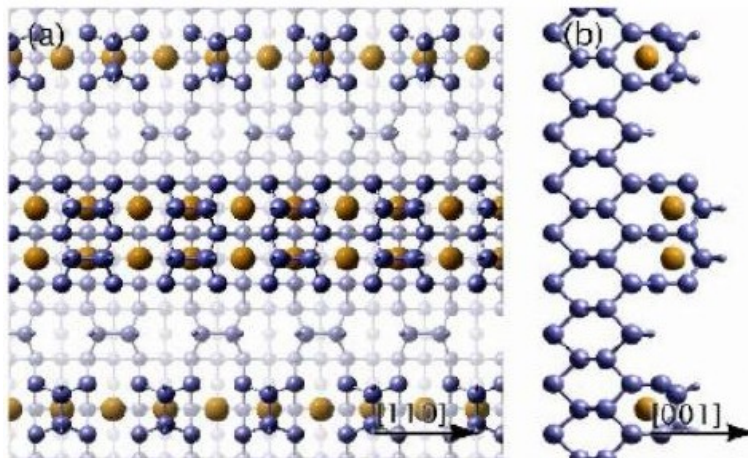


Figure 6.11: Structure model of the 2×7 reconstruction [99].

Contrary to Er which was found to be amorphous when deposited on Si(001) at RT [95], we found that RT deposited Dy up to a coverage of 1.8ML still produce a diffraction pattern. It has not been cleared whether the disappearance of the $2 \times$ -periodicity was due to increasing disorder in the film or a $2 \times 1 - 1 \times 1$ phase transition. The assumption of the crystallinity of the RT evaporated Dy film has not yet been reported so far in literature. But in both cases, high quality silicide films can be achieved by annealing the sample at high temperature. The good ordering of the overlayer becomes clear by the various reconstructions.

Dy silicide grown on Si(111) results in a closed film. In contrast, thick Dy layer growth on Si(001) results in 3D rectangular islands [19]. Consequently the diffraction pattern may become very diffuse, but still shows the top surface reconstruction of the islands. Only by growing submonolayer Dy coverages it was possible to observe of structures with high length to width aspect ratios, the so-called nanowires [19].

It is energetically favorable to form silicide nanowires by reaction between Si atoms on the Si(001) and deposited Dy adatoms. But this reaction must break the Si-Si-bond at the substrate surface. Higher annealing temperatures are needed to ensure the reaction but result in dislocations in the nanowires to relieve the lattice mismatch [96]. The compromise to form good quality nanowires resides in a relatively narrow temperature range of 500-600°C and the steps are the source of atoms for the reaction, because of the lower number of Si-Si bonds [97]. For this reason the growth of nanowires is not stopped by steps but only by reaching another nanowires.

The reconstructions and streak features encountered above are in good agreement with

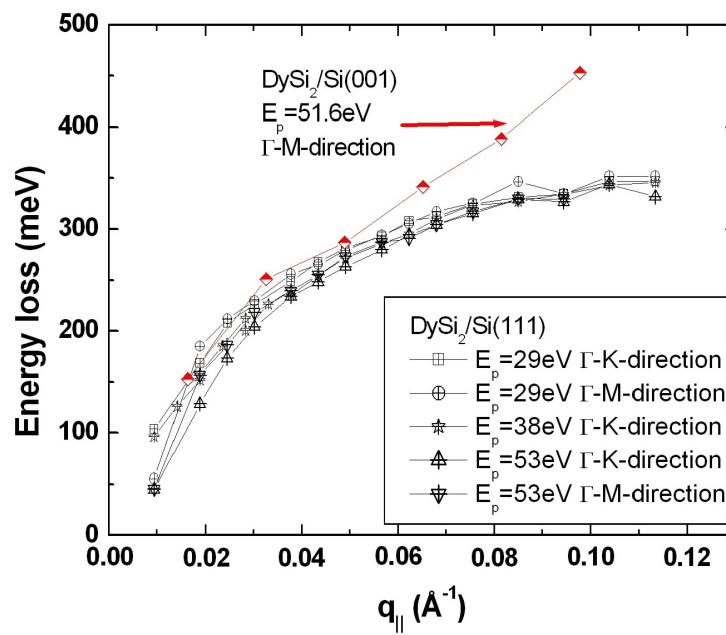


Figure 6.12: The 2D-plasmon dispersion curves of 1ML Dy disilicide grown on Si(111) are compared to the plasmon dispersion curve obtained in a array of parallel wires crossing each other orthogonally.

both LEED and STM measurements that have been made on Dy silicide grown on Si(001) [20, 80, 96, 98]. When Dy silicide is grown at temperature around 600°C and higher, STM pictures showed thick wire structures between which areas of clean 2×1-Si(001) coexist with areas of 2×4 and 2×7 reconstructions. Areas of 2×1 can mix with 2×4 reconstructions but not with 2×7 [80]. Deposition of Dy at RT followed by annealing at 500°C results in close-packed thin Dy silicide nanowires of 2×7 reconstruction [99]. The 2×-periodicities are parallel to the 2×-periodicity of the clean Si(001) [100]. This means that the nanowires are growing perpendicularly to the dimer row direction.

The nanowire must have, additionally to its wire-like shape, metallic character. STS measurement has confirmed such metallicity in the Ho-silicide nanowires grown on Si(001) [20]. In good agreement, our HREELS measurement at Γ -point shows a Drude tail far higher than on clean Si, demonstrating the metallic nature of the surface. Surprisingly energy loss dispersion was only obtained in relation with the 2×7 reconstruction. It may be related to the good ordering that can be achieved when Dy silicide nanowires are grown at 500°C [99]. A structure model for the 2×7 reconstruction, shown in Fig. 6.11, was proposed on the basis of STM measurements [99].

The plasmon energy dispersion extracted from the HREELS spectra in Fig. 6.9 is compared to the plasmon dispersion on the monolayer DySi₂ film (Fig. 5.10), as illustrated in Fig. 6.12. In the very vicinity of Γ -point all plasmon dispersion curves tend to vanish as it should be expected for 2D and 1D plasmon losses. Interesting is the difference in the behavior as q_{\parallel} increases. The discrepancy in the two dispersion relations reveals the differences in the structures formed on the two substrates. On Si(111) the Dy-silicide films form closed 2D layers of hexagonal AIB₂ structures, whereas the Dy-silicides grown on Si(001) build 1D-like structures of tetragonal symmetry.

The 1D-structure is further supported by the anisotropy in the HREELS measurements on the Si(001) substrate with a majority of one terrace kind. Since the 7×-periodicity is perpendicular to the nanowire direction, the graphs in the lower part of Fig. 6.10 can now be better understood. The losses have only been obtained in the direction parallel to the nanowires. In the perpendicular direction the HREELS spectra remain with a broad shoulder that could not be resolved.

For a better control of the direction in which the Dy silicide nanowires grow, it is of importance to control the terrace distribution on Si(001). Since the nanowires are not stopped by steps the chosen surface must have dimer rows perpendicular to the steps. The laborious work for the heating induced anisotropy can be simplified by the use of vicinal surfaces. This particular surface can be for example Si(001) with a 4° miscut towards Si[1 $\bar{1}$ 0], which results in double atomic steps with a terrace width of 39 Å \approx 10 a_{Si} , where a_{Si} =3.84 Å, corresponding to the 1×1 unit-cell dimension on Si(001) surface. The study of the Dy silicide nanowires on vicinal Si(001) will be the object of the following section.

6.2 Dysprosium silicide on vicinal Si(001)

6.2.1 Structure of vicinal Si(001) substrate

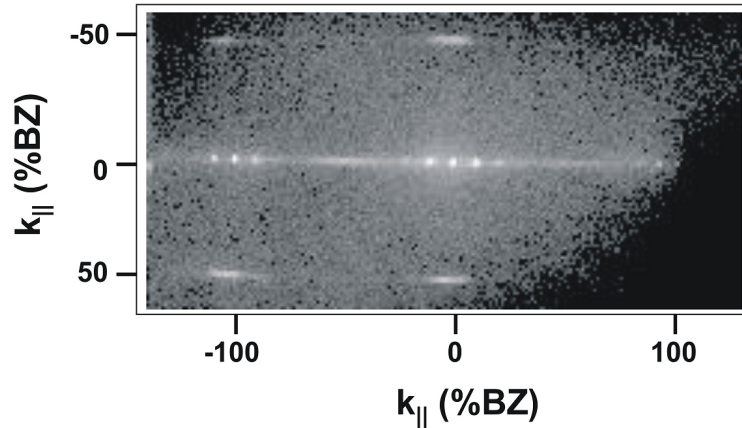


Figure 6.13: Two dimensional diffraction pattern of a clean vicinal Si(001) surface reconstruction.

Fig. 6.13 represents a two dimensional LEED pattern of a 4° miscut Si(001). Striking differences to the case of the flat Si(001)-surface (fig. 6.1) can be seen. On the one hand all main reflexes are split. This results from a regular step arrangement which gives an additional periodicity to the reconstruction on terraces. From the 10% splitting a mean terrace width of 10 lattice spacings can be deduced. On the other hand one domain with 2×1 reconstruction is nearly missing. In an ideal case it should vanish completely due to the existence of double atomic steps. But during the sample preparation defects are created, as the steps are destroyed in some places and very narrow terraces with monoatomic steps appear with the 1×2 reconstruction.

6.2.2 Investigation of DySi₂ on vicinal Si(001)

The experience gathered by growing Dy silicide nanowires on flat Si(001) was used in the present study. The Dy atoms were deposited either at RT or at 500°C followed by annealing at 500°C . The remaining question was to find an optimal coverage at which the metallicity could be found by means of electron energy loss spectroscopy.

Fig. 6.14 shows several HREELS spectra taken at different Dy silicide coverages at a momentum transfer of $q_{||} = 0.065 \text{ \AA}^{-1}$. The Dy silicide structure was grown by successive deposition of 0.1 ML on vicinal Si(001). Each deposited Dy layer was then annealed for 1 min at 500°C . The elastic peak intensity of all HREELS spectra have been normalised for comparison. HREELS spectrum of 0.2ML Dy silicide presents a broad loss peak that begins to emerge from the background signal. Its intensity

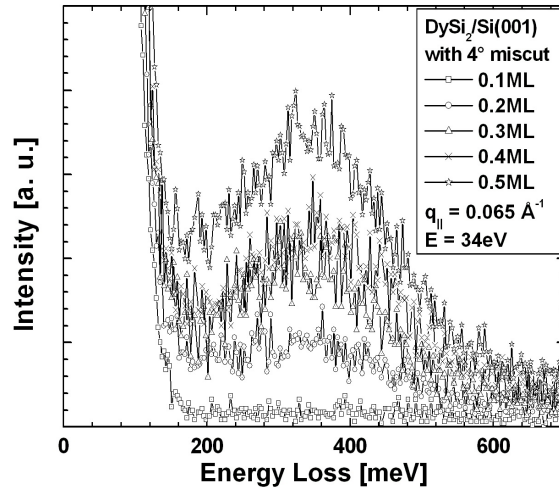


Figure 6.14: HREELS spectra performed at $q_{\parallel} = 0.065 \text{ \AA}^{-1}$ for increasing coverage.

increases with increasing coverage. Around 0.4 ML the intensity in the loss peak increases very slightly. There seems to be a saturation, which is however clearly not confirmed by the increase in intensity with 0.5 ML Dy silicide. At the same time the elastic peak is broadening with increasing coverage. If the difference in the FWHM of the elastic peak between two consecutive Dy silicide coverages is considered, it is found to be positive and nearly double at each deposition step until reaching 0.4 ML. At 0.5 ML Dy silicide, the broadening difference decreases by a factor of ≈ 4 compared to the previous deposition step. If the Dy silicide is grown at RT and then annealed at 500°C for several minutes, the same characteristics are reproduced, except that the loss intensity saturates at Dy silicide coverage of 0.4 ML. In the following results of the investigations of Dy silicide nanowires grown by depositing 0.4 ML Dy at 500°C on vicinal Si(001) will be given.

6.2.2.1 Study of the morphology of Dy silicide nanowires

Fig. 6.15 represents a two dimensional LEED pattern obtained after growing 0.4 ML Dy silicide on the substrate given in Fig. 6.13.

At first sight the LEED spots are all aligned in one direction, described as the one perpendicular to the step direction. The picture represents clearly a diffraction pattern of a one dimensional structure. A closer look first in the direction parallel to the step direction is given in Fig. 6.16. Besides the half order spots seen on the two dimensional diffraction pattern (Fig. 6.15), low intensity $4\times$ -periodicities are observed. They do

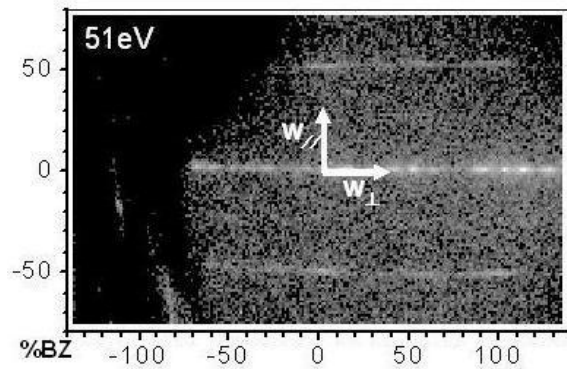


Figure 6.15: Two-dimensional LEED pattern of 0.4 ML Dy silicide grown on Si(001) with 4° miscut towards Si[$1\bar{1}0$]. The arrows with w_{\parallel} and w_{\perp} represent directions parallel and perpendicular to the step, respectively. $E_p=51\text{eV}$

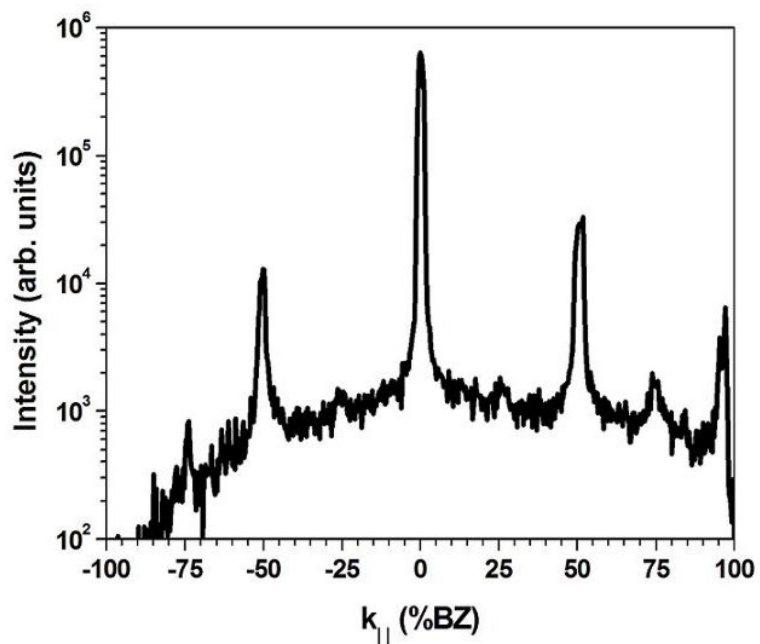


Figure 6.16: LEED line scan along the direction parallel to the step shown by the arrow w_{\parallel}

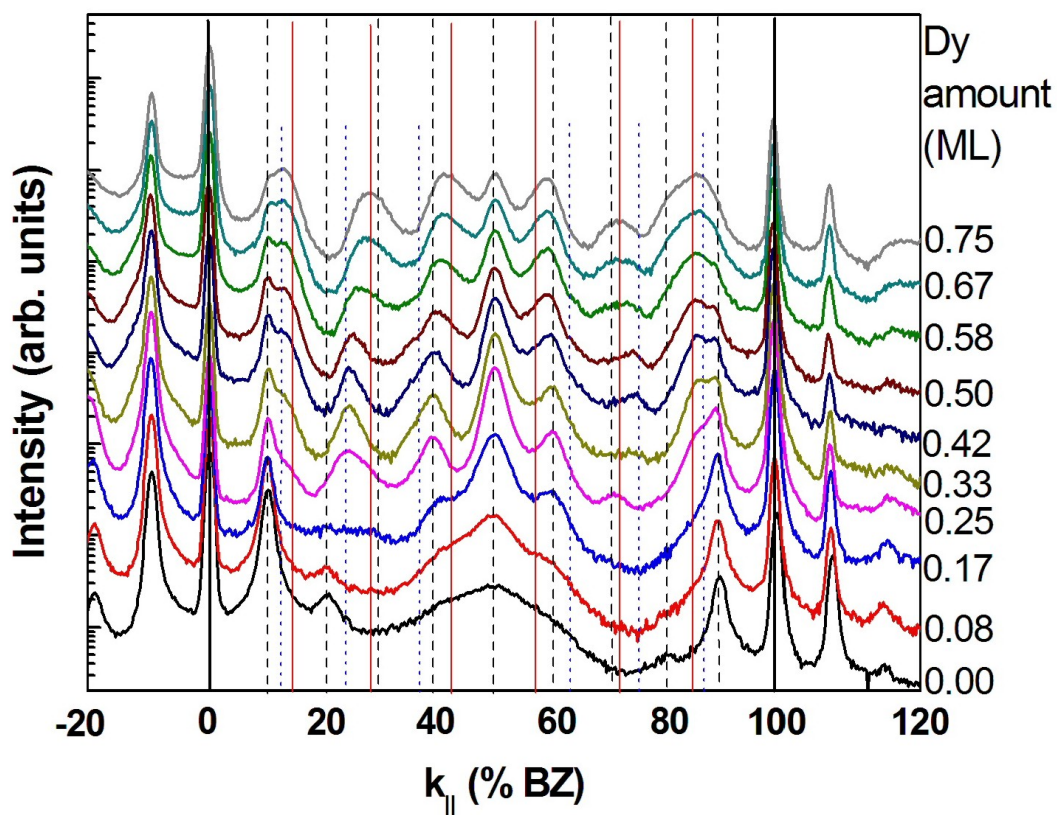


Figure 6.17: LEED line scans of a successively grown Dy silicide structure on vicinal Si(001) by adding at each deposition step 0.08ML of Dy at 500°C and additionally annealing for 1 min at the same temperature. The line scans are performed in the direction perpendicular the step direction. Dashed black lines, solid red lines and blue dotted lines represent $10\times$, $7\times$ and $8\times$ periodicities peak positions, respectively.

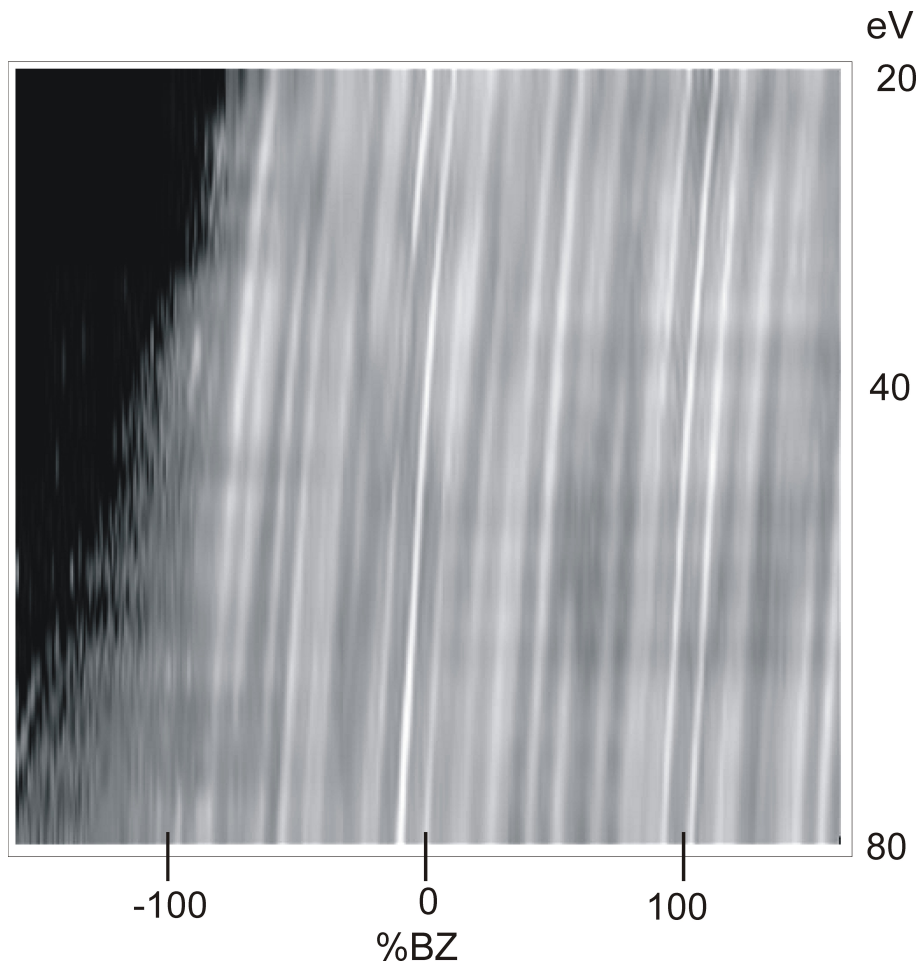


Figure 6.18: Plot of the reciprocal space as function of vertical scattering vector K_{\perp} or scattering phase S . The Dy silicide has been prepared by deposition of 0.4 ML Dy on Si(001)-4° miscut at 500°C

appear with every formation of Dy silicide structure.

The situation is more complicated when considering the line scans along the direction normal to the step direction. Besides the $10\times$ -periodicity recurrent to the terrace width on the 4° -miscut vicinal Si(001)-surface, additional spots are observed with a periodicity close to a $7\times$ -periodicity.

To get a closer look, a Dy silicide structure was prepared by depositing successively $\approx 0.08\text{ML}$ Dy on the vicinal surface heated at 500°C . At the end of each deposition step, the sample was annealed at the same temperature for 1 min.

Fig. 6.17 shows LEED line scans performed along the direction perpendicular to the step direction after each step of a successive deposition process of Dy on vicinal Si(001) held at 500°C and then annealed at the same temperature for 1 min. The line scans are arranged vertically in the order they were made, the lowest line scan has been performed on the lowest Dy silicide coverage. Dashed black, solid red and blue dotted lines represent peak positions with $10\times$, $7\times$ and $8\times$ periodicities. They help for comparison.

The line scans up to a Dy silicide coverage of 0.17 ML are nearly identical, apart from some broad peaks around 40 and 60 %BZ. Those broad features can be also seen around 25 %BZ where the peak at 20 %BZ has vanished. The new features seem to come from a $10\times$ -periodicity. This is even clearly enhanced by the next deposition step. Additional peaks that present other periodicities can also be seen. The peak at 10 %BZ has got a shoulder on the right side whereas the peak at 90 %BZ has got a shoulder at the left side. This means that the grown structure is inducing a new $n\times$ -periodicity, with n lower than 10. If both shoulders are considered, with increasing coverage they increase in intensity so that between 0.50 and 0.67 ML they become more intense than the neighboring peaks. Besides the change in intensity, a position shift is observed and seems to be located between the position of the first and last pair of solid red and blue dotted lines, shifting from the blue dotted line to the red solid line. This corresponds to n between 7 and 8.

At 0.25 ML a peak can be observed at ≈ 25 %BZ. With increasing coverage peaks at ≈ 75 %BZ are seen and they experience a shift with increasing coverage towards the neighboring solid red lines. It may be easier to assume that those peaks belong to a $4\times$ -periodicity. But considering the similarity in the peak position shift towards the $7\times$ -peak positions, it is more consequent to relate them to the shoulders observed around 10 and 90 %BZ, and so to build a $8\times$ -periodicity. The rest of the peaks are assumed to be hidden by the diffuse shoulders that can be observed at the corresponding positions.

It is interesting to observe the intensity behavior of the peak at 50 %BZ. Initially very diffuse on the clean sample due to probable defects at steps, the peak is sharper around 0.33 ML. The line scan at that coverage has predominantly peaks that has now been identified as belonging to the $8\times$ - and $10\times$ -periodicities. These contribute in common to the intensity of the mentioned peak. Its intensity begins to decrease, together with the increase in intensity of the peaks at 40 and 60 %BZ while they are shifting towards the next neighboring positions of $7\times$ -periodicity. The structure seems to reorganise

continuously towards that periodicity with increasing coverage.

From Fig. 6.17 it can be seen that the Dy silicide structure grown by depositing 0.4 ML Dy is made of a mixture of periodicities. This behavior implies that the surface might have built facets during the silicide formation through Si-Dy reactions. It has been found that at temperatures around 500°C the steps are the favored sources of Si atoms. In order to keep the macroscopic surface orientation of 4° some terraces must become broader whereas the other get narrower with different inclination for the two kind of terraces. Another possibility might be the building of a saw-tooth-like structure. One way of checking the formation of facets by means of LEED is to perform several line scans with different energies. The change in the terrace orientation results in Bragg diffraction rods of different inclination.

Fig. 6.18 has been obtained by putting together successive line scans of different energy from 20 to 85eV with an energy step of 0.5eV. The picture represents the intensity behavior in a grey scale. The main order spots reproduce the structure on the clean 4° miscut Si(001). They have a splitting of 10%BZ and the inclination is similar, which may lead to the same terrace distribution with the double atomic step height. All the diffraction rods are running parallel to each other and they might become broad with change in the scattering phase. No faceting is observed, contrary to what was expected.

6.2.2.2 Electronic structure

After the morphological characterization of the Dy silicide structure, HREELS has been applied to study the surface electronic structure. Fig. 6.19 shows a series of HREELS spectra taken parallel to the step direction for the 0.4 ML Dy silicide grown at 500°C on the 4° miscut Si(001). The spectrum at the Γ -point presents a broad shoulder of Drude nature similar to the case with flat Si(001) surface. At $q_{||} = 0.033 \text{ \AA}^{-1}$ a broad peak appears and narrows with increasing momentum transfer while its intensity is increasing. The peak disperses to high energy with increasing momentum transfer. At $q_{||} > 0.065 \text{ \AA}^{-1}$ the loss peak begins to broaden again while its intensity decreases. After $q_{||} = 0.13 \text{ \AA}^{-1}$ the loss peak is hard to distinguish from the background. HREELS spectra made normal to the step direction are shown in Fig. 6.20. Besides the broad Drude tail that is observed in all spectra no other loss peak is found.

The nature of the losses has been checked by performing an angle distribution of the inelastic scattering as shown in Fig. 6.21. The curve reproduces the form of a dipole lobe, in good agreement with the dipole theory. The intensity of the inelastically scattered electrons that have a dipole scattering is concentrated in a lobe located near the specular direction.

6.3 Discussion

The Si(001) with a 4° surface miscut towards Si[1 $\bar{1}$ 0] have stabilized double atomic steps. The terraces have dimer rows running perpendicular to the steps. Due to the

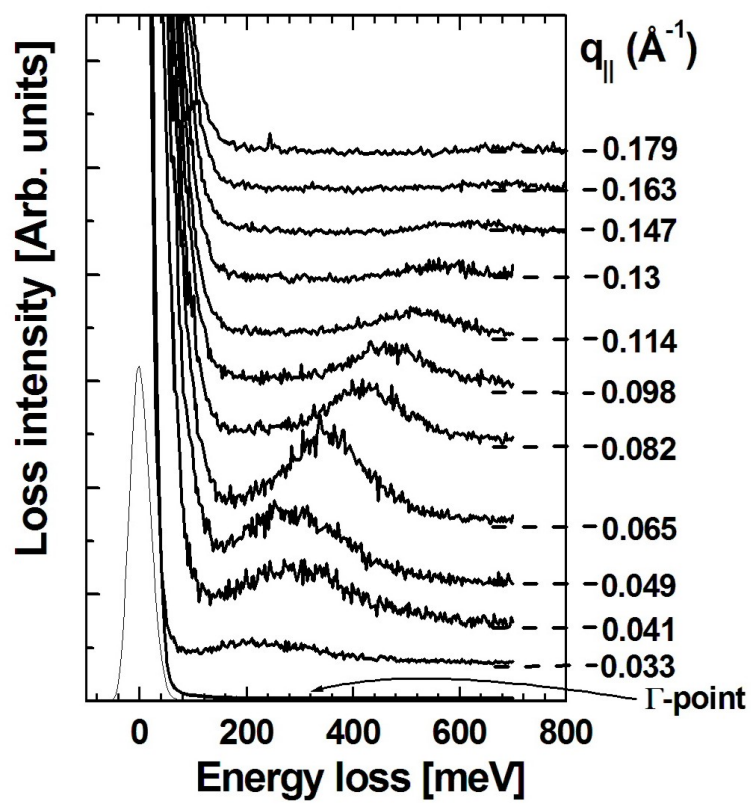


Figure 6.19: HREELS spectra performed in the direction parallel to the step direction for 0.4 ML Dy silicide grown on Si(001)-4° at 500°C

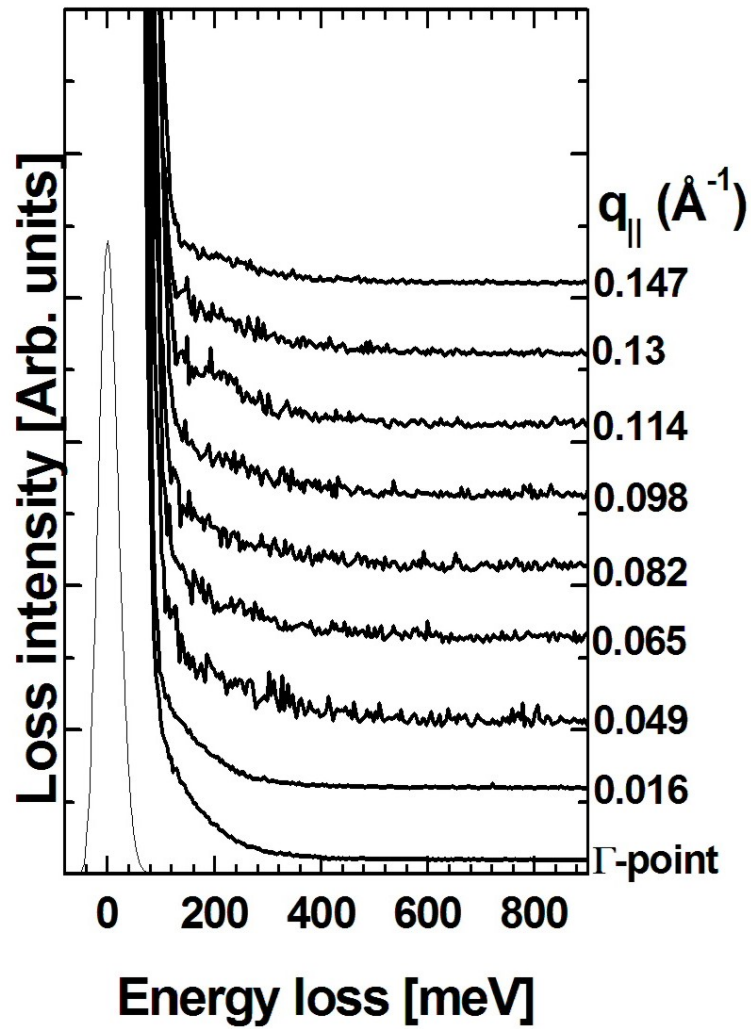


Figure 6.20: HREELS spectra performed in the direction normal to the step direction for 0.4 ML Dy silicide grown on Si(001)-4° at 500°C

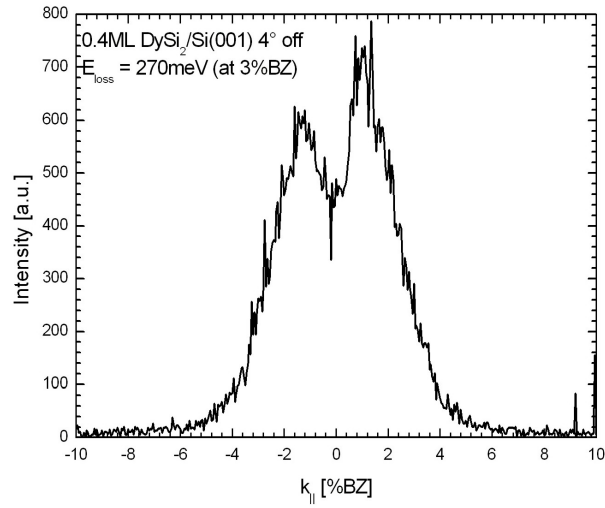


Figure 6.21: Angular distribution of the inelastic scattering with $\Delta E = 270$ meV for the 0.4ML Dy silicide structure.

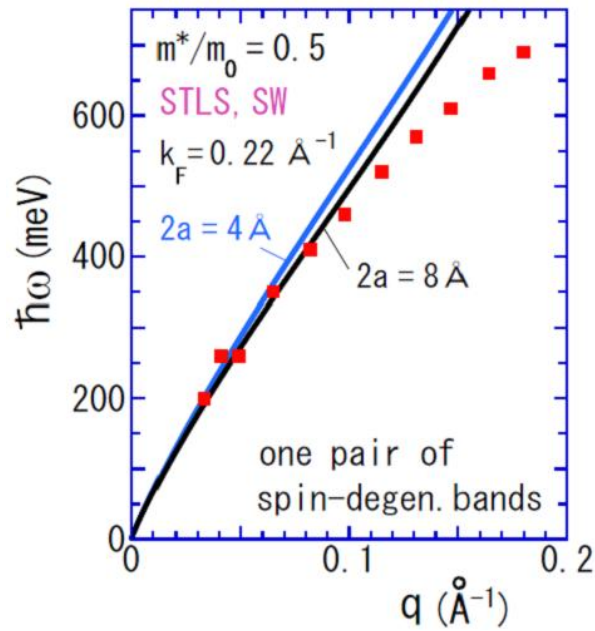


Figure 6.22: 1D-plasmon model fitting of the experimental dispersion curve. m^* is the effective electron mass, k_F the Fermi wave vector, and $2a$ the wire width. STLS stands for Singwi, Tosi, Land, and Sjölander. the abbreviation represents in general the self-consistent local field correction theory for 3D electronic excitations developed by those authors. See [103] for details.

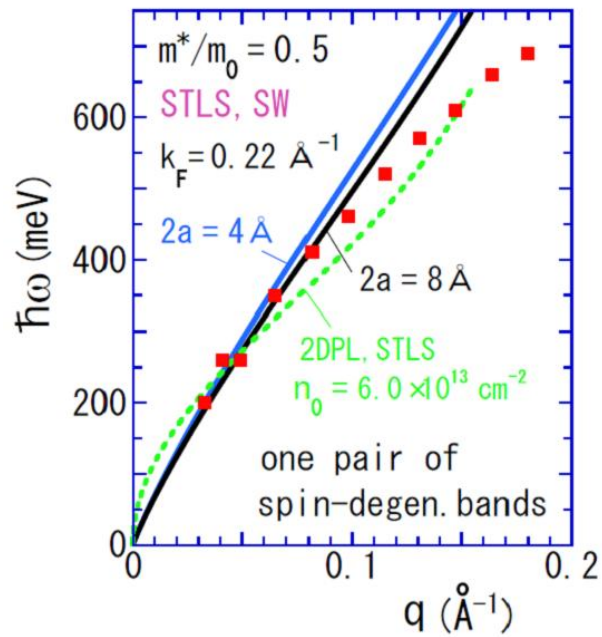


Figure 6.23: The fit model is performed using a 2D-plasmon model, shown together with a 1D fit model

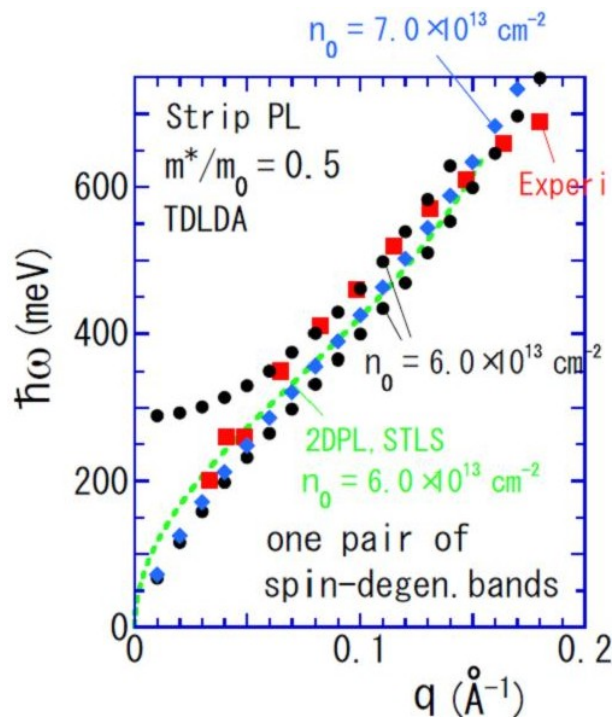


Figure 6.24: The fitting calculation assume that the nanowires form strips of 40 Å wide

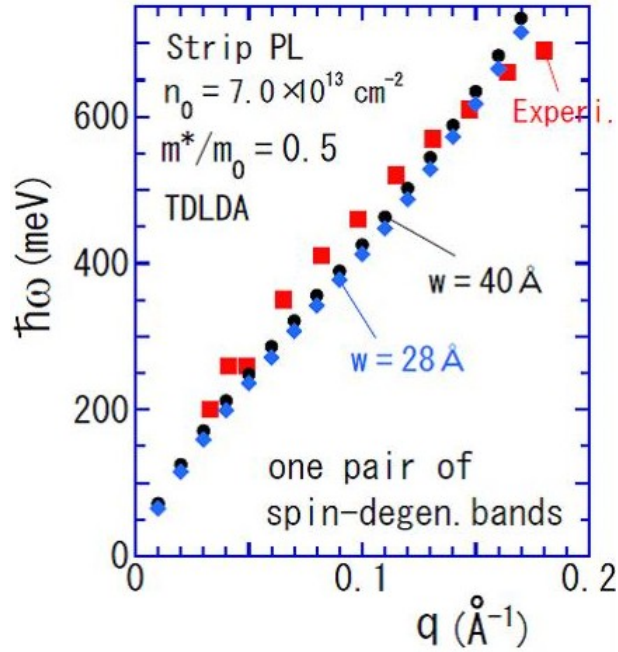


Figure 6.25: The symmetric plasmon branch is kept for further fitting. The wire width is taken as parameter

fact that the Dy silicide nanowires grow perpendicular to the dimer rows [100], the formation of Dy silicide on Si(001) with 4° miscut leads to the formation of arrays of one dimensional structures or nanowires which are far longer than those prepared on flat Si(001) [22, 101, 102]. Additionally the nanowire formation induces surface reconstructions of $n \times 2$ and $n \times 4$, in good agreement with results available in the literature [22]. The $2 \times$ and $4 \times$ -superperiodicities appear in the direction parallel to the step. We found that in the submonolayer regime n takes values from 7 to 10 depending on coverage. It is not excluded that structures with different values of n coexist on the surface.

The mixing of structure of different periodicity could not be explained by faceting as expected and another structure model needs to be considered. Nevertheless the mixing of structure seems to be optimal at 0.4ML Dy silicide for an enhanced signal in the HREELS study. Parallel to the nanowires, at $q_{\parallel} < 0.033 \text{ \AA}^{-1}$, it was not possible to separate the peak from the Drude tail. But for larger momentum transfer, a loss peak is observed that disperses to higher energies before it broadens and disappears in the background signal. In the direction normal to the nanowires no losses were obtained. This means that the one dimensional arrangement of the nanowires is able to support a one dimensional electronic structure. This is in good agreement with photoemission study on this system [22].

The losses in the direction parallel to the nanowires were clearly found to be of dipolar

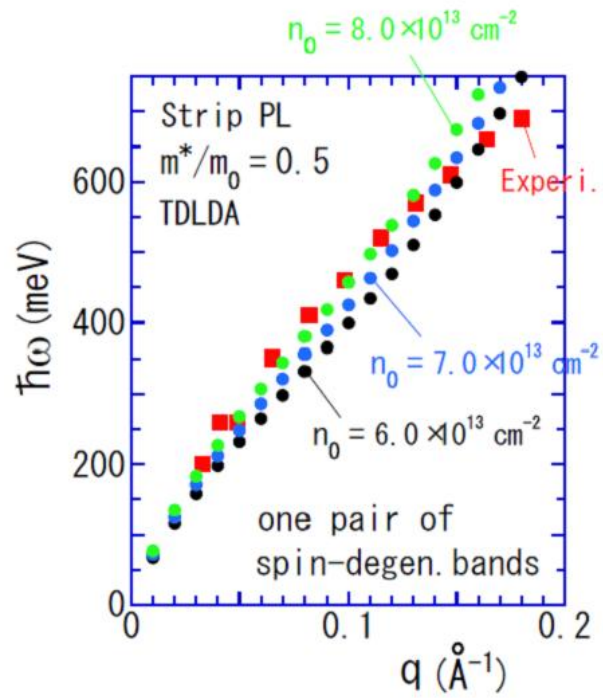


Figure 6.26: Fit dependence on the 2D electron density

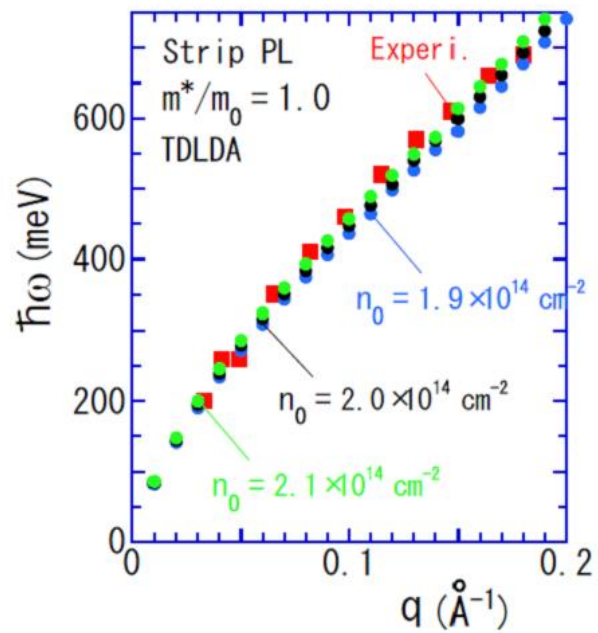


Figure 6.27: Fit dependence on the electron effective mass

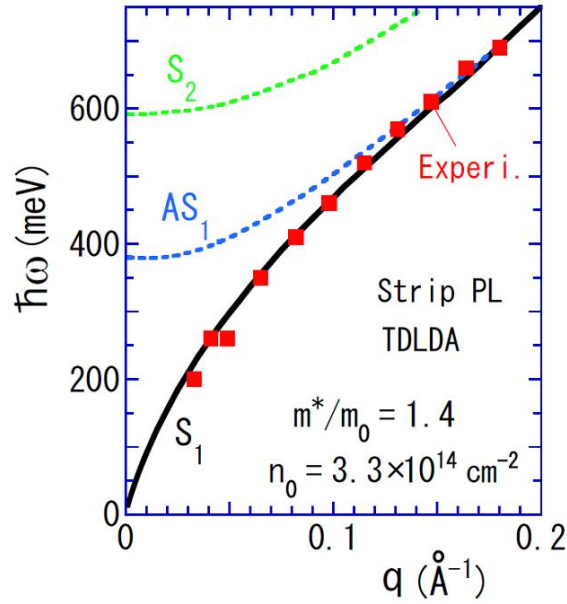


Figure 6.28: Strip monolayer with higher mode. Symmetric mode S1, asymmetric mode AS1 and a higher symmetric mode S2

nature. This brings us to the conclusion that the Dy silicide nanowires are sustaining a one dimensional electron collective excitation, or 1D-plasmon. The parameters of those plasmons losses in terms of electron effective mass and electron density can be found by fitting the energy dispersion of the peak position obtained from Fig. 6.19. The dispersion curve was first fitted using a 1D-plasmon model. As it can be seen in Fig. 6.22 the 1D-plasmon model gives only very straight dispersion curve. The fit matches well the experimental data at small q value but fails completely to reproduce the curvature of the experimental dispersion curve. The increase in the wire width did not change significantly the slope of the fit model. Since the experimental dispersion curve bends towards lower energy with respect to the 1D-plasmon energy model, a 2D-plasmon fit model was tried (Fig. 6.23). The experimental dispersion curve is again only better fitted in the lower q values where it shows slightly a \sqrt{q} behavior. At higher q values the fit model deviates. Our measured plasmon energy dispersion show very little \sqrt{q} dependence and its frequency is clearly higher than the calculated one. The electron system in the Dy-silicide nanowires seems to be localized in a space region larger than a simple atomic wide nanowire. We introduce the notion of strip region, meaning a nanowire with a finite width, allowing some degree of lateral correlations in the electron system. Following [26] low dimensional plasmons in a strip region have a series of plasmon dispersion branches where the node number in oscillation of the induced electron density δn across the strip increases one by one with ascending energy. The induced electron-density distribution δn of each mode with even node number is

symmetric with respect to the center line in the strip region. In the other case, it is asymmetric.

We assume for as starting point a wire width of 40 Å, what means that the wire is assumed to cover the whole terrace on the vicinal Si(001) surface. The other parameters used in the previous fit are kept constant (Fig. 6.24). We have two modes, the upper one is antisymmetric mode and the lower one is symmetric. The latter is the mode that is more HREELS active. We concentrated first on the symmetric mode. We can see that the fitting model is strongly improved. Three parameters can be used here: the electron effective mass m^* , the electron density n_0 and the wire width.

Increasing n_0 brings the fitting curve closer to the experimental one. The expected dependence on the strip width did not occur. In fact the slope of the fitting curve is not really changed if the width is varied from 28 Å to 40 Å (Fig. 6.25). The width was then left constant at 40 Å. As seen before, the fitting curve remained very sensitive to the effective mass.

A gradually increase from $n_0=6 \times 10^{12} \text{ cm}^{-2}$ to $n_0=8 \times 10^{12} \text{ cm}^{-2}$ shifted significantly the fitting curve towards the experimental curve. Some deviation are still present at smaller and larger q (Fig. 6.26). Further, the effective electron mass is increased from $0.5m_0$ to $1m_0$. The fitting curve responded in getting closer. The electron density is also further increased. It can be seen in Fig. 6.27 that the fitting curve with $m^*=1m_0$ and $n_0=2.1 \times 10^{14} \text{ cm}^{-2}$ fits better the experimental data.

The experimental dispersion curve was at the end perfectly fitted by assuming an effective electron mass of $1.4m_0$ and a 2D electron density of $3.3 \times 10^{14} \text{ cm}^{-2}$ on 40 Å strip width. If we compare this electron density to that obtained in the case of DySi₂ in Table 5.1, we can see that the two electron densities are in the same order of magnitudes.

If we turn our attention to the width of the experimental plasmons losses, one can see from Fig. 6.19 that the width decreases first with increasing momentum transfer and the losses become again broad. The fitting performed using the symmetric plasmon mode can not explain this behavior.

If we consider again the higher mode in the strip plasmon theory, the splitting between the symmetric mode S1 and the antisymmetric one AS1 could explain the broadening behavior (Fig. 6.28). The combination of S1 and AS1 could create a shoulder at energy around 300 meV to 400 meV as observed experimentally since the S1 mode was found to have a higher intensity compared to the AS1 mode in the calculations. The S2 mode, though its intensity was found to have even higher than AS1, was not detected in the experiments.

Chapter 7

Summary and outlook

The present work has been dedicated to the study of collective electronic excitations on low-dimensional Dy-silicide structures. Through confinement of electron gas systems in 2D and 1D structures, new physical, optical and magnetic properties arise. These properties are different from the bulk properties. Dy-silicide offers here a unique class of material for research due to the fact that the same material can be used to form a highly ordered monolayer flat film and perfectly aligned thin nanowires. The ELS-LEED device used in the experiments did enable to set some relationship between the different Dy-silicide phases and the resulting energy losses.

The first reported experimental results concerned the study of Dy-silicide on Si(111). The small lattice mismatch between the two lattices allowed to form flat monolayer DySi₂. The perfect ordering in the film enabled to study collective electronic excitations in that system. Accordingly a plasmon dispersion was found, with a vanishing plasmon energy in the long-wavelength limit ($q \rightarrow 0$), with q the wave number. Starting from $q=0$, the plasmon energy increased as \sqrt{q} until $q = 0.1 \text{ \AA}^{-1}$, and then begins to saturate. A 2D-plasmon fit model using equation 2.34 seems to fit well the experimental dispersion curve in the range of $q \leq 0.1 \text{ \AA}^{-1}$. A very small deviation between the two curves exists between 0.03 and 0.09 \AA^{-1} , where the experimental curve lies slightly above the fit model. We were able to extract an electron density of the order of 10^{14} cm^{-2} . In comparison, approximately 2 ML of ErSi₂ were found to have an electron density of $8.7 \times 10^{20} \text{ cm}^{-3}$ and an electron effective mass of $4.6m_0$, with m_0 the electron mass.

On the flat Si(001), Dy-silicide builds nanowires. Depending on the growth conditions, thin or thicker wires can be formed. We have focused on the thinner wires due to their close-packed structures. Surprisingly the occurrence of the 7×2 reconstruction was connected to the high intensity losses. We turned then to the vicinal Si(001) to enhance formation of symmetric structures. When the coverage is increased slowly, the Dy-silicide was first decorating the steps, but then began to induce other reconstructions. We have reported of $n \times 2$ reconstruction, with n running between 7 and 10. The experimental dispersion curve was not fitting in any 1D or 2D-plasmon model. A new theory treating the wires as strip structures of 40 \AA width succeeded to reproduce the

experimental data. Here again an electron density of $3.3 \times 10^{14} \text{cm}^{-3}$ and an effective mass of $1.4m_0$ were extracted.

The electron densities values in the DySi₂ monolayer film as well as in the nanowire structures are in the order of magnitudes that should account for by 2D electron systems. Here, more experimental and theoretical work is called out to try to tune the width of the Dy-silicide nanowires towards 1D-behavior and for model calculations.

Bibliography

- [1] M. Sundaram, S. A. Chalmers, P. F. Hopkins, and A. C. Gossard *New Quantum Structures Science* **254** 1326 (1991)
- [2] R. H. Chen, A. N. Korotov, and K. K. Likharev, *Single electron transistor logic* Appl. Phys. Lett. **68** 1954 (1996)
- [3] C. P. Collier, E. W. Wong, M. Belohradský, Raymo, J. F. Stoddart, P. J. Kuekes, R. S. Williams, J. R. Heath, *Complex dynamics of mesoscopic magnets* Science **285** 391 (1999)
- [4] W. Mönch, *Semiconductor surfaces and interfaces* Springer, Berlin (1995)
- [5] J. E. Baglin, F. M. d'Heurle, and C. S. Petersson, *The formation of silicides from thin films of some rare-earth metals* Appl. Phys. Lett. **36** 594 (1980)
- [6] J. A. Knapp and S. T. Picraux *Epitaxial growth of rare-earth silicides on (111) Si* Appl. Phys. Lett. **48** 466 (1986)
- [7] P. Paki, U. Kafader, P. Wetzel, C. Pirri, J. C. Peruchetti, D. Bolmont, and G. Gewinner *Growth of a two-dimensional Er silicide on Si(111)* Phys. Rev. B **45** 8490 (1992)
- [8] K. N. Tu, R. D. Thompson, and B. Y. Tsaur, *Low Schottky barrier of rare-earth silicide on n-Si* Appl. Phys. Lett. **38** 626 (1981)
- [9] H. Norde, J. de Sousa Pires, F. d'Heurle, F. Pesavento, S. Petersson, and P. A. Tove, *The Schottky-barrier height of the contacts between some rare-earth metals (and silicides) and p-type Si* Appl. Phys. Lett. **38** 865 (1981)
- [10] S. Vandr , T. Kalka, C. Preinesberger, and M. Dahne-Prietsch, *Flatband conditions observed for lanthanide-silicide monolayers on n-Type Si(111)* Phys. Rev. Lett. **82** 1927 (1999); **82** 4370 (1999)
- [11] S. Vandr , T. Kalka, C. Preinesberger, and M. Dahne-Prietsch, *Epitaxial growth and electronic structure of lanthanide silicides on n-type Si(111)* J. Vac. Sci. Technol. B **17** 1682 (1999)

- [12] L. Pahun, Y. Campidelli, F. Arnaud d'Avitaya, and P. A. Badoz, *Infrared response of Pt/Si/ErSi_{1.7} heterostructure: Tunable internal photoemission sensor* Appl. Phys. Lett. **60** 1166 (1992)
- [13] T. A. Nguyen Tana, J. -Y. Veullen, S. Kennou and L. Magaud, *Si/ErSi_{1.7} interfaces and Si reepitaxy on the ErSi_{1.7}/Si structure* Appl. Surf. Sci. **70/71** 520 (1993)
- [14] M. H. Unewisse and J. W. V. Storey, *Electrical and infrared investigation of erbium silicide* J. Appl. Phys. **72** 2367 (1992)
- [15] C. Deng, T. W. Sigmon, J. C. Wu, M. N. Wybourne, and J. Rack, *Formation and characterization of ultrasmall dimension GeSi wire structure by using pulsed laser-induced epitaxy* Appl. Phys. Lett. **68** 3734 (1996)
- [16] D.-X. Xu, J. P. McCaffrey, S. R. Das, G. C. Aers, and L. E. Erickson, *Electrical and structural properties of PtSi films in deep submicron lines* Appl. Phys. Lett. **68** 3588 (1996)
- [17] D. Lenssen and S. Mantl, *Observation of quantum interference effects in submicron CoSi₂ wires in Si(100)* Appl. Phys. Lett. **71** 3540 (1997)
- [18] M. M. R. Evans, J. Nogami, *Indium and gallium on Si(001): A closer look at the parallel dimer structure* Phys. Rev. B **59** 7644 (1999)
- [19] C. Preinesberger, S. Vandr , T. Kalka, and M. D hne-Prietsch, *Formation of dysprosium silicide wire on Si(001)*, Appl. Phys. D **31** L43 (1998)
- [20] J. Nogami, B. Z. Liu, M.V. Katkov, C. Ohbuchi, and N. O. Birge, *Self-assembled rare-earth silicide nanowires on Si(001)*, Phys. Rev. B **63** 23305 (2001)
- [21] D. Lee, D. K. Lim, S. S. Bae, S. Kim, R. Ragan, D. A. A. Ohlberg, Y. Chen, and R. S. Williams, *Unidirectional hexagonal rare-earth disilicide nanowires on vicinal Si(100)-2×1*, Appl. Phys. A **80** 1311 (2005)
- [22] C. Preinesberger, G. Pruskil, S. K. Becker, M. D hne, D. V. Vyalikh, S. L. Molodtsov, C. Laubschat, and F. Schiller, *Structure and electronic properties of dysprosium-silicide nanowires on vicinal Si(001)*, Appl. Phys. Lett. **87** 083107 (2005)
- [23] I. Engelhardt, C. Preinesberger, S.K. Becker, H. Eisele, and M. D hne, *Atomic structure of thin dysprosium-silicide layers on Si(111)*, Surf. Sci. **600** 755 (2006)
- [24] S. Tomonaga, *Remarks on Bloch's method of sound waves applied to many-fermion problem*, Prog. Theor. Phys. **5**, 544 (1950)

- [25] F. Stern, *Polarizability of a Two-Dimensional Electron Gas*, Phys. Rev. Lett. **18**, 546 (1967)
- [26] T. Inaoka, *Predicted energy-loss spectrum of two-dimensional plasmons in a metallic strip monolayer on a semiconductor surface*, Phys. Rev. B **71** 115305 (2005)
- [27] M. Horn-von Högen, *Growth of semiconductor layers studied by spot profile analysing low energy electron diffraction* Z. Kristallogr. **214** 1 (1991)
- [28] H. Ibach and D. L. Mills, *Energy electron loss spectroscopy and surface vibrations*, (Academic, San Francisco, 1982)
- [29] P. A. Thiry, M. Liehr, J. J. Pireaux, and R. Caudano, *Electron interaction mechanisms in high resolution electron energy loss spectroscopy*, Physica Scripta **35**, 368 (1987)
- [30] H. Froitzheim, H. Ibach, and D. L. Mills, *Surface optical constants of silicon and germanium derived from electron energy-loss spectroscopy*, Phys. Rev. B **11**, 4980 (1975)
- [31] D. Šokčević, Z. Lenac, R. Brako, and M. Šunjić, *Excitation of adsorbed molecule vibrations in low energy electron scattering.*, Z. Physik B **28**, 273 (1977)
- [32] S.Y. Tong, C. H. Li, and D. L. Mills, *Inelastic scattering of electrons from adsorbate vibrations: large-angle deflections*, Phys. Rev. Lett. **44**, 407 (1980)
- [33] S.Y. Tong, C. H. Li, and D. L. Mills, *Inelastic scattering of electrons from adsorbate vibrations in impact scattering regime*, Phys. Rev. B **24**, 806 (1981)
- [34] A. Zangwill, *Physics at surfaces*, Cambridge University Press, Cambridge (1988)
- [35] H. Ibach and H. Lüth, *Festkörperphysik*, Springer-Verlag, (1993)
- [36] G. Mie, *Beiträge zur Optik trüber Medien, speziell kolloidaler Metallösungen*, Ann. Phys. **25**, 377 (1908)
- [37] A. Liebsch, *Surface plasmon dispersion and size dependence of Mie resonance: Silver versus simple metals*, Phys. Rev. B **48**, 11317 (1993)
- [38] A. Liebsch, *Electronic excitations at metal surfaces*, Plenum Press, New York (1997)
- [39] H. Kuzmany, *Festkörperspektroskopie*, Springer Verlag (1990)
- [40] H. Ehrenreich and H. R. Philipp, *Optical properties of Ag and Cu.*, Phys. Rev. **128**, 1622 (1962)

- [41] B. N. Persson and J. E. Demuth, *Determination of the frequency-dependent resistivity of ultrathin metallic films on Si(111)*, Phys. Rev. B **31** 1856 (1985)
- [42] P. J. Feibelman, *Surface electromagnetic fields*, Prog. in Surf. Sci. **12**, 287 (1982)
- [43] P. J. Feibelman, *Interpretation of the linear coefficient of surface-plasmon dispersion*, Phys. Rev. B **40**, 2752 (1989)
- [44] A. Liebsch, *Dynamical screening at simple-metal surfaces*, Phys. Rev. B **36**, 7378 (1987)
- [45] J. E. Inglesfield, *Surface electronic structure.*, Rep. Prog. Phys. **45**, 223 (1982)
- [46] E. V. Chulkov, V. M. Silkin, E. N. Shirykalov, *Surface electronic structure of Be(0001) and Mg(0001).*, Surf. Sci. **188**, 287 (1987)
- [47] B. Diaconescu, K. Pohl, L. Vattuone, L. Savio, P. Hofmann, V. M. Silkin, J. M. Pitarke, E. V. Chulkov, P. M. Echenique, D. Farías, and M. Rocca, *Low-energy acoustic plasmons at metal surfaces*, Nature **448**, 57 (2007)
- [48] S. Das Sarma and E. H. Hwang, *Dynamical response of a one-dimensional quantum-wire electron system*, Phys. Rev. B **54**, 1936 (1996)
- [49] J. M. Elson and R. H. Ritchie, *The damping rate of plasma waves in condensed matter*, Surf. Sci. **30** 178 (1972)
- [50] H. Froitzheim and H. Ibach, *Interband transitions in ZnO observed in low energy electron spectroscopy*, Zeitschr. f. Phys. **269** 17 (1974)
- [51] U. Scheithauer, G. Meyer, and M. Henzler, *A new LEED instrument for quantitative spot profile analysis*, Surf. Sci. **178** 441 (1986)
- [52] H. Claus, *Aufbaus eines SPA-LEED mit Energieauflösung*, Ph.D. Thesis, Universität Hannover (1992)
- [53] H. Claus, A. Büssenschütt, and M. Henzler, *Low-energy electron diffraction with energy resolution*, Rev. Sci. Instrum. **63** 2195 (1992)
- [54] M. Rocca, U. Valbusa, and F. Moresco, *On Plasmon dispersion measurements by EELS*, in: A. F. Ponce, M. Cardona (Eds), Surface Science, Springer Proceedings in Physics, Vol. 62, Springer-Verlag Berlin Heidelberg (1992), p. 59
- [55] Ch. Kittel, *Einführung in die Festkörperphysik*, 10. Aufl., Oldenburg München, (1993)
- [56] J. J. Lander, G. W. Gobeli, and J. Morrison, *Structural properties of cleaved silicon and germanium surfaces*, J. Appl. Phys. **34** 2298 (1963)

- [57] N. Osakabe, K. Yagi, and G. Honjo, *Reflection electron microscope observations of dislocations and surface structure phase transition on clean (111) silicon surfaces*, Japan J. Appl. Phys. **19** L309 (1980)
- [58] K. Takayanagi, Y. Tanishiro, Sh. Takahashi, and M. Takahashi, *Structure analysis of Si(111)-7×7 reconstructed surface by transmission electron diffraction*, Surf. Sci. **164** 367 (1985)
- [59] B. N. J. Persson and J. E. Demuth, *Inelastic scattering of slow electron from Si(111) surfaces*, Phys. Rev. B **30** 5968 (1984)
- [60] U. Backes and H. Ibach, *Evidence of a 2D-metallic state of the clean 7×7 Si(111) surface*, Solid State Communication **40** 575 (1981)
- [61] H. Froitzheim, U. Köhler, and H. Lammering, *Electronic structure of the 7×7 Si(111): Differences due to preparation*, Phys. Rev. B **30** 5771 (1984)
- [62] P. N. Keating, *Effect of invariance requirements on the elastic strain energy of crystals with application to the diamond structure*, Phys. Rev. **145** 637 (1966)
- [63] C. B. Duke, *Surface structures of tetrahedrally coordinated semiconductors: principles, practice, and universality*, Appl. Surf. Sci. **66** 543 (1993)
- [64] J. Zachariae, *Untersuchung zur Bildung von epitaktischen SrO- und BaO-Schichten auf Si(001)*, Universität Hannover, Diplomarbeit, 2001
- [65] Y. Wang, M. J. Bronikowski, and R. J. Hamers, *An atomically resolved scanning tunneling microscopy study of the thermal decomposition of disilane on Si(001)*, Surf. Sci. **311** 64 (1994)
- [66] Y.-W. Mo, and M. Lagally, *Anisotropy in surface migration of Si and Ge on Si(001)*, Surf. Sci. **248** 313 (1991)
- [67] Y.-W. Mo, J. Kleiner, M. Webb, and M. Lagally, *Surface self diffusion of Si on Si(001)*, Surf. Sci. **268** 275 (1992)
- [68] F. J. Himpsel and D. E. Eastman, *Photoemission studies of intrinsic surface states on Si(001)*, J. Vac. Sci. Technol. **16** 1297 (1979)
- [69] A. Ramstad, G. Brocks, and P. J. Kelly, *Theoretical study of the Si(001) surface reconstruction*, Phys. Rev. B **51** 14504 (1995)
- [70] S. Tang, A. J. Freeman, and B. Delley, *Structure of the Si(001)2×1 surface: Total-energy and force analysis of the dimer models*, Phys. Rev. B **45** 1776 (1992)
- [71] D. J. Chadi, *Stabilities of single-layer and bilayer steps on Si(001)*, Phys. Rev. Lett. **59** 1691 (1987)

- [72] O. L. Alerhand, A. N. Becker, J. D. Joannopoulos, D. Vanderbilt, R. J. Hamers, and J. E. Demuth, *Finite-temperature phase diagram of vicinal Si(001) surfaces*, Phys. Rev. Lett. **64** 2406 (1990)
- [73] R. D. Thompson and N. K. Tu, *Comparison of the three classes (rare earth, refractory and near-noble) of silicide contacts.*, Thin Solid Films **93** 265 (1982)
- [74] G. B. Samsonov, L. A. Drovina, and B. M. Rud, , *Silicides* (Moscow: Metallurgija) (1979)
- [75] E. Houssay, A. Rouault, O. Thomas, R. Madar, and J. P. Senateur, *Metallurgical reinvestigation of rare earth silicides.*, Appl. Surf. Sci. **38** 156 (1989)
- [76] J. E. E. Baglin, F. M. d'Heurle, and C. S. Petersson, *Diffusion marker experiments with rare-earth silicides and germanides: Relative mobilities of the two atom species*, J. Appl. Phys. **52** 2841 (1980)
- [77] P. Wetzel, S. Saintenoy, C. Pirri, D. Bolmont, and G. Gewinner, *Surface states and reconstruction of epitaxial $\sqrt{3}\times\sqrt{3}$ R30° Er silicide on Si(111)*, Phys. Rev. B **50** 886 (1994)
- [78] T. P. Roge, F. Palmino, C. Savall, J. C. Labrune, P. Wetzel, C. Pirri, and G. Gewinner, *Surface reconstruction of ErSi_{1.7}(0001) investigated by scanning tunneling microscopy*, Phys. Rev. B **51** 10998 (1995)
- [79] P. Wetzel, S. Saintenoy, C. Pirri, D. Bolmont, G. Gewinner, T. P. Roge, F. Palmino, C. Savall, and J. C. Labrune, *STM investigation of a 2- and 3-dimensional Er disilicide grown epitaxially on Si(111)*, Surf. Sci. **355** 13 (1996)
- [80] B. Z. Liu and J. Nogami, *A scanning tunneling microscopy study of dysprosium silicide nanowire growth on Si(001)*, J. Appl. Phys. **93** 593 (2003)
- [81] A.M. Shikin, A. Yu. Grigor'ev, G. V. Prudnikova, D. V. Vyalykh, S. L. Molodtsov, and V. K. Adamchuk, *Interaction of thin silicon layers with the (0001) surface of rare-earth metals*, Physics of the Solid State **42** 973 (2000)
- [82] W. A. Henle, M. G. Ramsey, and F. P. Netzer, *Formation of divalent Eu silicides at the Eu-Si(111) interface*, Surf. Sci. **254** 182 (1991)
- [83] Z. He, D. J. Smith, and P. A. Bennett, *Epitaxial DySi₂ nanowires formation on stepped Si(111)*, Appl. Phys. Lett. **86** 143110 (2005)
- [84] H. R. Philipp and H. Ehrenreich, *Optical properties of semiconductors*, Phys. Rev. **129**, 1550 (1963)
- [85] T. Nagao, T. Hildebrandt, M. Henzler, and S. Hasegawa, *Dispersion and Damping of a Two-Dimensional Plasmon in a Metallic Surface-State Band*, Phys. Rev. Lett. **86** 5747 (2001)

- [86] P. Wetzel, C. Pirri, P. Paki, J. C. Peruchetti, D. Bolmont and G. Gewinner, *Experimental band structure and Fermi surface of a two-dimensional Er silicide on Si(111)*, Solid State Comm. **82** 235 (1992)
- [87] L. Stauffer, A. Mharchi, C. Pirri, P. Wetzel, D. Bolmont, and G. Gewinner, *Electronic structure and interfacial geometry of epitaxial two-dimensional Er silicide on Si(111)*, Phys. Rev. B **47** 10555 (1993)
- [88] T. Inaoka, T. Nagao, S. Hasegawa, T. Hildebrandt, and M. Henzler, *Two-dimensional plasmon in a metallic monolayer on a semiconductor surface: Exchange-correlation effects*, Phys. Rev. B **66** 245320 (2002)
- [89] H. Ibach and J. E. Rowe, *Hydrogen adsorption and surface structures of silicon*, Surf. Sci. **43** 481 (1974)
- [90] S. Maruno, H. Iwasaki, K. Horioka, S.-T. Li, and S. Nakamura, *Electronic structures of the monohydride $(2 \times 1):H$ and the dihydride $(1 \times 1)::2H$ Si(001) surfaces studied by angle-resolved electron-energy-loss spectroscopy*, Phys. Rev. B **27** 4110 (1983)
- [91] T. Kubo, T. Aruga, N. Takagi, and M. Nishijima, *Investigation of the surface electronic states of the Si(001) $c(4 \times 2)$ and $c(8 \times 8)$ surfaces: An electron energy loss spectroscopy study*, Jpn. J. Appl. Phys. **36** L975 (1997)
- [92] A. I. Shkrebtii and R. Del Sole, *Microscopic calculation of the optical properties of Si(100) 2×1 : Symmetric versus asymmetric dimers*, Phys. Rev. Lett. **70** 2645 (1993)
- [93] H. H. Farrell, F. Stucki, J. Anderson, D. J. Frankel, G. L. Lapeyre, and M. Levinson, *Electronic excitations on Si(001)(2×1)*, Phys. Rev. B **30** 721 (1984)
- [94] T. Sakamoto and G. Hashiguchi, *Si(001)- 2×1 single-domain structure obtained by high temperature annealing*, Japan J. Appl. Phys. **25** L78 (1986)
- [95] N. Frangis, J. Van Landuyt, G. Kaltsas, A. Travlos, and A. G. Nassiopoulos, *Growth of erbium-silicide on (001) silicon as characterised by electron microscopy and diffraction*, Journal of Crystal Growth **172** 175 (1997)
- [96] B. Z. Liu and J. Nogami, *An STM study of the Si(001)(2×4)-Dy surface*, Surf. Sci. **488** 399 (2001)
- [97] Y. Chen, D. A. A. Ohlberg, G. Medeiros-Ribeiro, Y. A. Chang, and R. S. Williams, *Self-assembled growth of epitaxial erbium disilicide On silicon (001)*, Appl. Phys. Lett. **76** 4004 (2000)
- [98] B. Z. Liu, and J. Nogami, *An STM study of the Si(001)(2×7)-Gd, Dy surface*, Surf. Sci. **488** 399 (2001)

- [99] C. Preinesberger, S. K. Becker, and M. Dähne, *An STM study of the 2×7 dysprosium-silicide nanowire superstructure on Si(001)*, AIP Conference Proceedings **696** 837 (2003)
- [100] Y. Chen, D. A. A. Ohlberg, G. Medeiros-Ribeiro, Y. A. Chang, and R. S. Williams, *Growth and evolution of epitaxial erbium disilicide on Si(001)*, Appl. Phys. A **75** 353 (2002)
- [101] B. Z. Liu, and J. Nogami, *Growth of parallel rare-earth silicide nanowire arrays on vicinal Si(001)*, Nanotechnology **14** 873 (2003)
- [102] R. Ragan, Y. Chen, D. A. A. Ohlberg, G. Medeiros-Ribeiro, and R. S. Williams, *Ordered arrays of rare-earth silicide nanowires on Si(001)*, Journal of Crystal Growth **251** 657 (2003)
- [103] K. S. Singwi, M. P. Tosi, R. H. Land, and A. Sjölander, *Electron Correlations at Metallic Densities*, Phys. Rev. **176** 589 (1968)

Curriculum Vitae

Personal Data:

Name: Eddy Patrick Rugeramigabo
Date of birth: 17.03.1975
Place of birth: Bujumbura (in Burundi)
Citizenship: Burundi
Family status: married
Children: one son

School:

1981-1987 Primary School in Bujumbura
1987-1994 High School in Bujumbura
November 1994 High School Diploma

Bachelor (Licence):

1994-2000 Study of Physics at the University of Burundi
30th June 2000 Degree in Physics (Licence en Sciences Physiques)
at the University of Burundi
Title of the Thesis:
'Representations du groupe de Poincare comme
limite de la serie discrete du groupe de De Sitter
a l'aide des etats coherents'

Position:

July 2000 - Jan. 2001 Teacher of Physics in High School in Bujumbura
Febr. 2001 - Oct. 2001 Assistant Lecturer at the University of Burundi

Master:

Oct. 2001 - April 2004 Master in Solid State Institut, Surface Science Department
Universität Hannover (Germany)
30 April 2004 Master of Science in Physics

PhD:

Since Mai 2004 Scientific coworker at
Solid State Institut, Surface Science Department
Universität Hannover
Appelstr. 2, 30167 Hannover
under the supervision of
Prof. Dr. H. Pfnür

Acknowledgement

I would like to thank Prof. H. Pfnür to have made the present work possible. He has entitled me an interesting and very challenging work. Only through his continuous support, patience, helpfull discussions and suggestions, this work did come to an end.

To Dr. V. Zielasek, for introducing me in the ELS-LEED-world at the beginning of my PhD, I thank him. Even after he left, he stayed available for discussion any time need from far away in Bremen.

I would like also to thank and express my gratitudes to Prof. T. Nagao for the spontaneous help about the fitting of my experimental data. His availability to discussions at the DPG Meeting in Germany and the support about the theoretical calculations were of great help. My regards also to T. Inaoka.

To all my colleagues, thank you very much for the nice time I had in the institute and the feeling of belonging to a big family. You were always very kind, especially Priv. Doz. Dr. C. Tegenkamp, was always available and trying to understand my too specific and punctual questions. Special thanks to Elke Trolp for her understanding and help in the very many administrative questions and personal discussions.

To Marcin Czubanowski, thank you for the friendship over the years, for being the right GMF, and for the great help in the finalizing this thesis.

For the measuring time on their chamber, I would like also to thank Jędrzej Schmeidel and Dirk Müller-Sajak for their collaboration. Thanks to Dirk Müller-Sajak for the fine touch on the thesis.

I would like to thank also the 'Werkstatt' for the nice collaboration.

A special thought is dedicated to my wife Dany. Her loving support and comprehension created the right atmosphere to write and finalize the thesis. She makes home the best place to be and, for our son Niklas, she has been there for two, especially when I was taken by the thesis. Thank you Niklas for giving me a strong inner peace and joy.

I thank God for all in my life.